

# Spin and Charge in Semiconductor Nanowires



# Spin and Charge in Semiconductor Nanowires

## Proefschrift

ter verkrijging van de graad van doctor  
aan de Technische Universiteit Delft,  
op gezag van de Rector Magnificus prof. dr. ir. J.T. Fokkema,  
voorzitter van het College voor Promoties,  
in het openbaar te verdedigen op dinsdag 16 september 2008 om 15:00 uur

door

**Floris Arnoud ZWANENBURG**

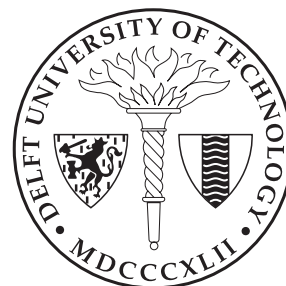
natuurkundig ingenieur  
geboren te Heerde.

Dit proefschrift is goedgekeurd door de promotor:

Prof. dr. ir. L.P. Kouwenhoven

Samenstelling van de promotiecommissie:

Rector Magnificus	voorzitter
Prof. dr. ir. L.P. Kouwenhoven	Technische Universiteit Delft, promotor
Prof. dr. ir. J.E. Mooij	Technische Universiteit Delft
Prof. dr. R.G. Clark	University of New South Wales, Sydney, Australië
Prof. dr. C.M. Lieber	Harvard University, Cambridge, Verenigde Staten
Prof. dr. J.W.M. Frenken	Universiteit Leiden
Prof. dr. ir. B.J. van Wees	Rijksuniversiteit Groningen
Dr. S. Rogge	Technische Universiteit Delft
Prof. dr. Yu.V. Nazarov	Technische Universiteit Delft, reservelid



**nano**  **ned**  **TU Delft**  
Delft University of Technology



Supported by NanoNed, a national nanotechnology program coordinated by the Dutch Ministry of Economic Affairs.

Published by: Floris Zwanenburg  
Cover design by: Marjanne Henderson  
Format: 170 x 240 mm, 128 pages  
Paper: 115 grams MultiArt Silk  
Printed by: Joh. Enschedé Amsterdam

ISBN: 978-90-8593-042-6

Casimir PhD Series, Delft-Leiden, 2008-04

Copyright © 2008 by Floris A. Zwanenburg

An electronic version of this thesis is available at [www.library.tudelft.nl/dissertations](http://www.library.tudelft.nl/dissertations)

# Preface

At the end of 2001 it was time for me to choose a group for my MSc research. The problem was that my interest in physics had never been very content-driven. I enjoyed studying for exams in the years before, but I was never passionate about any specific subject. My life was occupied with social and organizational activities, and I focused on acquiring a wide variety of skills, ready for a business career. I chose Quantum Transport because of the people and because I was hoping that their drive and working spirit would motivate me to finish fast, so I could start working for a consultancy firm or multinational. After all, their recruiters promised me I would be ‘solving complex problems in a creative environment with a steep learning curve, in a team with highly intelligent and inspiring people’.

My choice to become a PhD student thus came as a surprise, both to me and my environment. The reason was the challenge of doing a PhD in fundamental physics and more importantly, the pure joy in the work we do every day. Our job cannot be characterized any better than by the description promised by recruiting folders of the average consultancy firm or multinational, see above. On top of that, most scientists are sincerely passionate about their work. Without passion one would never be able to persist after each failed experiment. It turned out to be the best decision of my life so far: every day in the past five years I drove to the lab with pleasure and eagerness. Doing a PhD is a way of life with many opportunities and an incredible amount of freedom. However, a strong intrinsic motivation is essential to continuously work in an efficient and disciplined way towards a long-term deadline.

I have spent six years in QT, one year as a Master student and five as a PhD student. QT feels like a family: colleagues are like brothers and sisters. We do not work hard because our boss tells us to, but because we really like our job. This passion combined with the social environment and concern for another’s results is crucial for the success of the group. There will always be pushy people who mainly pursue their own goals. This may lead to good results for the individual, but in the long run it will affect the group negatively. I hope everyone continues to motivate and stimulate each other to greater heights.

Leo Kouwenhoven, thank you for giving me the opportunity to spend four months in the lab of professor Charles Marcus at Harvard University, and for trusting me to set up collaborations with two other research groups at Harvard. At crucial moments I have always had the feeling that you wanted the best for both of us. I very much appreciate the liberal in you, who avoids making decisions for another and who limits himself to strong suggestions. This way your students learn that they themselves must be the driving force behind their research, not the professor. I respect you as a scientist, as a personality, and as a football player. In the second half of last year's competition we missed your brilliant organization in the defense of Réal RKC, the QT monday night football team. I hope you will be back on the field soon and lead the team to many championships in the coming years.

Our collaborations have been of great importance to this work. Erik Bakkers and Aarnoud Roest at Philips Research have synthesized the InAs and InP nanowires, thanks for many pleasant and informative meetings. The scanning gate measurements were performed in the group of professor Robert Westervelt at Harvard University. Ania Bleszynski, I enjoyed our (non-)scientific encounters in Delft, Vienna, Cambridge, Los Angeles and Santa Barbara. The Si nanowires were grown in the group of professor Charles Lieber at Harvard University. Thank you for your hospitality and your enthusiasm about our collaboration. I felt welcome in your lab, everyone was open and willing to help me and to discuss anything about nanowires. Ying Fang, it was a pleasure to work with you. Your professionalism, eye for detail and fast answers to our questions were essential for our success. Discussions with Daniel Loss, Yuli Nazarov, Sven Rogge and Bart van Wees have contributed significantly to a better understanding of our results.

I wish to thank the scientific staff for making QT a special place by stimulating all social interactions. You give the good example with small things as joining the coffee breaks, but you also show the importance of social events by making them possible. Please keep in mind, that fitting socially into the group is a very important criterion for accepting PhD students and post-docs in QT. The most intelligent and skilful people may get the job done, but they will not get far without being able to interact with the rest of the group.

Hans Mooij, it is a great pleasure to be part of the group you built and especially of the Hans Pension Party Committee, the cream of the crops within QT. I found it impressive to see and hear the people who came over for your pension party. Lieven Vandersijpen, I enjoyed our squash games, het is eenvoudiger om je te verslaan dan je te verstaan (sorry, this only works in Dutch). Val Zwiller, your group has brought many new impulses to QT, I appreciate how you bring people from everywhere into the lab.

---

It has been a delight to supervise three fantastic MSc students. One after the other worked intensively with me for twelve months and organized the annual QT Trip. Without you I would have worked less hard and had less fun! In almost three years we have fabricated 285 samples with the electron-beam pattern generator, of which about 220 nanowire chips. This means that we have contacted roughly 2640 individual nanowires, quite a production. Dirk van der Mast, a small guy with a big mouth, and a magician on the football field. Thanks for the good conversations and our trips to Poland and Arosa, where we explored sausages, skiing and spin rausch. Anne van Loon, you are a wonderful person in all respects. Besides that, you are a gifted hockey and football player, and the Ultimate Multitasker. Too bad we lost you to the business world, see you in NYC or down under! Cathalijn van Rijmenam, we made it to the national media twice in 2007, both on television and in a renowned newspaper. We shared the most exciting part of my PhD, when the long-awaited results came in the nick of time. Thanks for fabricating the winning devices!

Raymond, the man who lives on sandwich spread, mueslibollen, tea, cake and tin-lead solder. Thank you very much for your didactic talents, all electronic support, your synthesized compositions and the friday-afternoon projects. Remember: *A banana a day keeps the noise away*. Bram, thanks for your directness, your open communication, your sense of humor and all technical support. Remco and Peter, welcome to the club, it is good to see two naughty boys sneaking through the corridor. Please do not stop making practical jokes! Yuki and Angèle, I am glad we can rely on your administrative support. Wim and Willem, thanks for supplying helium, especially in times of shortage.

Ronald Hanson, Ronny, S-prof, the new Herre, Roddelkoning, even during your two years in Santa Barbara you managed to stay better informed than most of us. I am glad you missed Stromboli, football and exchanging spicy stories so badly that you limited your post-doc to two years. Thanks for your advice, your help, the rickrolls and our many '1-2tjes' on and off the football field. Ivo Vink, thanks for your legendary impersonations and the deadline-borrel. You have the most seductive Wink ever, and as the Chinese say: '*St'ong wink is powful tool against itching Nose*'. I still wonder when our first manuscript titled 'Leading through technology by understanding people' will appear in Harvard Business Review. Pieter de Groot, Two-face, we still have to find out how Thorgal ends! It is good to have someone in the group who is always smiling. I have never met someone who can show such sincere happiness over breakfast, eleventies, computer programs, lunch, microwave generators, second lunch, Sinterklaas (does not exist), first dinners, second dinners, drinking, a midnight snack and a glass of water next to our bed.

After years of sharing the same space, your office mates know almost everything about you. Frank Koppens, Floor Paauw, I am glad I could share it with you. Frank, thanks for the strange sounds you produce and for all the fun, especially while mingling in Bostonian bachelorettes. Floor, glad you were in the office to tame Frank and me. Remember to practice controlling the ball, improve your shot and increase your running speed. Reinier Heeres, Reindeer, I am glad to leave QT in the capable hands of my follow-up hockeying corpslid a.k.a. the toptalent. Maarten van Kouwen, please make a joke. Juriaan van Tilburg and Gary Steele, we have had some unforgettable breakfast sessions after steamy nights in a non-airconditioned hotel room in sizzling Vienna. What ever happened to ‘ze fallen madonna’? Thanks to the four PhDs in the QT-house for defying their background one way or the other: Pol Forn-Diaz, a Catalan playing in royal white. Xinglan Liu, Lan, the only individualistic and direct Chinese. Umberto Perinetti, an Italian who likes Dutch diepvriespizza and dislikes football (on the train during a Euro 2008 match of the Squadra Azzurra). Katja Nowack, ze German who wants to be Dutch but mistakes Belgians for zem. I would also like to thank all other PhDs and Post-docs not mentioned here. I wish all current PhD students good luck, make sure to enjoy the ride!

Many former QT members must not be left unmentioned: Jorden van Dam & Hubert ‘Vroegslaper’ Heersche a.k.a. Jut & Jul, thanks to your diamond program I ended up using Matlab instead of Excel for data processing. Herbert, I enjoyed our discussions, trips and especially beating you by three seconds in the ski race in Arosa. Jeroen Elzerman, left-wing intellectual and always optimistic about the Dutch national football team. Laurens Willems van Beveren, thanks for the brilliant idea to go to Sydney, see you at the barbie. Silvano De Franceschi, madonna! Sami Sapmaz, the football miracle, you were personally responsible for quite a few victories of Réal RKC. Jelle Plantenberg, proost! Alberto Morpurgo, I hope Stromboli will not go bankrupt after your leave, good luck in Geneva. Herre ‘Trouwe Hond’ van der Zant, thanks for keeping us up-to-date with the most recent NanoScience gossip and for your football lessons (in de voet!). Thomas Balder, thanks for the capacitance calculations. Mauro Porcu of the HREM group, thanks making the TEM images, for the caffès and the dinners.

Experiments in the lab do not work out without fun outside the lab. I found plenty distraction, especially in sports: Playing in the Monday night football team has been pure fun. Thanks to all players from past and present. Robert Bartelds, thanks for many endless games of squash and for a great visit to Berlin, also topsport. I have spent a significant part of the past five years on my hockey club Groen Geel. Many thanks to my hockey team for your interest in my stories and for all nano-nicknames.

---

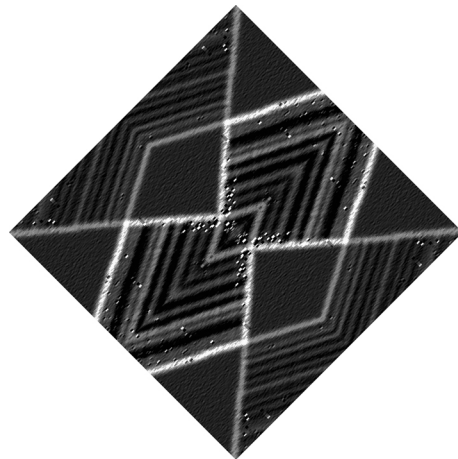
Furthermore, I am very grateful to many other friends who are important to me: my former housemates of Koornmarkt 81E, my VvTP-board, my Almanak committee and my 'clubgenoten'. Marjanne Henderson, Nico, thanks for designing the cover of my thesis – the result is beautiful! Without my car I would not have been able to spend so many hours in the lab, thank you for five years of unconditional logistic, audiovisual and mental support. Arthur and Bernard, I am looking forward to having you in front of me during my defence.

Seeing my friends from grammar school in Zwolloywood regularly is very valuable to me. Astarte, Bernard, Bettie, Dolf, Roland and your better halves, thanks for the many dinners that got out of hand (e.g. due to the Sandorf's drankenkabinet). Sorry for my late arrivals straight from the lab, even if the dinner was at my own place... Our friendship has remained strong despite all of us moving to different parts of the world one after the other. I have fantastic memories with you in South Africa, Curaçao, Diemen-Zuid, Rome, Boston, Glimmen, Hurghada, Alanya, Sharm El-Sheikh and several obscure villages in France. I hope we can add Shanghai and Sydney to the list in the years to come!

I thank my brothers, their partners, my parents and grandparents for their continuous love and support. Finally, I thank Marjolein for signing up her team for the Haagse Hockey Open 2007, and Pauline for showing up. After thirteen years at university in Delft, it is time for a change. Sydney, here I come!

Floris Zwanenburg  
August 2008





# Contents

<b>Preface</b>	<b>5</b>
<b>1 Introduction</b>	<b>13</b>
1.1 Quantum physics . . . . .	13
1.2 Spin and charge . . . . .	14
1.3 Semiconductor nanowires . . . . .	15
1.4 Outline of this thesis . . . . .	15
<b>2 Theoretical concepts and device fabrication</b>	<b>17</b>
2.1 Quantum dots . . . . .	17
2.2 Semiconductor nanowire growth . . . . .	22
2.3 Device fabrication and measurement techniques . . . . .	24
<b>3 Silicon and silicon nanowires</b>	<b>27</b>
3.1 Crystal structure and energy bands . . . . .	27
3.2 Transport properties . . . . .	32
3.3 Silicon nanowires . . . . .	34
<b>4 Silicon nanowire quantum dots</b>	<b>39</b>
4.1 Two types of Si nanowire quantum dots . . . . .	40
4.2 Single quantum dots of varying lengths . . . . .	42
4.3 Capacitances and dot lengths . . . . .	44
4.4 Towards the few-hole regime . . . . .	47
<b>5 Few-hole spin states in a silicon nanowire quantum dot</b>	<b>49</b>
5.1 Introduction . . . . .	50
5.2 Small silicon quantum dots . . . . .	51
5.3 Observation of the last hole . . . . .	55
5.4 Zeeman energy of the first four holes . . . . .	57
5.5 Magnetospectroscopy of the first four holes . . . . .	59
5.6 Additional material . . . . .	62

<b>6</b>	<b>Quantized energy emission in a few-hole Si nanowire quantum dot</b>	<b>65</b>
6.1	Introduction . . . . .	66
6.2	Discrete energy spectrum due to environment . . . . .	66
6.3	Quantized energy spectrum for different bias directions . . . . .	69
6.4	Quantization independent of magnetic field . . . . .	69
6.5	Quantized energy emission to the environment . . . . .	72
6.6	Discussion . . . . .	75
<b>7</b>	<b>Scanned probe imaging of quantum dots inside InAs nanowires</b>	<b>77</b>
7.1	Introduction . . . . .	78
7.2	Scanned probe microscopy of InAs nanowires . . . . .	78
7.3	Spatially mapping quantum dots . . . . .	80
7.4	Quantum dot size . . . . .	82
7.5	Evolution of SPM images with tip voltage . . . . .	83
7.6	Additional material . . . . .	85
<b>8</b>	<b>Electric field control of magnetoresistance in InP nanowires</b>	<b>87</b>
8.1	Introduction . . . . .	88
8.2	Electric field control of magnetoresistance . . . . .	90
8.3	Relation between transconductance and magnetoresistance . . . . .	91
8.4	Magneto-Coulomb effect and spin transport . . . . .	93
8.5	Magnetoresistance with one ferromagnet . . . . .	94
8.6	Magnetoresistance at high bias . . . . .	95
8.7	Discussion . . . . .	97
	<b>Bibliography</b>	<b>103</b>
	<b>Summary</b>	<b>115</b>
	<b>Samenvatting</b>	<b>119</b>
	<b>Curriculum Vitae</b>	<b>123</b>
	<b>Publications</b>	<b>125</b>

# Chapter 1

## Introduction

### 1.1 Quantum physics

Quantum physics generalizes classical physics, which is only a special case. It provides accurate descriptions for many phenomena that cannot be explained classically, such as the photo-electric effect and stable electron orbits. In the early 20<sup>th</sup> century, Albert Einstein showed that an electromagnetic wave such as light is composed of discrete quanta rather than continuous waves [1], earning him the Nobel Prize in 1921. Ironically, he had serious theoretical issues with quantum mechanics and tried for many years to disprove or modify it. In quantum mechanics we discover that the entire universe is actually a series of probabilities. Many quantum phenomena, such as the particle-wave duality and tunneling through classically impenetrable barriers, are counterintuitive for humans used to a world of classical objects. This led the physicist Richard Feynman to say: *‘I think it is safe to say that no one understands Quantum Mechanics.’*

While the interpretation of quantum physics remains under debate, the theory is generally accepted to give an adequate description of our physical reality within present-day experimental limits. So, rather than trying to comprehend it we want to use quantum physics in applications. The experiments described in this thesis have been carried out in the Quantum Transport Group, part of the Kavli Institute of NanoScience at Delft University of Technology. The research in our group focuses on understanding and controlling the quantum properties of structures with typical sizes of 10 to 100 nanometer. We use nanotechnology to design the small structures used in our experiments. Possible long-term applications of this fundamental research are novel electronics devices and the realization of a new type of computer, the quantum computer. Here we study two properties of electrons and holes in semiconductor nanowires: their electrostatic charge and magnetic moment, called spin.

## 1.2 Spin and charge

In our daily lives we use the spin and charge of electrons practically every day. The operation of the transistor is based on the *charge* of electrons in a semiconductor. At the time of the invention in 1947 the researchers at Bell Labs could not have guessed it would lead to the rapid development of the computer industry. Analogously, the mechanism responsible for the giant magnetoresistance in magnetic multi-layers is founded on the *spin* of electrons. After the discovery in 1988 it resulted in the realization of hard-disk drives, nowadays a billion-dollar industry. Both breakthroughs were then a part of fundamental research, and have later had an enormous impact on human society.

A long-term application of nanotechnology is the development of novel electronic devices that outclass modern-day silicon integrated-circuit technology. Computer processing power has doubled roughly every 18 months in the past decades, mainly by making the charge-based transistors smaller and smaller [2]. Nanotechnology offers the promise of continuing the miniaturization, but this will no longer hold when the active components reach the size of individual atoms and stop obeying the classical laws of physics. One solution is presented by the field of ‘spintronics’, where the spin degree of freedom is used in addition to, or instead of the charge degree of freedom. Without having to proceed the miniaturization, spintronics has the potential advantage of increased data processing speed, decreased electric power consumption, non-volatility, and increased integration densities [3, 4, 5].

Instead of avoiding the quantum mechanical nature of electrons, we may exploit it for computations that are classically impossible. A classical computer has a memory made up of bits, where each bit represents either 1 or 0. A so-called quantum computer maintains a sequence of quantum bits, or qubits, which can be in a quantum superposition of both 0 and 1; moreover, a quantum computer with  $n$  qubits can be in up to  $2^n$  different states simultaneously. The qubits are then manipulated by means of a quantum algorithm to perform quantum logic. A quantum computer would be able to carry out specific tasks that a classical computer will not be able to solve within the lifetime of the universe, e.g. the factorization of large numbers with Shor’s algorithm [6].

There are several proposals for quantum mechanical two-level systems that can comprise the states of a qubit, e.g. atoms in an optical lattice [7], ions in electrostatic traps [8], flux qubits in superconducting circuits [9] and solid state spin qubits [10, 11]. In case of the latter, confined electron spins form the basis of a quantum bit, where spin-up and spin-down represent the qubit states. The potential of the spin qubit is underlined by the recent demonstration of

coherent control of one and two spin states in quantum dots in GaAs/AlGaAs heterostructures [12, 13]. A drawback of these materials is the limited electron spin coherence time, caused by interactions with the nuclear environment. The motivation to use silicon arises from the fact that those interactions are much weaker in Si. Indeed, spin lifetimes longer than 500 ns have been measured on a macroscopic number of spins [14, 15]. In this thesis we show the first report of the identification of spin states of the first four holes in a silicon quantum dot. These results are an important step towards the realization of spin qubits in a material with a long spin coherence time, crucial for quantum computation with single spins.

### 1.3 Semiconductor nanowires

In the past years, science has shown great interest in semiconducting crystalline nanowires, cylinder-shaped wires with aspect ratios of 1000 or more. Nanowires have diameters up to tens of nanometers and can be tens of microns long. Their strength lies in the precisely controlled and tunable chemical composition, structure, size, and morphology, since these characteristics determine their corresponding physical properties. The versatility of chemically grown semiconductor nanowires promises a wide range of potential applications, such as nanoelectronics, nanophotonics, quantum information processing and biochemical sensors [16, 17, 18]. The high degree of freedom in nanowire synthesis additionally allows epitaxial growth of heterostructures in both the radial and longitudinal direction. The doping can be varied during growth, to make for example *pn*-junctions within a single nanowire to create LEDs. It is essential for this work that a nanowire provides natural confinement for electrons and holes due to its small size, making it ideal to observe quantum effects.

### 1.4 Outline of this thesis

This thesis describes a series of electronic transport experiments aimed at a better understanding of spin and charge effects in semiconductor nanowires. *Chapter 2* starts with a general introduction to the theory of quantum dots. Next, we describe the growth of semiconductor nanowires, the fabrication of nanowire devices and the measurement techniques.

*Chapters 3 to 6* focus on silicon nanowires. In *Chapter 3* we describe the crystal structure and the energy bands of bulk silicon. Next, we address properties such as the mobility, doping and the metal-silicon interface. We end by discussing

to what extent these properties apply to silicon nanowires.

In *Chapter 4* we demonstrate the experimental realization of single quantum dots in *p*-type silicon nanowires. We observe pronounced excited states in many devices with short channel lengths, i.e. shorter than 50 nm. Most devices split up into two dots before we reach the few-hole regime due to local potential perturbations in the environment of the dot.

We demonstrate control of the hole number down to one in *Chapter 5*. Detailed measurements at perpendicular magnetic fields reveal the Zeeman splitting of a single hole in silicon. We are able to determine the ground-state spin configuration for one to four holes occupying the dot and find a spin filling with alternating spin-down and spin-up holes, which is confirmed by additional magnetospectroscopy up to 9 T.

An unusual feature in single-hole silicon nanowire quantum dots is analyzed in *Chapter 6*. We observe transitions corresponding to additional energy levels below the  $N = 0$  ground-state energy of the dot, which cannot correspond to electronic or Zeeman states. The levels are quantized in multiples of 100–180  $\mu\text{eV}$  and independent of magnetic field. We explain the discrete energy spectrum as inelastic tunneling processes, where the excess energy is emitted to quantized states in the environment of the quantum dot. The most likely explanation for the excitations is acoustic phonon emission to a cavity between the two contacts to the nanowire.

In *Chapter 7* we show how a scanning probe microscope can be used to find individual quantum dots inside InAs nanowires. Complex patterns of concentric rings in conductance plots mapped across the length of the nanowires reveal the presence of multiple quantum dots, formed by disorder. Rings of high conductance are centered on each quantum dot, corresponding to the addition or removal of electrons by the scanning probe.

*Chapter 8* presents electric field control of the magnetoresistance in InP nanowires with ferromagnetic contacts. The magnetoresistance is induced by a single ferromagnetic contact and persists at high bias. The origin is found in a magnetically induced change in the ferromagnetic work function, which alters the electric field experienced by the InP nanowire and hence the total device resistance. These results show our ability to combine the functionalities of semiconductors and magnetic materials.

# Chapter 2

## Theoretical concepts and device fabrication

### 2.1 Quantum dots

A quantum dot is a small box that can be filled with electrons. The box is coupled via tunnel barriers to a source and drain reservoir, with which particles can be exchanged (see Figure 2.1). By attaching current and voltage probes to these reservoirs, we can measure the electronic properties of the dot. The dot is also coupled capacitively to one or more ‘gate’ electrodes, which can be used to tune the electrostatic potential of the dot with respect to the reservoirs. When the size of the dot is comparable to the wavelength of the electrons that occupy it, the system exhibits a discrete energy spectrum, resembling that of an atom. As a result, quantum dots behave in many ways as artificial atoms [19]. In experiments described in this thesis we have used the latter to study quantum dots defined in segments of semiconductor nanowires. Here we present a general introduction to electronic transport through quantum dots based on ref. [20].

Because a quantum dot is such a general kind of system, there exist quantum dots of many different sizes and materials: for instance single molecules trapped between electrodes, metallic or superconducting nanoparticles, self-assembled quantum dots, semiconductor lateral or vertical dots, and also semiconducting nanowires or carbon nanotubes between closely spaced electrodes. In this thesis, we focus on semiconductor nanowire quantum dots.

#### **Constant Interaction model**

A simple, yet very useful model to understand electronic transport through QDs is the constant interaction (CI) model [21]. The CI model makes two important assumptions. First, the Coulomb interactions among electrons in the dot, and

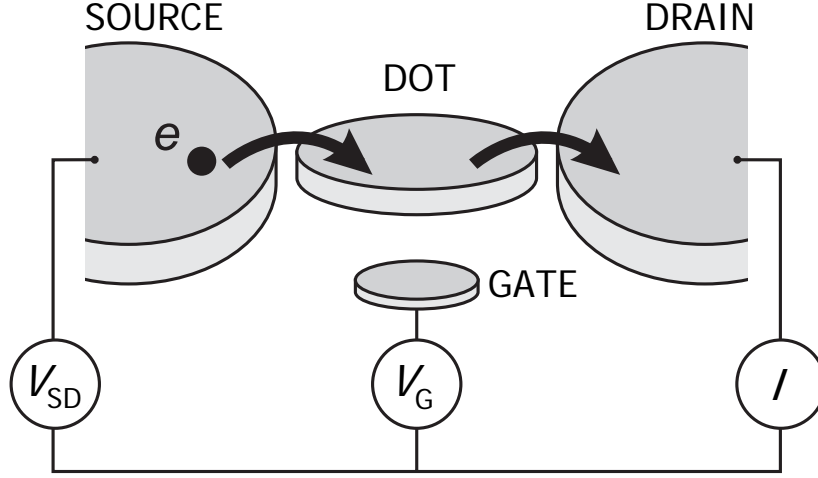


**Figure 2.1: Schematic picture of a quantum dot.** The quantum dot (represented by a disk) is connected to source and drain contacts via tunnel barriers, allowing the current through the device,  $I$ , to be measured in response to a bias voltage,  $V_{SD}$  and a gate voltage,  $V_G$ .

between electrons in the dot and those in the environment, are parameterized by a single, constant capacitance,  $C$ . This capacitance can be thought of as the sum of the capacitances between the dot and the source,  $C_S$ , the drain,  $C_D$ , and the gate,  $C_G$ :  $C = C_S + C_D + C_G$ . Second, the discrete energy spectrum can be described independently of the number of electrons on the dot. Under these assumptions the total energy of a  $N$ -electron dot in the ground state with the source-drain voltage,  $V_{SD}$ , applied to the source (and the drain grounded), is given by

$$U(N) = \frac{[-|e|(N - N_0) + C_S V_{SD} + C_G V_G]^2}{2C} + \sum_{n=1}^N E_n(B) \quad (2.1)$$

where  $-|e|$  is the electron charge and  $N_0$  the number of electrons in the dot at zero gate voltage, which compensates the positive background charge originating from the donors in the heterostructure. The terms  $C_S V_{SD}$  and  $C_G V_G$  can change continuously and represent the charge on the dot that is induced by the bias voltage (through the capacitance  $C_S$ ) and by the gate voltage  $V_G$  (through the capacitance  $C_G$ ), respectively. The last term of equation (2.1) is a sum over the occupied single-particle energy levels  $E_n(B)$ , which are separated by an energy  $\Delta E_n = E_n - E_{n-1}$ . These energy levels depend on the characteristics of the confinement potential. Note that, within the CI model, only these single-particle states depend on magnetic field,  $B$ .

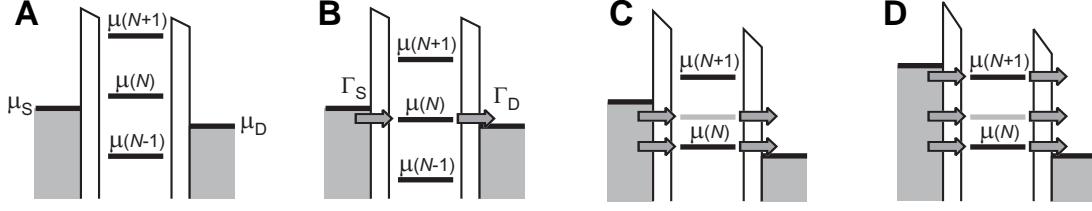


**Figure 2.2: Schematic diagrams of the electrochemical potential of the quantum dot for different electron numbers.** (A) No level falls within the bias window between  $\mu_S$  and  $\mu_D$ , so the electron number is fixed at  $N - 1$  due to Coulomb blockade. (B) The  $\mu(N)$  level is aligned, so the number of electrons can alternate between  $N$  and  $N - 1$ , resulting in a single-electron tunneling current. The magnitude of the current depends on the tunnel rate between the dot and the reservoir on the left,  $\Gamma_L$ , and on the right,  $\Gamma_R$ . (C) Both the ground-state transition between  $N - 1$  and  $N$  electrons (black line), as well as the transition to an  $N$ -electron excited state (gray line) fall within the bias window and can thus be used for transport (though not at the same time, due to Coulomb blockade). This results in a current that is different from the situation in (B). (D) The bias window is so large that the number of electrons can alternate between  $N - 1$ ,  $N$  and  $N + 1$ , i.e. two electrons can tunnel onto the dot at the same time.

To describe transport experiments, it is often more convenient to use the electrochemical potential. The electrochemical potential of the dot is by definition the energy required for adding the  $N$ th electron to the dot:

$$\begin{aligned} \mu(N) &\equiv U(N) - U(N - 1) = \\ &= (N - N_0 - \frac{1}{2})E_C - \frac{E_C}{|e|}(C_S V_{SD} + C_G V_G) + E_N \end{aligned} \quad (2.2)$$

where  $E_C = e^2/C$  is the charging energy. This expression denotes the transition between the  $N$ -electron ground state and  $N - 1$ -electron ground state. To avoid confusion when also excited states play a role, we will sometimes use a more explicit notation: the electrochemical potential for the transition between the  $N - 1$ -electron state  $|a\rangle$  and the  $N$ -electron state  $|b\rangle$  is then denoted as  $\mu_{a \leftrightarrow b}$ , and is defined as  $U_b - U_a$ .

The electrochemical potential for the transitions between ground states with a different electron number  $N$  is shown in Figure 2.2A. The discrete levels are spaced by the so-called addition energy:

$$E_{add}(N) = \mu(N + 1) - \mu(N) = E_C + \Delta E. \quad (2.3)$$

The addition energy consists of a purely electrostatic part, the charging energy  $E_C$ , plus the energy spacing between two discrete quantum levels,  $\Delta E$ . Note that  $\Delta E$  can be zero, when two consecutive electrons are added to the same spin-degenerate level.

Of course, for transport to occur, energy conservation needs to be satisfied. This is the case when an electrochemical potential level falls within the ‘bias window’ between the electrochemical potential (Fermi energy) of the source ( $\mu_S$ ) and the drain ( $\mu_D$ ), i.e.  $\mu_S \geq \mu \geq \mu_D$  with  $-|e|V_{SD} = \mu_S - \mu_D$ . Only then can an electron tunnel from the source onto the dot, and then tunnel off to the drain without losing or gaining energy. The important point to realize is that since the dot is very small, it has a very small capacitance and therefore a large charging energy – for typical dots  $E_C \approx$  a few meV. If the electrochemical potential levels are as shown in Figure 2.2A, this energy is not available (at low temperatures and small bias voltage). So, the number of electrons on the dot remains fixed and no current flows through the dot. This is known as Coulomb blockade.

The Coulomb blockade can be lifted by changing the voltage applied to the gate electrode. This changes the electrostatic potential of the dot with respect to that of the reservoirs, shifting the whole ‘ladder’ of electrochemical potential levels up or down. When a level falls within the bias window, the current through the device is switched on. In Figure 2.2B  $\mu(N)$  is aligned, so the electron number alternates between  $N - 1$  and  $N$ . This means that the  $N$ th electron can tunnel onto the dot from the source, but only after it tunnels off to the drain can another electron come onto the dot again from the source. This cycle is known as single-electron tunneling.

By sweeping the gate voltage and measuring the current, we obtain a trace as shown in Figure 2.3B. At the positions of the peaks, an electrochemical potential level is aligned with the source and drain and a single-electron tunneling current flows. In the valleys between the peaks, the number of electrons on the dot is fixed due to Coulomb blockade. By tuning the gate voltage from one valley to the next one, the number of electrons on the dot can be precisely controlled. The distance between the peaks corresponds to  $E_C + \Delta E$ , and can therefore give information about the energy spectrum of the dot.

A second way to lift Coulomb blockade is by changing the source-drain voltage,  $V_{SD}$  (see Figure 2.2C). (In general, we change the electrochemical potential of only one of the reservoirs, and keeping the other one fixed.) This increases the bias window and also ‘drags’ the electrochemical potential of the dot along, due to the capacitive coupling to the source. Again, a current can flow only when an electrochemical potential level falls within the bias window. When  $V_{SD}$  is increased so much that both the ground state as well as an excited state transition

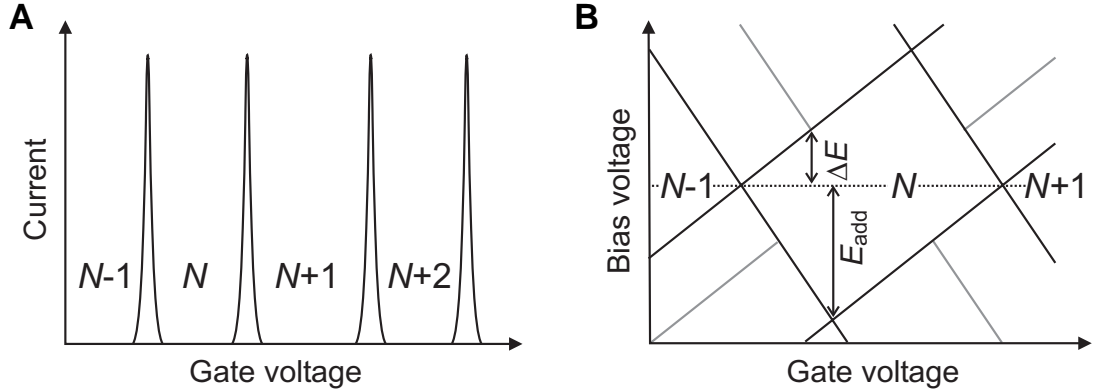


**Figure 2.3:** Transport through a quantum dot. **(A)** Coulomb peaks in current versus gate voltage in the linear-response regime. **(B)** Coulomb diamonds in differential conductance,  $dI/dV_{SD}$ , versus  $V_{SD}$  and  $V_G$ , up to large bias. The edges of the diamond-shaped regions (black) correspond to the onset of current. Diagonal lines emanating from the diamonds (gray) indicate the onset of transport through excited states.

fall within the bias window, there are two paths available for electrons tunneling through the dot. In general, this will lead to a change in the current, enabling us to perform energy spectroscopy of the excited states.

Usually, we measure the current or differential conductance (the derivative of the current with respect to the source-drain bias) while sweeping the bias voltage, for a series of different values of the gate voltage. Such a measurement is shown schematically in Figure 2.3B. Inside the diamond-shaped region, the number of electrons is fixed due to Coulomb blockade, and no current flows. Outside the diamonds, Coulomb blockade is lifted and single-electron tunneling can take place (or for larger bias voltages even double-electron tunneling is possible, see Figure 2.2D). Excited states are revealed as changes in the current, i.e. as peaks or dips in the differential conductance. From such a ‘Coulomb diamond’ the energy of excited states as well as the charging energy can be read off directly.

The simple model described above explains successfully how quantization of charge and energy leads to effects like Coulomb blockade and Coulomb oscillations. Nevertheless, it is too simplified in many respects. For instance, the model considers only first-order tunneling processes, in which an electron tunnels first from one reservoir onto the dot, and then from the dot to the other reservoir. But when the tunnel rate between the dot and the leads,  $\Gamma$ , is increased, higher-order tunneling via virtual intermediate states becomes important. Such processes are known as ‘cotunneling’. Furthermore, the simple model does not take into account the spin of the electrons, thereby excluding for instance exchange effects.

## 2.2 Semiconductor nanowire growth

In this section we describe in detail the growth of semiconductor nanowires, based on ref. [22]. The nanowire growth was performed in the group of prof. C.M. Lieber at Harvard University, and at Philips Research in Eindhoven, The Netherlands. After growth, further device processing was carried out at the Delft Institute of Microelectronics and Submicron-technology (DIMES).

Several fabrication methods are available to grow semiconductor nanowires. They can be divided into two classes: top-down and bottom-up methods. In top-down methods the strategy is to start with a large piece of semiconductor material and use techniques to obtain nanoscale wires, like nanolithography and etching. In bottom-up methods the starting point is a nano-scale object and a chemical process is used to obtain semiconductor nanowires. The nanowires studied in this thesis were grown using a bottom-up process based on the vapor-liquid-solid (VLS) growth method [23]. We have studied Si, InP and InAs nanowires grown by two different types of VLS growth methods. The most important difference between the methods is the way semiconductor vapor is supplied. In the laser-ablation method, semiconductor vapor is supplied by focusing a high-intensity laser on a semiconductor material [24]. In case of Metal-Organic Vapor-Phase Epitaxy [25] (MOVPE) or Metal-Organic Chemical Vapor Deposition (MOCVD) the semiconductor material is supplied through organic molecules like trimethylindium (TMI) and phosphine ( $\text{PH}_3$ ). Despite the fact that we use two different growth methods and various semiconductor materials, all wires are grown by the VLS growth mode. We will now discuss the growth of Si nanowires by MOCVD method (see Figure 2.4A).

A substrate with gold nanoclusters is heated under  $\text{H}_2$  gas to  $430 - 440^\circ\text{C}$  [26]. The silicon nanowires grow under a silane ( $\text{SiH}_4$ ) gas flow. The silane decomposes and Si atoms rapidly condense into Si-rich liquid nanoclusters (see Figure 2.4A). When the clusters become supersaturated, silicon will start to crystallize below the gold particle and a solid silicon nanowire grows from the substrate. The length of the nanowires is controlled by the growth time. Typically nanowires with a length of several microns are grown.

Figure 2.4C shows a typical Scanning Electron Microscopy (SEM) image of the as-grown nanowires. Over 95% of the deposited material consists of one-dimensional structures. High-resolution Transmission Electron Microscopy (HR-TEM) images are used to determine the growth direction and the crystal structure (Figure 2.4C). The long axis of most of the wires is perpendicular to the (111) lattice plane as has been reported [27], but also growth along the [211] direction is observed occasionally. Each wire is terminated by a particle containing Au and

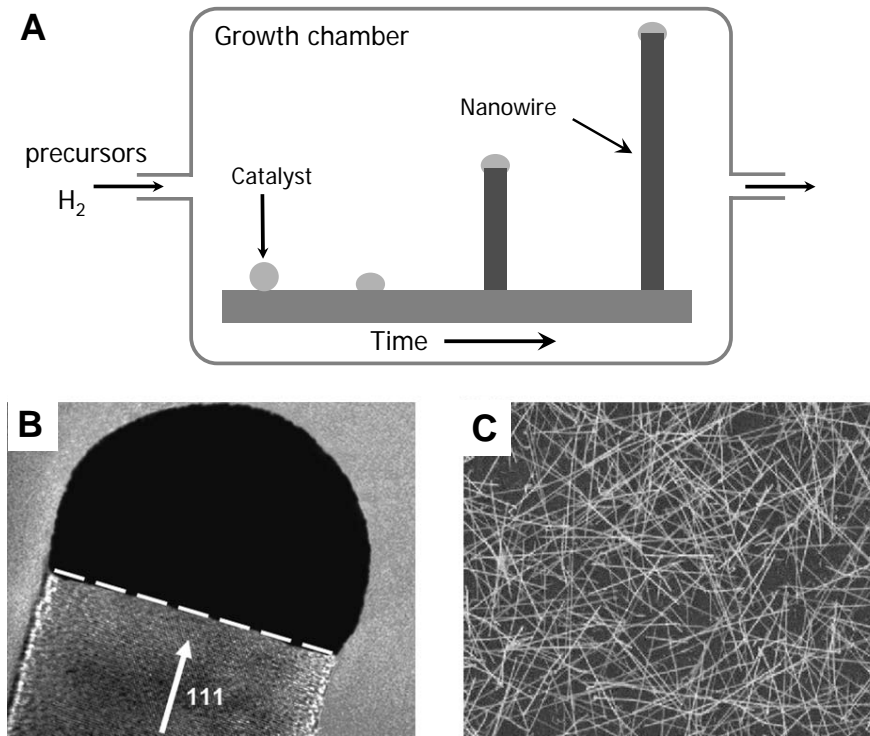


**Figure 2.4:** (A), Schematic of the VLS growth of semiconductor nanowires. The upper part of the panel shows the different stages of nanowire growth. Starting from a gold particle on the left, the second stage is a Au-Si eutect when semiconductor vapor is dissolved in the particle. When the particle is saturated with semiconductor material the single-crystal nanowire starts to grow. (B) HR-TEM image of a 30 nm diameter silicon nanowire, grown from a gold particle in the  $\langle 111 \rangle$  direction (from [26]). (C) SEM image of a substrate after growth showing the nanowires standing on the substrate.

an amount of semiconductor. The diameter of the nanowires is largely dictated by the size of the gold nanoclusters. However, the substrate temperature during growth affects the resulting diameter as well. Growth takes place via two processes, namely the liquid/solid interface between the eutectic and the nanowire (VLS growth) and the gas/solid interface between reactants and the exposed surface of the growing nanowire. Precipitation through the first interface results in axial elongation of the nanowire, while adsorption via the nanowire sidewalls results in vapor-solid growth and thickening of the radial direction. The latter is mostly unwanted because it disrupts the longitudinal uniformity of the nanowires.

As mentioned at the beginning of this section, the growth of Si by MOCVD is only one of several growth processes used throughout this thesis. Other semiconductor materials have been grown, like InAs nanowires via an MOVPE-method in chapter 7 and InP nanowires via a laser ablation method in chapter 8.

## 2.3 Device fabrication and measurement techniques

In this section we discuss the techniques for device fabrication. After describing the nanowire deposition on suitable substrates we present the principle of electron-beam lithography, which is used for defining the electrodes. Finally, we discuss the deposition of metallic contacts.

### Nanowire deposition

After growth the nanowires are transported to Delft and subsequent processing takes place at the DIMES nanofacility. The first step is the deposition of nanowires on suitable substrates for further device fabrication. We use degenerately doped  $p^{++}$  silicon wafers covered by a 50 or 285 nm thick dry thermal oxide. This allows us to use the substrates as a global gate for field-effect devices where the thermal oxide acts as the gate dielectric.

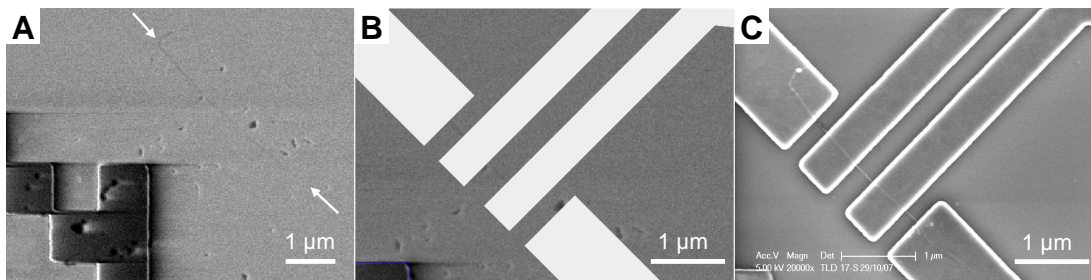


**Figure 2.5:** (A) SEM image of a silicon nanowire (indicated by white arrows) on the marker field, used to determine the position of nanowires with respect to alignment markers. (B) Computer design of the metallic contacts with distances of 300, 400, and 300 nm respectively. (C) Scanning electron microscope image of the device after contact fabrication.

Several different methods are available for the transfer of nanowires from the growth chip to the doped silicon substrates. Here we describe two processes, namely: (i) deposition from solution, and (ii) direct transfer. When the wires are deposited from solution, we first put the chip with as-grown nanowires (as in Figure 2.4C) in 2-propanol (IPA). By low-power ultrasonic agitation the nanowires are released from the growth-chip and suspended in solution. The nanowires in the IPA can now be transferred to the silicon substrate using a reference pipette. The second deposition method, called direct transfer, is even more straightforward than deposition from solution. We gently put the growth chip on top of the oxidized silicon substrate resulting in the direct transfer of nanowires to the

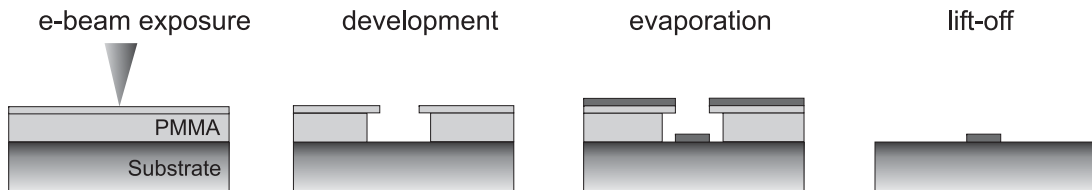


**Figure 2.6:** Schematic of the electrode fabrication process. In the first step a double-layer of e-beam resist (PMMA) is exposed using an e-beam pattern generator (EBPG). Then the exposed areas are dissolved with a suitable developer and a metal film is deposited using e-beam evaporation. In the last step the remaining resist is removed using a solvent (right panel).

silicon substrate.

After nanowire deposition the position of the nanowires on the substrate have to be determined in order to fabricate individual electrodes. This is done by using pre-deposited markers on the silicon substrate. These markers are defined by electron beam lithography, a technique we discuss below. Figure 2.5a shows an SEM image of a silicon nanowire deposited on a substrate with a predefined marker. We have used Computer Aided Design (CAD) software in order to design individual electrodes to the nanowires. An example of a design connecting the nanowire with four Ni contacts is shown in Figure 2.5b.

### Electron-beam lithography

We have used electron-beam lithography (EBL) for defining the electrodes in a layer of resist. This process is illustrated schematically in Figure 2.6 and consists of the following steps: (i) Spinning of resist, (ii) E-beam exposure, (iii) Metal deposition, (iv) Lift-off.

(i) For this thesis we have used a double layer of polymethyl methacrylate (PMMA). The double layer improves the lift-off process due to a better resist profile with an undercut. This results from a higher sensitivity of the bottom layer compared to the top layer. The bottom layer (8% PMMA/MMA in ethyl-L-lactate) is spun for 55 seconds at 3000 rpm and subsequently baked at 175°C for 15 minutes. The top layer (2% 950k PMMA in chlorobenzene) is spun at 4000 rpm for 55 seconds. We use a final bake at 175°C for 60 minutes.

(ii) The CAD design is written in the resist by an e-beam pattern generator (EBPG). Due to the exposure by an electron beam bonds in the polymer are broken and the resist becomes soluble in a developer. We have used methyl-isobutyl-ketone (MIBK):IPA 1:3 as a developer with a development time of 60 seconds. Subsequently, the sample has been rinsed for 60 seconds in IPA.

(iii) Metal deposition is typically done by e-beam evaporation in a vacuum system with a background pressure of  $3 \cdot 10^{-8}$  mBar using deposition rates of typically  $1 \text{ \AA/s}$ . In order to reduce contact resistances between metal contacts and semiconductor nanowires we perform a wet etch just before evaporation. This process consists of a 5 seconds dip in an Ammonium-buffered HF solution (BHF) followed by a rinse in  $\text{H}_2\text{O}$ .

(iv) The final step in the fabrication process is lift-off. In this step the remaining resist is dissolved by immersing the sample in hot acetone ( $55^\circ\text{C}$ ) for 15 minutes. Subsequently, the sample is rinsed in cold acetone and dried with a nitrogen flow. Figure 2.5c shows a scanning electron microscope image of a sample after lift-off.

The samples (with a typical size of  $5 \times 5 \text{ mm}$ ) are glued on a 32-pin chip-carrier using silver paint. The silver paint ensures a good electrical connection between the silicon substrate and the chip-carrier which is important if we use the substrate as a global gate. Electrical connections from the chip to the chip-carrier are made by ultrasonic bonding using Al/Si(1%) wires. Because the electrical contacts on the chip are separated from the substrate by a thin silicon oxide, the bonding has to be done carefully in order to prevent gate leakage. Therefore we use a flat bonding-tool and minimize the force during bonding (equivalent to  $\sim 18$  gram).

### Measurement techniques

Measurements have been performed at low temperatures in order to study the quantum mechanical phenomena of interest. The temperature ranges from 4.2 K down to 30 mK. For measurements between 1.5 and 4.2 K we have used a dip-stick which is immersed in a liquid helium dewar. By pumping on a 1K-pot the temperature can be reduced to 1.5 K. For most other measurements we have used a dilution refrigerator in order to reach temperatures as low as 30 mK.

Although various different systems have been used throughout this thesis to cool down samples, the equipment for the electrical measurements has always been very similar. We have used battery-powered, in-house-built measurement equipment for all our electrical measurements in order to minimize the noise level. Voltage and current sources are computer-controlled and optically isolated from the electrical environment of the sample. Also the outputs of voltage amplifiers and IV-converters are optically isolated from the measurement computer.

# Chapter 3

## Silicon and silicon nanowires

### 3.1 Crystal structure and energy bands

Four of the fourteen electrons in a silicon atom lie in its outer shell. The remaining ten electrons occupy deeper levels,  $n = 1$  and  $n = 2$ , see figure 3.1A. These levels are completely full and have an electronic configuration  $1s^2 2s^2 2p^6$  in which  $s$  and  $p$  are subshells of a level  $n$ . The  $n = 1$  and  $n = 2$  levels can contain ten electrons in total. These levels are tightly bound to the nucleus. The outer shell, the  $n = 3$  level, contains the  $3s$  subshell, with two valence electrons, and the  $3p$  subshell which can contain six electrons, but has only the two remaining valence electrons, as shown schematically in figure 3.1A. The energy of an electron occupying the  $3s$ -orbital is different from an electron occupying the  $3p$ -orbital, since the electrons occupy different energy levels.

Silicon crystallizes in a face-centered cubic (FCC) primitive lattice, the same pattern as diamond. The four electrons in the outer orbital of every Si-atom form a bond with one electron of each of the four neighboring Si atoms. An FCC lattice has one atom on every corner and every face of a cube, and the extra atoms in the Si-lattice are placed at  $(\frac{1}{4}, \frac{1}{4}, \frac{1}{4})a$  with respect to each atom in the FCC lattice, in which  $a$  is the lattice constant. This structure is shown in three dimensions in figure 3.1B. The lines between Si atoms in the lattice illustration indicate nearest-neighbor bonds. The FCC lattice has a body-centered cubic (BCC) lattice in reciprocal  $k$ -space. The Brillouin zone of the FCC lattice is then the Wigner-Seitz cell of the BCC lattice. This is a truncated octahedron, shown in figure 3.1C. Roman letters are used for points on the surface of the octahedron and Greek letters for directions inside the lattice.

When Si atoms form a lattice, the energy levels of the  $3s$  and  $3p$  subshells will interact and overlap, which causes splitting of the energy levels and the formation of two bands. Four quantum states per atom make up the conduction band and

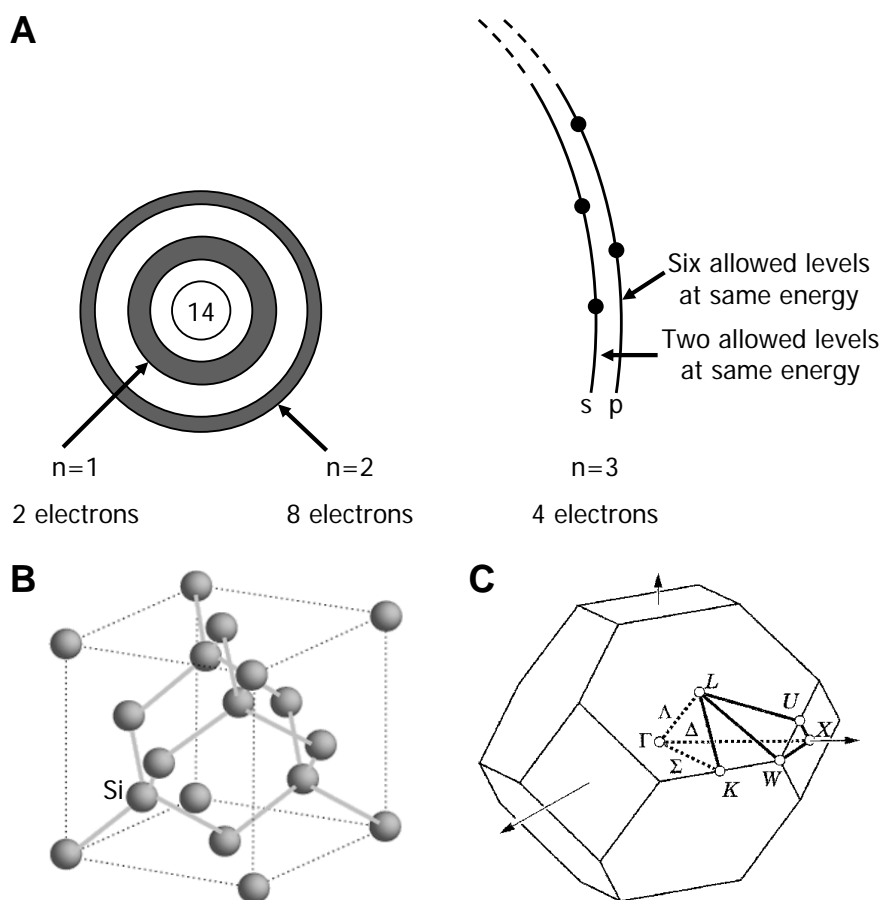


**Figure 3.1: Silicon crystal in real and reciprocal space.** (A) Schematic picture of a single silicon atom and its electrons, spread over three levels, picture based on [28]. (B) 3D plot of the unit cell of the silicon crystal in real space, showing the diamond or Face-Centered Cubic (FCC) lattice, with covalent bonds between all Si atoms. (C) Silicon crystal in reciprocal space. Brillouin zone of the silicon crystal lattice. It is the Wigner-Seitz cell of the BCC lattice.  $\Gamma$  is the center of the octahedron.

four make up the valence band. Figure 3.2A shows the band structure of silicon. The conduction and valence bands are shown versus the different directions in  $k$ -space, denoted by Greek and Roman letters. These directions are taken from the middle of the Brillouin-zone ( $\Gamma$ ), see also figure 3.1C.

In an intrinsic semiconductor the Fermi energy,  $E_F$ , lies in the gap, so both bands are full and there are no free charge carriers. Transport can only occur when electrons are available in the conduction band or holes in the valence band. The energy difference between the conduction and the valence band is called the bandgap energy,  $E_g$ , which is 1.12 eV for bulk silicon at room temperature and increases to 1.17 eV below 50 K. The thermal energy,  $k_B T$ , is much smaller at room temperature ( $\sim 0.03$  eV) than the band gap energy, hence the absence of

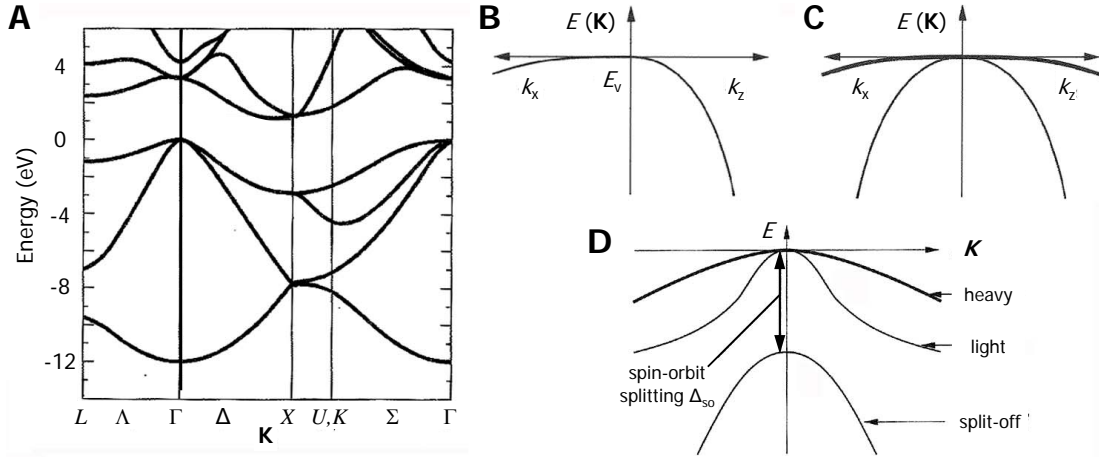


**Figure 3.2: Silicon band structure.** (A) Band structure of silicon in  $\mathbf{K}$ -space. The four lower bands in the valence band, the four upper bands in the conduction band and the band gap energy are shown. (B) Band structure of the  $p_z$ -orbitals only, the band is heavy in the  $k_x$  direction and light in the  $k_z$  direction. (C) Total bands from all three  $p$ -orbitals in the  $k_x k_z$ -plane, which shows a doubly degenerate band ‘heavy’ band and a single ‘light’ band. The bands look identical in the  $k_x k_y$ -plane and the  $k_y k_z$ -plane. (D) Zoom-in on the top of the valence band. The heavy and light holes are degenerate for  $\mathbf{K} = 0$ , but have different masses for small  $\mathbf{K}$ . For large  $\mathbf{K}$ , they converge and form the ‘heavy’ band. The split-off band is separated from this band by the spin-orbit splitting  $\Delta_{so}$ . Figures from [29].

thermally excited free charge carriers. Silicon has an indirect gap, which means that not only an energy change is required to get an electron excited into the conduction band, but also some momentum change. For excitation, a phonon is needed to require the change in momentum, because a photon does not provide a high enough momentum. It is therefore impossible to determine the bandgap of silicon by optical absorption of a photon with a certain wavelength. Besides that, silicon is not a very efficient light emitter.

### Top of the valence band

The different bands for heavy and light holes in the valence band are shown in fig 3.2A. Holes in the top of the valence band have wave functions that display a symmetry similar to the symmetry of  $p$ -orbitals [29]. If we consider a lattice of  $p_z$ -orbitals, carriers in the  $p_z$ -orbital can travel easily in the  $z$ -direction, because the wave functions overlap strongly in this direction. In the  $k_x k_y$ -plane, the overlap is much weaker, carriers travel less freely, and thus the effective mass is higher in these directions, see figure 3.2B. For the  $p_x$ - and  $p_y$ -orbitals, the wave functions

overlap strongly in respectively the  $k_x$  and  $k_y$  direction, and weak in the other directions. The picture of all p-orbitals results in a doubly degenerate upper band for heavy holes and a lower single band for light holes, which is shown in figure 3.2C. The result is that the top of the valence band of silicon consists of a single band for holes traveling slowly, and a doubly degenerate band for fast traveling holes (figure 3.2C).

Bulk silicon has a spin-orbit splitting,  $\Delta_{\text{so}} = 0.044$  eV, which is quite small compared to e.g. GaAs (0.34 eV) and Ge (0.29 eV). Spin-orbit coupling in silicon is even smaller for electrons in the conduction band. This band consists of s-orbitals, which have an angular momentum  $l = 0$ . Since the spin-orbit coupling is proportional to  $l \cdot s$ , it can be neglected and the conduction band is fourfold degenerate. This is known as the valley degeneracy of Si. Since the valence band consists of p-orbitals, the carriers have an angular momentum of  $l = 1$ , and a small spin-orbit coupling is present. When we zoom in on the top of the valence band, the simple picture of figure 3.2A fails. Figure 3.2D shows that a single band is split off from the degenerate band by  $\Delta_{\text{so}}$ . The degenerate band itself is no longer degenerate for all small  $\mathbf{K}$ , but only for  $\mathbf{K} = 0$ . Instead, we have an upper band with heavy holes and a lower band containing light holes [29].

### Effective mass

There has been an inconsistency in literature between commonly used values of the intrinsic carrier concentration, the effective densities of states, the band gap and the carrier effective mass in silicon. The assessment of Green [30] critically evaluates the literature and identifies a self-consistent set of these parameters. Here we present a description of the different types of effective masses based on his work.

Holes with an energy close to a band maximum behave as free electrons, since the E-k relation can be approximated by a parabola. They accelerate in an applied electric field just like a free electron in vacuum. Their wave functions are periodic and extend over the size of the material. The presence of the periodic potential, due to the atoms in the crystal without the valence electrons, changes the properties of the electrons. Therefore, the mass of the electron differs from the free electron rest mass,  $m_0 = 9.11 \cdot 10^{-31}$  kg. For isotropic and parabolic bands the resulting effective mass,  $m^*$ , is defined as

$$\frac{1}{m^*} = \frac{1}{\hbar^2} \frac{d^2 E}{dk^2}. \quad (3.1)$$

Because of the anisotropy of the effective mass and the presence of multiple equivalent band minima in Si, two types of effective mass are used: (i) the effective mass for density of states calculations,  $m_{\text{dos}}^*$ , and (ii) the effective mass

for conductivity calculations,  $m_{\text{cond}}^*$ . The latter is used for the calculation of amongst others mobility, diffusion constants and the shallow impurity levels using a hydrogen-like model. Here we will only use the effective mass for density of states calculations.

The two types are equal if the effective mass is isotropic, e.g. electrons in GaAs have  $m_{\text{e,dos}}^* = m_{\text{e,cond}}^* = 0.067m_0$ . The conduction band in silicon, however, has six equivalent conduction band minima forming ellipsoidal constant energy surfaces with anisotropic effective masses: one longitudinal mass,  $m_l$ , and two transverse masses,  $m_t$ . In that case the density of states effective mass is obtained from

$$m_{\text{e,dos}}^* = M_c^{3/2} \sqrt[3]{m_l m_t m_t}, \quad (3.2)$$

where  $M_c$  is the number of equivalent conduction band minima.  $M_c = 6$  for silicon since it has three doubly degenerate valleys at the  $\Gamma$ -point. With  $m_l = 0.92m_0$  and  $m_t = 0.19m_0$  one finds  $m_{\text{e,dos}}^*$  to be  $1.06m_0$  at 4 K, going up to  $1.09m_0$  at room temperature [30]. The temperature dependence of the effective mass is related to two effects: (i) the shape of the energy-momentum curves changes with temperature as the lattice expands and electron-phonon coupling increases [31]. (ii) The conduction band and valence band move towards each other with temperature or, in other words, the bandgap energy becomes smaller. States away from the band edge approach the other band faster than those at the edge, resulting in flattening of the bands and thus an increased effective mass [32].

In case of isotropic and parabolic valence bands the densities of states effective mass barely changes with temperature and is defined as

$$m_{\text{h,dos}}^* = \{m_{\text{lh}}^*{}^{3/2} + m_{\text{hh}}^*{}^{3/2} + (m_{\text{so}}^* e^{-\Delta_{\text{so}}/k_B T})^{3/2}\}^{2/3}. \quad (3.3)$$

Here  $m_{\text{hh}}^*$ ,  $m_{\text{lh}}^*$  and  $m_{\text{so}}^*$  refer to the effective masses of respectively the heavy hole band, the light hole band and the split-off band with values of  $m_{\text{hh}}^* = 0.54m_0$ ,  $m_{\text{lh}}^* = 0.15m_0$  and  $m_{\text{so}}^* = 0.23m_0$  [33]. In Si, however, the non-parabolic nature of the heavy and light hole bands gives rise to a temperature dependent hole effective mass [34]. If that is taken into account one can make an exact calculation of the effective masses as a function of temperature and calculate  $m_{\text{h,dos}}^*(T)$  as the weighted average:

$$m_{\text{h,dos}}^*(T) = \{m_{\text{lh}}^*{}^{3/2}(T) + m_{\text{hh}}^*{}^{3/2}(T) + m_{\text{so}}^*{}^{3/2}(T)\}^{2/3}, \quad (3.4)$$

yielding a densities of states effective mass of  $1.15m_0$  at room temperature and  $0.59m_0$  at 4 K. There is no analytical expression available, but a polynomial fit to the computed values can be used to get an accurate number of the effective mass [35]. In this work we use the densities of states effective mass to calculate the Fermi energy and the level spacing in a silicon nanowire.

## 3.2 Transport properties

### Doping and mobility

Free charge carriers can be introduced to a semiconductor by impurity doping. Electrons (holes) can be ionized from donor (acceptor) atoms to the conduction (valence) band to create an  $n$ -type ( $p$ -type) semiconductor. Commonly used donors for silicon are As, P and Sb with respective ionization energies of 0.054, 0.045 and 0.043 eV. The acceptor atoms Al, B and Ga require respectively 0.072, 0.045 and 0.074 eV for ionization. Addition of donors or acceptors pulls the Fermi energy up or down compared to the bands, increasing the carrier density and the conductivity. However, impurities have a negative effect on the mobility of the charge carriers,  $\mu$ , which describes the relation between drift velocity,  $v_d$  and applied electric field,  $\vec{E}$ , as  $\vec{v}_d = -\mu\vec{E}$ . It is derived from the Drude model, which assumes that the electron system can be described as an ideal gas, and the motion of electrons is only limited by occasional scattering events [36]. The mobility depends on the mean free time and the effective mass, according to

$$\mu = \frac{e\tau}{m^*}, \quad (3.5)$$

where  $\tau$  is the scattering time.  $\tau$  is determined by various scattering mechanisms, of which lattice and impurity scattering are most dominant. Lattice scattering arises from thermal vibrations of the lattice (phonons), damping out at low temperatures. Impurity scattering results from dopant atoms and dominates at low temperatures. The scattering time goes up with increasing impurity concentration, diminishing the mobility, see Figure 3.3. The difference between electron and hole mobility is mainly due to the degeneracy of the top of the valence band, where  $\tau$  is lowered by interband scattering [37]. Equation (3.5) also makes clear that materials with higher effective masses generally have a lower mobility. E.g. bulk intrinsic InAs has an electron effective mass of  $\sim 0.023m_0$  and a mobility of about  $10^5 \text{ cm}^2/\text{Vs}$  at 77 K, whereas in bulk Si, with  $m_e^* \sim 0.3m_0$ , the mobility is  $\sim 8 \cdot 10^3 \text{ cm}^2/\text{Vs}$ .

### Contacts

In order to incorporate a semiconductor into an electronic circuit, metal contacts are required to connect the active semiconductor region to the external circuit. When a metal and an  $n$ -type semiconductor are brought into contact, alignment of the Fermi levels is accomplished by the transfer of electrons from the semiconductor to the metal, thus pinning the Fermi level below the conduction band of the semiconductor. Close to the interface the semiconductor is depleted of mobile charges, and an electric field builds up in the area where only ionized atoms are

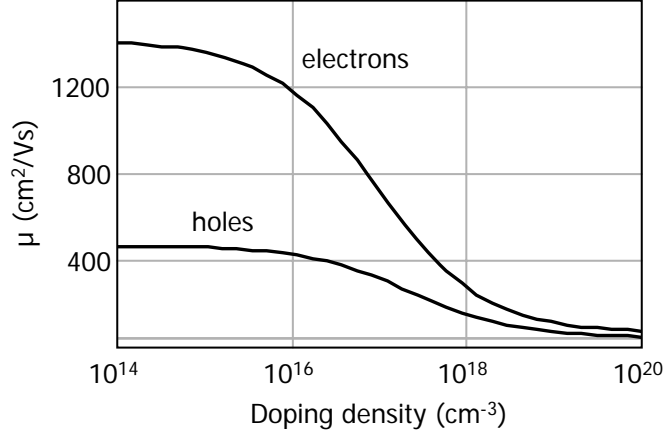


**Figure 3.3: Mobility at room temperature versus doping density in bulk silicon.** The mobility of holes and electrons goes down as the doping concentration increases. Graph from [38].

left. The resulting Schottky barrier is in theory determined by the work functions of metal and semiconductor [28]. The work function  $\phi_m$  is defined as the energy difference between the Fermi level,  $E_F$ , and the vacuum level, and can be regarded as the minimum energy needed to remove an electron from a solid to a point directly outside the surface of the solid. For an  $n$ -type semiconductor the Schottky barrier height is defined as

$$\phi_{B,n} = \phi_m - \chi, \quad (3.6)$$

where  $\chi$  corresponds to the electron affinity of the semiconductor. Similarly, the Schottky barrier of a  $p$ -type semiconductor,  $\phi_{B,p}$ , equals the bandgap energy minus  $\phi_{B,n}$ . Experimental values of the barrier height for different metals with  $n$ -type and  $p$ -type silicon lie typically between 0.3 and 0.9 eV (Table 3.1). While in theory the height of a Schottky barrier is determined by the difference between work functions of metal and semiconductor, in practice the presence of surface states can alter the theoretical value, especially in case of group IV and III-V semiconductors [39].

	Ag	Al	Au	Cr	Ni	NiSi	Pt	W
$\phi_m$ (eV)	4.3	4.25	4.8	4.5	4.5	4.5	5.3	4.6
$\phi_{B,n}$ (eV)	0.78	0.72	0.8	0.61	0.61	0.65	0.90	0.67
$\phi_{B,p}$ (eV)	0.54	0.58	0.34	0.50	0.51	0.45		0.45

**Table 3.1:** The work function of several metals and experimental values of the Schottky barrier height with  $n$ -type and  $p$ -type silicon. Values from [38].

### 3.3 Silicon nanowires

#### Diameter and crystal structure

The preferential crystallographic growth direction of silicon nanowires depends on the diameter. The smallest wires (3–10 nm) grow in the  $\langle 110 \rangle$  direction, wires with diameters of 10–20 nm grow mostly in the  $\langle 112 \rangle$  direction and the bigger ones (20–30 nm) grow in the  $\langle 111 \rangle$  direction [26]. In this research, *p*-Si nanowires were studied with diameters of 5–30 nm.

A nanowire provides confinement for charge carriers in two spatial dimensions, which can lift the degeneracy of the conduction and valence subbands. Since there are only few analytical results we use a simple conceptual picture to explain how the band edges may be pulled apart, see Figure 3.4. Confinement can lead to the ‘heavy’ holes having a lower energy at  $k = 0$  in the valence band. The two bands then cross because the heavy hole energies increase more rapidly with  $k$  than the energies of the ‘light’ holes. The heavy holes then turn out to be lighter for transverse motion than the light holes. If we assume coupling between the two bands, the crossings are in fact anti-crossings.

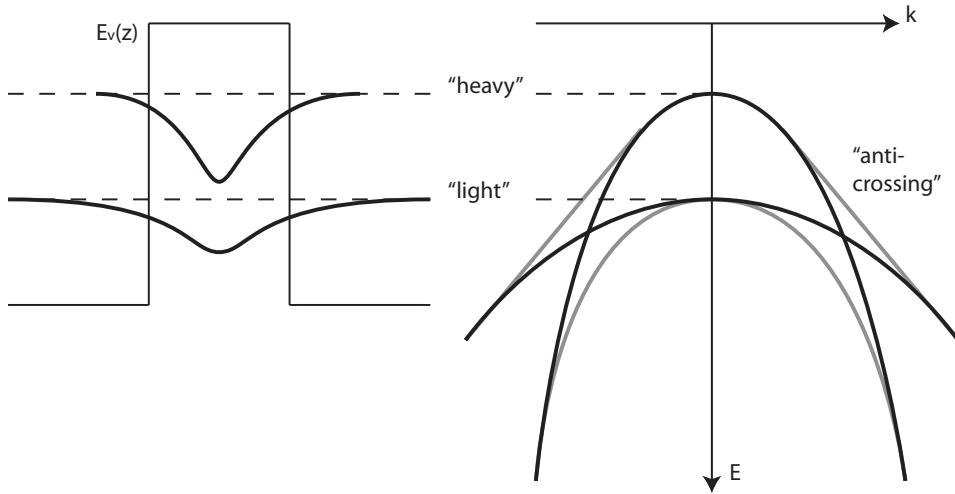


**Figure 3.4:** Conceptual model of valence band in a quantum well, showing how confinement can lift the degeneracy of the heavy and light hole subbands. Coupling between these subbands results in anti-crossing behavior, shown by the grey line. Picture based on [29], page 385.

We can use a simple model to get an order of magnitude estimate of the splitting between the valence subbands. If we assume a 1D box of size  $L$  to be confined by a hard wall potential, the level spacing between the  $N + 1^{th}$  and the  $N^{th}$  subband is [21]

$$\Delta E_N = E_{N+1} - E_N = \frac{(2N + 1)\pi^2 \hbar^2}{2m^* L^2}. \quad (3.7)$$

Based on a densities of states effective mass at 4 K of  $0.59m_0$  and a 6 nm diameter,  $E_2 - E_1 = 53$  meV. If the splitting between the first and second subband is greater than the Fermi energy, we can consider the nanowire as a one-dimensional system. The Fermi energy can be written as

$$E_F = \frac{\hbar^2 k_F^2}{2m^*}, \quad (3.8)$$

where  $k_F$  is the Fermi wave number. The Fermi wave vector in one dimension is  $k_{F-1D} = n\pi/2$ , resulting in a one-dimensional Fermi energy of  $E_{F-1D} = 13$  meV for a carrier density of  $10^{19} \text{ cm}^{-3}$ . Since  $E_F < E_2 - E_1$ , only the lowest subband is filled and we have one-dimensional transport. Figure 3.5 plots the Fermi energy  $E_F$  and the level spacing energy  $E_2 - E_1$  in the radial direction as a function of wire diameter for various carrier densities. Calculations of the sub-

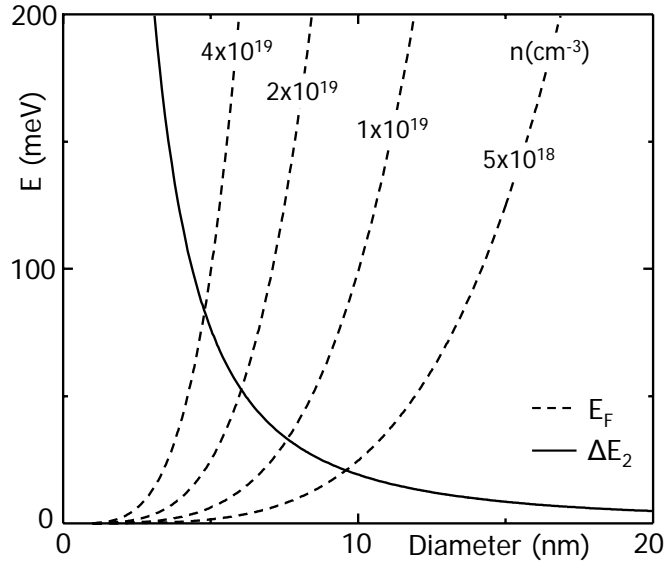


**Figure 3.5: Dimensionality of silicon nanowires.** The Fermi energy  $E_F$  and the level splitting energy between the first and second energy level  $\Delta E_2$  as a function of diameter  $d$ . Curves for  $E_F$  are made for various carrier densities.

band structure using tight-binding models support this conceptual picture, but give smaller values for the subband splitting. The energy difference between the first and second valence subbands in 3 nm diameter Si nanowires is theoretically found to be  $\sim 18$  meV [40, 41].

### Doping and mobility

The incorporation of dopant atoms in silicon nanowires is largely determined by the ratio of the precursor gases, silane and e.g. diborane. The boron-doped silicon wires in this research were grown with an atomic feed-in ratio of Si:B = 4000:1 and

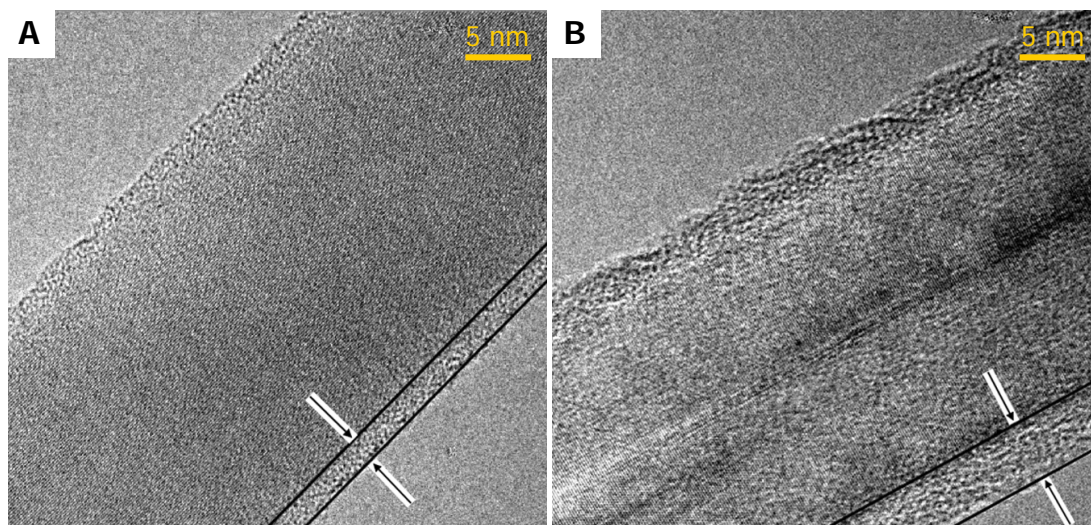


**Figure 3.6: Surface oxide of silicon nanowires.** (A) HR-TEM image of a silicon nanowire with a diameter of 25 nm. The native oxide shell is about 2 nm thick. (B) HR-TEM image of a 25 nm diameter silicon nanowire after 10 min oxidation at 600°C in an O<sub>2</sub>-atmosphere. The oxide shell has grown to a thickness of 4 nm.

3000:1, resulting in a carrier density of  $\sim 10^{19} \text{ cm}^{-3}$  according to [42] and our own experience [43]. The presence of  $\sim 10^{19} \text{ cm}^{-3}$  carriers reduces the hole mobility of bulk Si to below  $80 \text{ cm}^2/\text{Vs}$  (Figure 3.3). One would expect an even lower number for Si nanowires due to increased surface roughness scattering: since the surface-to-volume ratio is much higher, silicon nanowires are more susceptible for local potential fluctuations than planar silicon. After growth, silicon nanowires have a thin amorphous surface oxide of 1-3 nm, see Figure 3.6A. Surface defects in SiO<sub>2</sub> or molecules from the ambient adhering to the oxide can induce potential fluctuations, increasing the scattering rate and thus lowering the mobility. In order to passivate these potential fluctuations we terminate the surface during fabrication by exposing the nanowires to oxygen for ten minutes at 300°C, after which the time in ambient is minimized.

Hole mobilities of 20-30 nm diameter nanowires are found to be  $10\text{-}50 \text{ cm}^2/\text{Vs}$  [43], as expected. However, the mobility of 3-10 nm diameter nanowires is roughly  $100\text{-}500 \text{ cm}^2/\text{Vs}$ , an order of magnitude bigger. The origin may be found in the radial confinement, which can lift the degeneracy of the valence subbands [40, 41] and therefore reduce intersubband scattering. Consequently, the decrease in scattering rate enhances the mobility, see equation (3.5).

Below a certain diameter the dopant atoms introduced during nanowire growth may be driven to the surface [44, 45]. In order to investigate this, we have cultivated the SiO<sub>2</sub> shell by means of dry oxidation at elevated temperatures. The

oxidation of Si nanowires is not constant over time: after a first rapid oxidation, the oxygen molecules have to diffuse through the SiO<sub>2</sub> layer, which limits the oxide growth [46]. Exposure of silicon nanowires to an O<sub>2</sub>-atmosphere for 10 minutes at 600°C results in an oxide shell of  $\sim 4$  nm, see Figure 3.6B. We have made contacts to another set of nanowires after exposure of 30 minutes at the same temperature, see Figure 3.7. The two-terminal resistances of the vast majority of these devices are greater than 100 M $\Omega$ , whereas devices of which the surface has only been passivated (see above) have two-terminal resistances of below 1 M $\Omega$ . The dopant atoms have probably been oxidized as well, resulting in an effectively lower carrier density and hence a lower conductance.

#### Contacts

Frequently used contact metals for *p*-type and *n*-type silicon nanowires are Al/Au [47, 48], Ti/Au [49, 50, 51] and Ni [45, 52, 53, 54]. We have tried three different contacting schemes for *p*-type silicon nanowires, namely Ti(100nm)/Al(10nm), Ti(1–2nm)/Pd(100nm) and Ni(100nm). Figure 3.7 shows two scanning electron micrographs of nanowires with Ti/Al contacts. Near each contact the wire is thinner due to the removed SiO<sub>2</sub> shell. The oxide has been etched with buffered hydrofluoric acid prior to metal evaporation, resulting in a thinner piece of nanowire near the contacts and a trench that has been etched off the substrate.

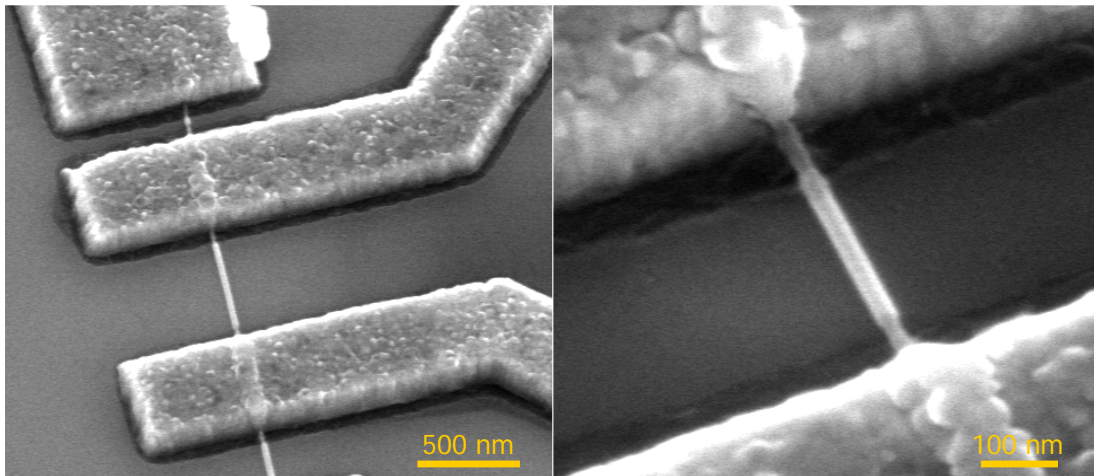


**Figure 3.7: Etched surface oxide of silicon nanowires.** Scanning Electron Micrographs of silicon nanowire devices with Ti/Al (100 nm/10 nm) contacts. The surface oxide has been cultivated to 6–7 nm by dry oxidation for 30 min at 600°C. The nanowire is thinner near the contact, where the SiO<sub>2</sub> shell has been etched prior to metal evaporation.

All three metallization schemes generally result in contact resistances of 10–50 k $\Omega$  when deposited on nanowires with diameters of 15–30 nm, see [43]. The interface resistance can be further reduced by rapid thermal annealing at temperatures between 300–400°C, which stimulates alloying of metal and semiconductor to form a silicide. On 5–10 nm diameter wires the above mentioned metallizations result in Schottky barriers of 0.5–1 V without annealing. In case of Ni and Pd the elevated temperatures induce radial and longitudinal diffusion into the nanowire, leading to an effectively shorter Si channel lengths and two-terminal resistances between 100 k $\Omega$  and 5 M $\Omega$ .

# Chapter 4

## Silicon nanowire quantum dots

The observation of quantum states in silicon devices requires small structures because of the relatively high electron and hole effective mass compared to e.g. InAs or GaAs. Additionally, planar silicon devices show localization on short length scales, caused by potential fluctuations which can arise from structural roughness or dopant fluctuations. These often result in multiple dots connected in series. Nearly all reports so far have been on Si quantum dots greater than 50 nm, e.g. in Si MOSFETs [55, 56, 57], silicon-on-insulator structures [58, 59, 60] and Si/SiGe heterostructures [61, 62]. In these three systems excited states have been observed only recently [63, 64, 65]. They were all preceded by the results on silicon nanowire quantum dots in 2005 [45], which include excited-state spectroscopy, spin spectroscopy and a strong indication of the realization of a single-hole dot. We have continued this work, and gained a better understanding of the specific system. This has allowed us to realize the first experimental identification of the first four spin states in a silicon quantum dot, which we will present in the next chapter. We start by giving a full description of the advantages and disadvantages of Si nanowire quantum dots in this chapter.

We have measured many single quantum dots in *p*-type silicon nanowires, defined by Schottky tunnel barriers with Ni and NiSi contacts. Quantum dots shorter than 30 nm with pronounced excited states have been realized, which readily allow spectroscopy of at least ten consecutive holes. We can make a reliable estimate of the dot length by comparing the measured backgate capacitance to the capacitance computed with a model based on the Poisson equation. The Si channel lengths visible in SEM images match the dimensions predicted by the model. Finally, we show the difficulty of creating a single-hole silicon quantum dot: many single dots split up in two dots upon reaching the few-hole regime. So far only very short dots ( $< 12$  nm) have allowed identification of the last charge.

## 4.1 Two types of Si nanowire quantum dots

In this section two approaches for fixing the Si channel length are compared: (i) Si nanowires with evaporated Ni contacts which are defined by electron-beam lithography and (ii) NiSi–Si–NiSi nanowires, fabricated by thermally induced diffusion of Ni into Si nanowires. Silicon nanowire devices are prepared as described in Chapter 2. During evaporation we deposit Ni contacts, leaving a Si channel of 50–300 nm uncovered, see Figure 4.1A. In order to make NiSi–Si–NiSi nanowires the samples are annealed in sequential steps of 20–30 seconds at 380 °C and 410 °C, to induce radial and longitudinal diffusion of Ni into the Si nanowire. From both Ni contacts a NiSi segment is formed in the nanowires with lengths of 100–150 nm, depending on diameter, temperature and time. Details about the results for different annealing temperatures and times can be found in ref. [66]. The remain-

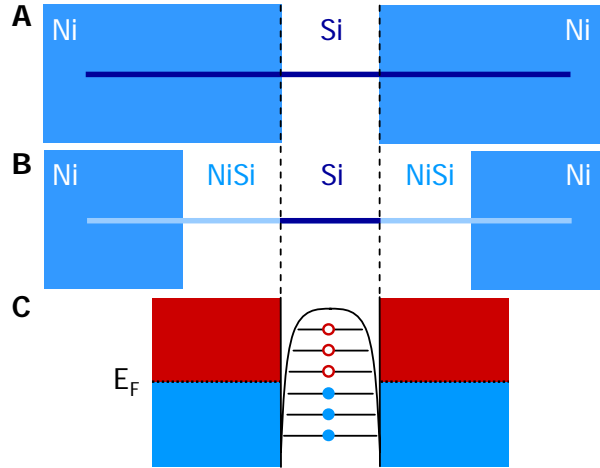


**Figure 4.1: Two types of Si nanowire quantum dots.** Schematic top view of a Si nanowire quantum dot with Ni leads (A) and with NiSi leads (B). Here the Ni has diffused into the Si nanowire during a two-step annealing process. (C) Schematic of the corresponding Schottky tunnel barriers that define the quantum dot. Occupied (empty) hole states are indicated in red (blue).

ing Si section is connected to the lithographically defined Ni contacts by two NiSi leads, see Figure 4.1B. These devices have room-temperature resistances varying from 100 k $\Omega$  to 5 M $\Omega$ . Some nanowires are fully transformed into the metal NiSi having room-temperature resistances of 1–5 k $\Omega$ , corresponding to  $\rho \sim 10 \mu\Omega\text{cm}$ , consistent with values found in NiSi nanowires [67] and large single crystals [68]. The sensitivity of the potential landscape in silicon nanowires to surface states demands clean fabrication to keep a flat valence band profile [66]. Otherwise fluctuations of the potential in the Si channel can give rise to the unintentional formation of extra tunnel barriers and thus in multiple-dot behavior.

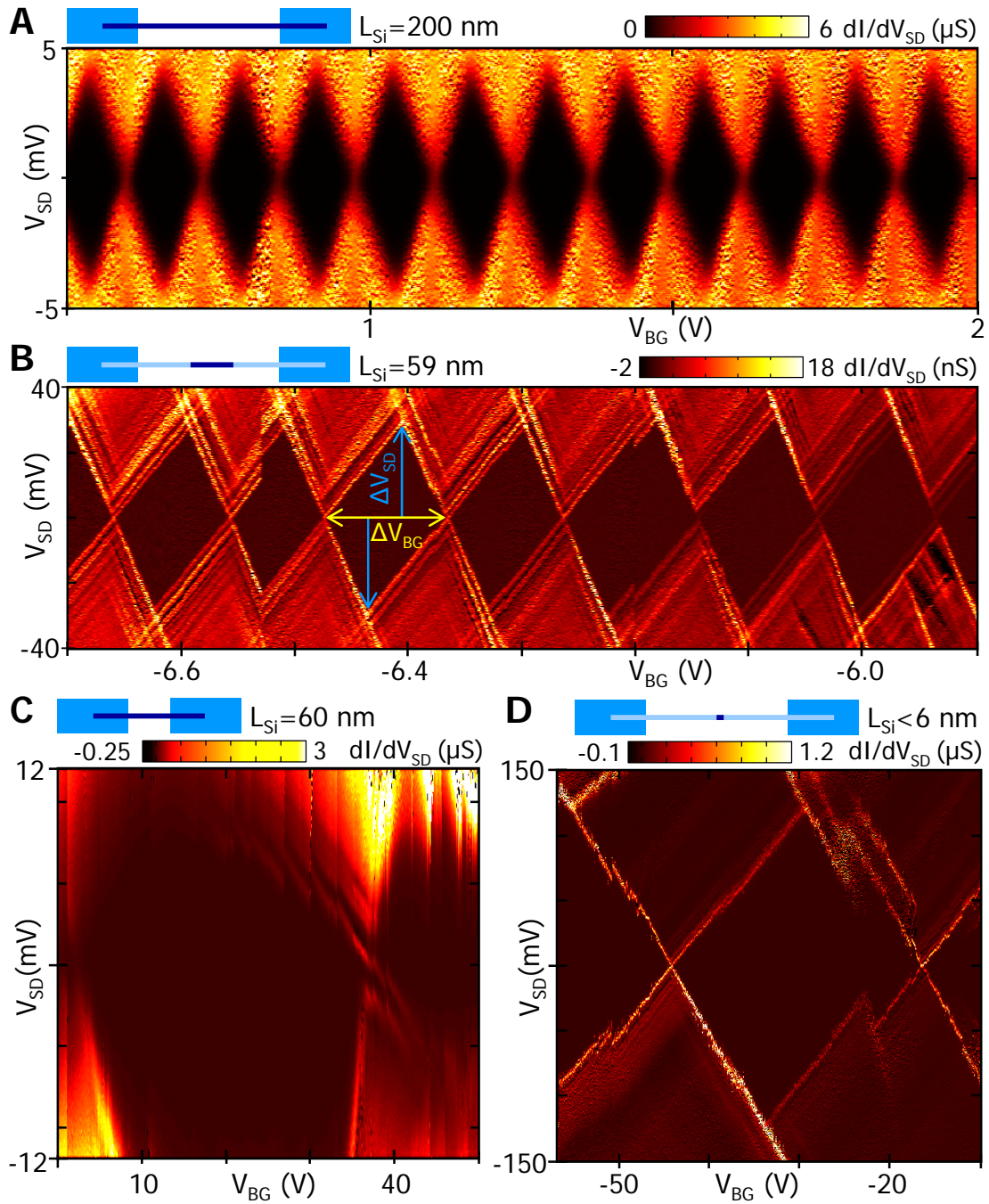


**Figure 4.2: Single quantum dots of varying lengths.** Stability diagrams of four Si nanowire quantum dots, measured at 2 K (A-C) and 20 mK (D). (A,C) Ni-Si-Ni quantum dots of 200 and 60 nm, as defined by electron-beam lithography. (B,D) NiSi-Si-NiSi nanowire quantum dots with estimated lengths of 59 and 6 nm, see next section. The devices A, C and D were fabricated on substrates with  $SiO_2$  thicknesses of 285 nm and device B on 50 nm thick  $SiO_2$ .

## 4.2 Single quantum dots of varying lengths

The Ni–Si or NiSi–Si interfaces in each device form the Schottky tunnel contacts between the metallic leads and the  $p$ -Si quantum dot, see Figure 4.1C. We have measured 6 Ni–Si–Ni and 30 NiSi–Si–NiSi single quantum dots on substrates with SiO<sub>2</sub> thicknesses of 50 and 285 nm. In Figure 4.2 the differential conductance,  $dI/dV_{SD}$ , of four devices of varying sizes is plotted versus source-drain voltage,  $V_{SD}$ , and backgate voltage,  $V_{BG}$ . We will refer to devices A, B, C and D for the respective Figures 4.2A, B, C and D.

All four subfigures consist of diamond-shaped regions in which the current is zero due to Coulomb blockade and the number of holes,  $N$ , is fixed, see Chapter 2. From these Coulomb diamonds we have derived the involved capacitances in Table 4.1. The backgate-to-dot capacitance,  $C_{BG}$ , is calculated as  $C_{BG}=e/\Delta V_{BG}$ , where  $\Delta V_{BG}$  is the voltage needed to add a single charge, see Figure 4.2B. We assume that the level spacing is much smaller than the charging energy. The diamond edges have slopes of  $-C_{BG}/C_S$  and  $C_{BG}/(C-C_S)$ , where  $C$  is the sum of all capacitances to the dot and  $C_S$  ( $C_D$ ) is the capacitance between dot and source (drain) [69]. If we assume that no other gates have a significant capacitive coupling to the dot  $C=C_S+C_D+C_{BG}$ . We also compute the gate coupling factor,  $\alpha$ , as  $E_{\text{add}}/\Delta V_{BG}$ , where the addition energy,  $E_{\text{add}}$ , is half the sum of the maximum and minimum  $V_{SD}$  of a diamond, indicated by blue arrows in Figure 4.2B. The length,  $L$ , of the NiSi–Si–NiSi quantum dots is estimated by means of a capacitance model, see next section.

The stability diagrams of the Ni–Si–Ni quantum dot in Figure 4.2A and of the NiSi–Si–NiSi nanowire quantum dot in Figure 4.2B both display a set of uniform Coulomb diamonds. Besides a longer Si channel, device A also has a diameter of  $\sim 20$  nm, versus  $\sim 6$  nm for device B. The source and drain capacitances of device A are about ten times bigger than those of device B, because of the order

Device	Lead metal	$L$ (nm)	$C_{BG}$ (aF)	$\frac{1}{2}(C_S+C_D)$ (aF)	$\alpha$ (eV/V)
A	Ni	200	1.3	19.4	0.032
B	NiSi	59	1.6	2.1	0.28
C	Ni	60	0.005	4.0	0.001
D	NiSi	< 6	0.005	0.64	0.004

**Table 4.1:** Parameters of the quantum dots of Figure 4.2. The length of the Si dots with NiSi leads is estimated as explained in the next section. We estimate  $C_{BG}$  from a single diamond, see text. For Figures 4.2C and 4.2D we have used the only full Coulomb diamond to determine the capacitances.

of magnitude difference in volume. The backgate capacitances, however, have comparable values. This can be understood by the difference in SiO<sub>2</sub> thickness, and the fact that in a NiSi–Si–NiSi nanowire the leads and quantum dot have comparable diameters. This strongly reduces screening of the backgate compared to lithographically defined leads.

Outside the diamonds of device B many lines of increased conductance run parallel to the edges, whereas the conductance of device A shows no such structure. The origin can be found in the availability of extra channels for transport. Lines ending on the  $N^{\text{th}}$  diamond are attributed to the excited states of the  $N^{\text{th}}$  hole, see Chapter 2. The magnitude of the excited states depends on the dot size. We can use a simple hard-wall potential to get an order or magnitude estimate of the level spacing, see equation (3.7). For a 200 nm quantum dot with an effective hole mass of  $0.59m_0$ ,  $\Delta E_2 = 0.048$  meV. Such a small level spacing is washed out by the thermal energy,  $k_B T \sim 0.2$  meV. However, in case of a 59 nm dot  $\Delta E_2 = 0.55$  meV is bigger than  $k_B T$ , and corresponds well to the observed excited state lines of about 1-2 meV.

The fact that excited states are visible is a direct consequence of the small size of quantum dot B. We have also fabricated Ni–Si–Ni dots of the same size, see Figure 4.2C. The comparable source and drain capacitances confirm the similarity of the dot sizes. However, the backgate voltage needed to add one hole is about 30 V, a factor of 300 more than needed for device B. Performing spectroscopy of four consecutive holes thus requires a change in backgate voltage of more than 100 V. This is problematic since sweeping  $V_{BG}$  over a large range increases the chance of gate leakage and charge rearrangements on the SiO<sub>2</sub>. Both can lead to potential fluctuations and thus unstable devices, see Figure 4.2C.

On the other hand, we have measured 22 single NiSi–Si–NiSi quantum dots shorter than 50 nm. Even dots with channel lengths between 10 and 20 nm need less than 2 V to add a single charge and thus readily allow spectroscopy of *at least* ten holes. Figure 4.2D shows a stability diagram of the shortest single NiSi–Si–NiSi dot we measured, with a length below 6 nm. The confining potential used above yields a level spacing of 53-120 meV for a dot of 4-6 nm. This value is close to the measured excited state of 120 meV ending on the leftmost diamond and thus confirms the ultra-small size of the dot. Just like in device C the peak-to-peak distance is 30 V on the backgate, despite the fact that the dot is more than an order of magnitude shorter than device C. Also, the stability of device D compared to device C over this gate voltage range is striking and has allowed us to resolve the Zeeman energy of the first hole, see Figure 5.6.

### 4.3 Capacitances and dot lengths

A cylinder-on-plate model can be used to connect the measured backgate-to-dot capacitance to the Si dot length as

$$C_{BG} = \frac{2\pi\epsilon_0\epsilon_r L}{\ln(2t/r)}, \quad (4.1)$$

where  $t$  is the backgate distance and  $r$  is the nanowire radius, see e.g. [70]. In this model  $C_{BG}$  increases linearly with the nanowire length, see Figure 4.3A. However, the capacitance is smaller in real devices because the metallic contacts screen the electric field induced by the backgate. To get around this, the Poisson equation is projected onto a discrete grid of the full three-dimensional geometry of realistic devices. The type of material as well as the dielectric constant and the fixed charge are defined for every grid point. The output of the numerical iteration contains the potential and electric field lines in all three dimensions, as well as the induced charge on every surface. Since the system is linear, the capacitance between two surfaces can be calculated by dividing the induced charge on one surface by the voltage on another. Details can be found in ref. [71].

With this Poisson solver we have calculated the backgate-to-dot capacitance of the Si nanowire devices used in this research, see Figure 4.1A and B. In case of the Ni–Si–Ni devices we varied the Ni contact separation from 0 to 300 nm, connected to each other by a 6 nm diameter Si nanowire. For the NiSi–Si–NiSi nanowire devices we have used a constant distance of 300 nm between the Ni contacts which sandwich the nanowire with a Si (NiSi) diameter of 6 nm (8 nm). We have varied the length of the Si dot from 0 to 300 nm, resulting in two NiSi leads of 150 to 0 nm. The computed  $C_{BG}$  versus the Si dot length has three regimes for NiSi–Si–NiSi nanowires, see Figure 4.3A: (i) For dot sizes between 6 and 250 nm  $C_{BG}$  increases proportionally with the length, by roughly 27 aF/ $\mu\text{m}$  (9 aF/ $\mu\text{m}$ ) on substrates with 50 nm (285 nm) SiO<sub>2</sub>. (ii) In case of Si dot lengths above 250 nm the slope of  $C_{BG}(L)$  becomes less steep due to screening by the wide Ni contacts. (iii) Below 6 nm the diameter becomes comparable to the dot length and the electric field lines from the backgate are screened by the NiSi leads, see the zoom in Figure 4.3B.

In case of Ni–Si–Ni dots we have only performed calculations for substrates with 285 nm SiO<sub>2</sub>, see Figure 4.3A. At a channel length of 300 nm the calculated capacitance is the same as for NiSi–Si–NiSi dots, because the latter have no NiSi leads left in the model and the geometries are thus equal. Below 300 nm the capacitance of Ni–Si–Ni dots drops rapidly, whereas the values of dots with NiSi leads decreases slowly. At dot lengths below 40 nm there is more than a factor

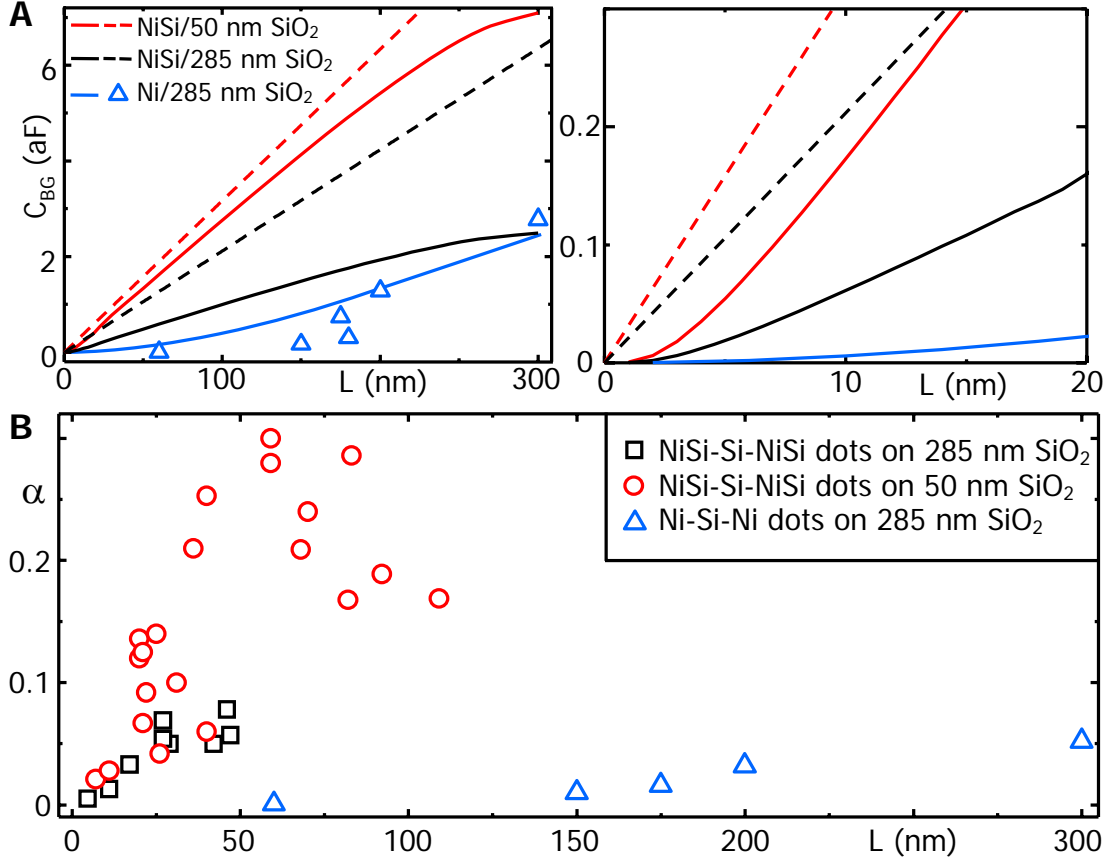


**Figure 4.3: Capacitances and dot lengths.** (A) Computed values of the backgate capacitance for NiSi–Si–NiSi dots on substrates with 50 nm (red) and 285 nm (black) thick  $\text{SiO}_2$ , and Ni–Si–Ni dots on substrates with 285 nm thick  $\text{SiO}_2$  (blue). Dashed lines are calculated with a cylinder-on-plate model, straight lines with a model based on the Poisson equation, which includes screening. Blue triangles are measured backgate capacitances on Ni–Si–Ni quantum dots. Right panel shows a zoom at dot lengths below 20 nm. (B) Experimentally found gate coupling factors versus dot length for all types of quantum dots. The Ni–Si–Ni dots have much smaller  $\alpha$ -values than NiSi–Si–NiSi dots, as a result of stronger screening of the electric field induced by the backgate.

of 5 difference between the capacitances of NiSi–Si–NiSi and Ni–Si–Ni dots. The measured capacitance values of the latter correspond well to the computed values and the model thus gives a reliable estimate of the dot length.

Along these lines we can connect the measured backgate capacitance of a NiSi–Si–NiSi device to a dot length. We calculate the capacitance from Coulomb diamonds at high hole numbers, where the tunnel barriers are thinnest and accordingly the size of the orbital wave functions corresponds best to the Si channel length. Scanning electron micrographs reveal silicide segments as bright regions which sandwich a darker section of Si, see Figure 4.4. When the channel length

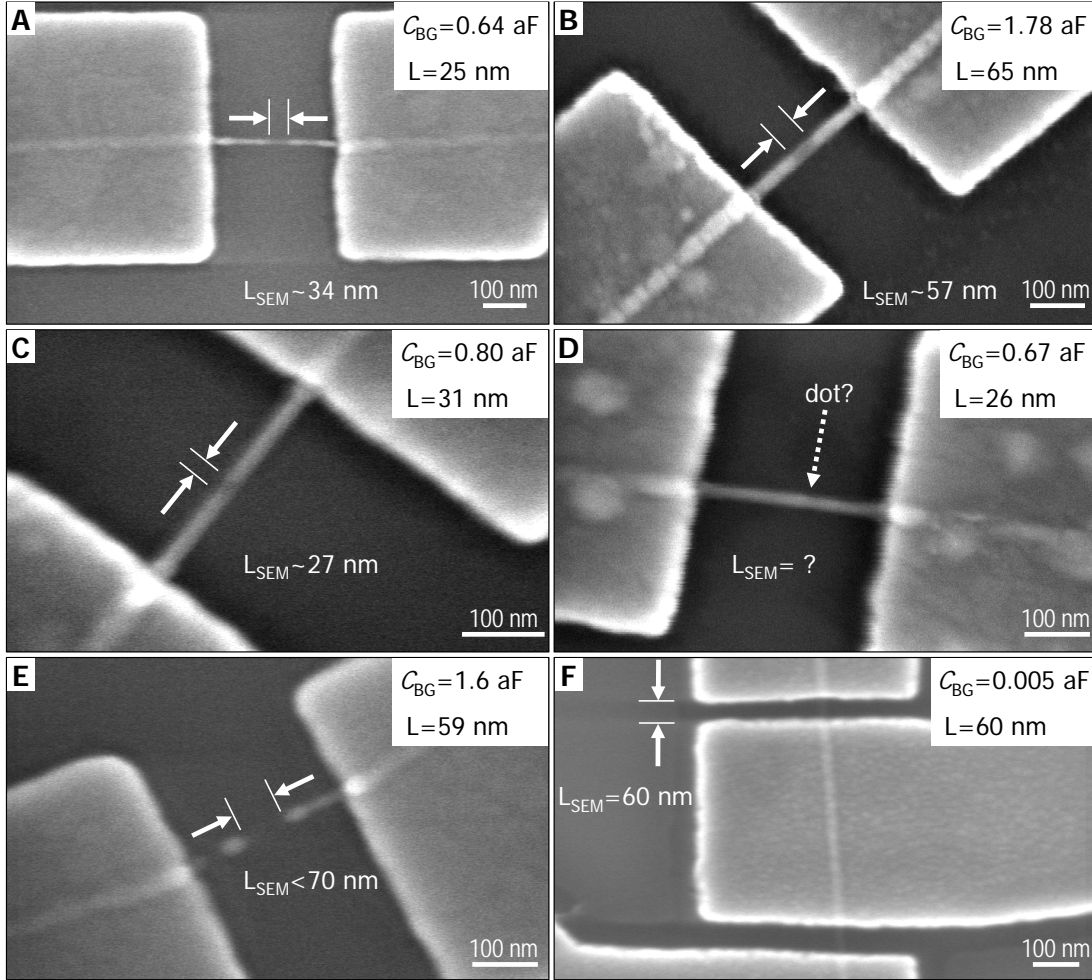


**Figure 4.4: Dot lengths in SEM.** SEM images of five different NiSi–Si–NiSi nanowire quantum dots (**A**, **B**, **C**, **D**, **E**) measured on substrates with 50 nm SiO<sub>2</sub> and one Ni–Si–Ni quantum dot (**F**) measured on substrates with 285 nm SiO<sub>2</sub>. The image in (**D**) does not reveal a distinct Si segment. The device in (**E**) blew up after the measurements, but the remaining NiSi gives an upper bound for  $L$  of 70 nm. Measurements of the devices in (**C**), (**E**) and (**F**) are shown in respectively Figure 5.1D, 4.2B and 4.2C. Insets: the backgate capacitance deduced from the measurements, and the corresponding model length, see Figure 4.3.

measured in SEM images is compared to the length predicted by the model we obtain an accuracy within 30% in different devices. In some cases we cannot exactly determine the dot in the SEM images, e.g. Figure 4.4D and E.

Additionally we have derived the gate coupling factors from the measurements and plotted them versus dot length in Figure 4.3C. In this geometry the gate coupling factor is a good measure for the strength of the screening. This explains the distinct difference in  $\alpha$ -values between NiSi–Si–NiSi dots and Ni–Si–Ni dots.

In case of the latter enormous screening due to the wide Ni contacts strongly complicates measuring Si quantum dots smaller than 50 nm. Clearly we have been able to fabricate many NiSi–Si–NiSi dots with lengths below 50 nm, which readily allow spectroscopy of at least ten holes.

In conclusion, we have demonstrated the realization of single Si quantum dots with Ni and NiSi contacts. In Ni–Si–Ni quantum dots we have strong control over the size of the quantum dots down to 50 nm channel lengths. However, the metallic leads severely screen electric field lines induced by a backgate, whereas the leads and quantum dot have comparable diameters in a NiSi–Si–NiSi nanowire. Screening from contacts at NiSi–Si junctions is very small compared to Ni–Si junctions and thus the backgate has a stronger capacitive coupling. A capacitance model based on the Poisson equation gives a reliable estimate of the dot length in NiSi–Si–NiSi nanowire quantum dots. An extra advantage is that this technique allows the formation of dots shorter than 30 nm with pronounced excited states. A drawback is the variation in Ni diffusion per device and therefore the lack of exact control of the dot length.

## 4.4 Towards the few-hole regime

Finally, we have attempted to isolate a single hole on a Si quantum dot by driving the gate voltage to more positive values. The result is shown for two devices in Figure 4.5A and B with estimated dot lengths of respectively 17 nm and 29 nm. More Coulomb diamonds at a higher resolution of the device in Figure 4.5B can be found in Figure 5.1C. At higher hole numbers, both stability diagrams consist of closing Coulomb diamonds, a signature of single-dot behavior. Small potential fluctuations in the bottom of the potential well will not be felt and the orbital wave functions spread over the entire width of the quantum well, see Figure 4.5C. As the gate voltage is increased, holes leave the dot and some diamonds no longer close, e.g. the diamonds numbered 2–6 in Figure 4.5A. This can be understood by fluctuations of the potential in the Si channel resulting in the formation of an extra tunnel barrier. In practice it turns out that most devices split up into two dots before we reach the few-hole regime.

We attribute the local potential perturbations to impurities or defects in the environment of the dot. So far, only very short dots have allowed positive identification of the last charge, see Figures 5.2, Figure 5.6 and Figure 4 in ref. [45]. The estimated dot lengths of these devices are respectively 12 nm, 5 nm and 9 nm. Shorter channels increase the chance to get a single-hole dot. First for statistical reasons: the chance of having e.g. an impurity or a defect right next

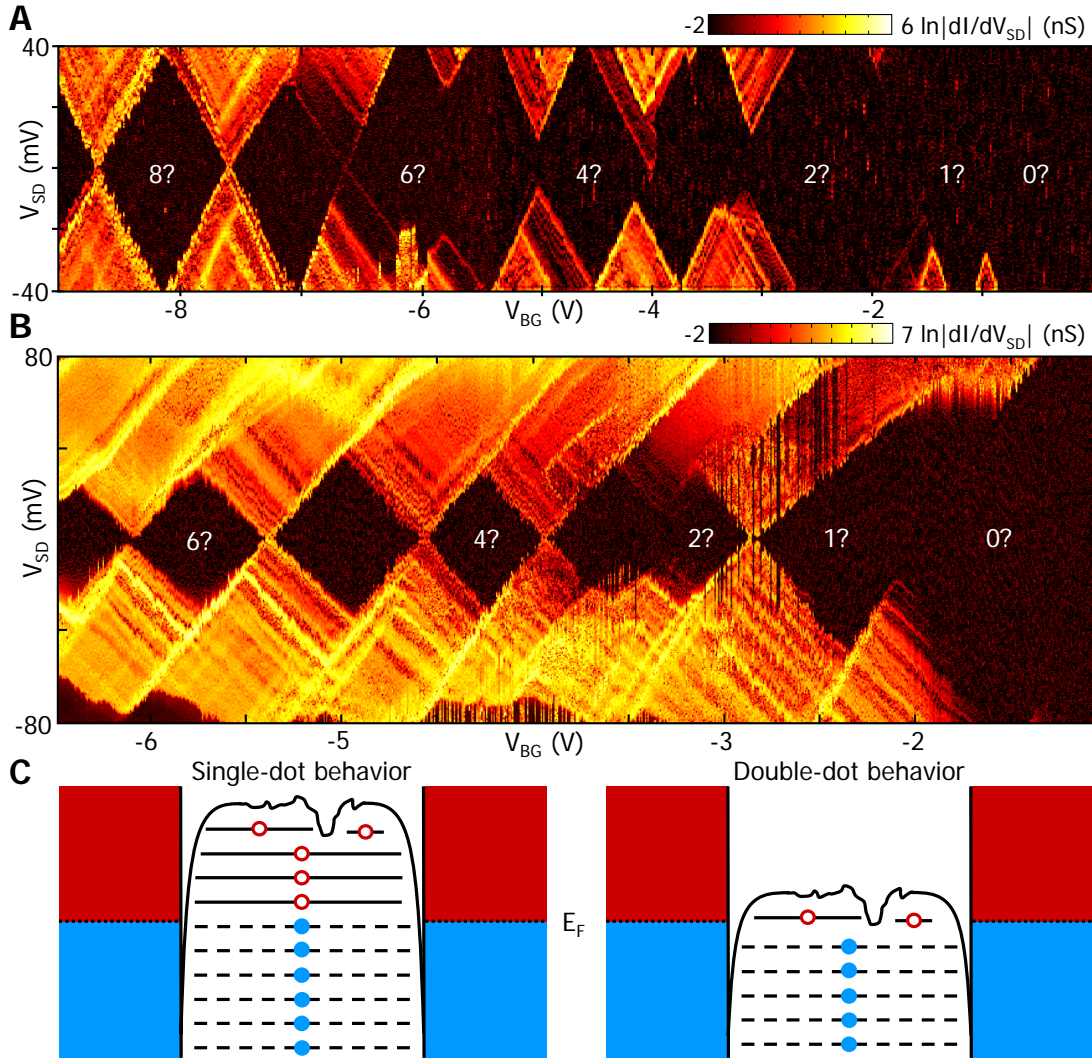


**Figure 4.5: Towards the few-hole regime.** (A, B) Stability diagrams of two Si nanowire quantum dots near depletion. Both devices display single-dot behavior at higher hole numbers and double-dot behavior at lower hole numbers. (C) Schematic diagram of a  $p$ -type quantum dot with a fluctuation in the bottom of the potential well, explaining the transition from single-dot behavior at higher hole numbers (left panel) to double-dot behavior at lower hole numbers (right panel).

to the dot decreases with the channel length. Secondly, if the confining potential is determined by two Schottky barriers *without* a flat valence band in between, the quantum well is less sensitive to modulations in the electrostatic potential due to the steepness of the bent valence band.

# Chapter 5

## Few-hole spin states in a silicon nanowire quantum dot

F. A. Zwanenburg, C. E. W. M. van Rijmenam, Y. Fang,  
C. M. Lieber & L. P. Kouwenhoven

We report an extensive experimental study of single spins in silicon quantum dots. We perform electronic transport measurements on 30 single quantum dots in silicon nanowires, defined by Schottky barriers with NiSi leads. Excited-state spectra of three quantum dots are presented, one of which shows control of the hole number down to one. Detailed measurements at magnetic fields ranging from 0 to 9 T reveal the Zeeman energy at both the  $0 \leftrightarrow 1$  and  $1 \leftrightarrow 2$  hole transition, corresponding to a g-factor close to the Si bulk value. By combining the observation of Zeeman splitting with our knowledge of the absolute number of holes, we are able to determine the ground-state spin configuration for one to four holes occupying the dot. We find a spin filling with alternating spin-down and spin-up holes which is confirmed by magnetospectroscopy from 0 to 9 T.

---

The results in this chapter will be submitted for publication.

## 5.1 Introduction

Long spin lifetimes are crucial for applications such as spintronics [4] and, more specifically, quantum computation with single spins. The proposal to use single spins as quantum bits [10, 11] exploits an optimal combination of the spin and charge degree of freedom [69]. The potential of this spin qubit is underlined by the recent demonstration of coherent control of one [13] and two [12] spin states in quantum dots in GaAs/AlGaAs heterostructures. Most experiments have focused on quantum dots formed in III-V semiconductors; however, electron spin coherence in those materials is limited by hyperfine interactions with nuclear spins and spin-orbit coupling. Group IV materials are believed to have long spin lifetimes because of weak spin-orbit interactions and the predominance of spin-zero nuclei. This prospect has stimulated significant experimental effort to isolate single charges in carbon nanotubes [72, 73], Si FinFETs [74] and Si nanowires [45]. The recent observation of spin blockade in Si/SiGe heterostructures is argued to confirm the predicted long-lived spin states [65].

In this work the spin states of single charges in silicon quantum dots are studied by means of low-temperature electronic transport experiments, for the first time to the level of individual spins. We have measured 30 single Si nanowire quantum dots with pronounced excited states we present stability diagrams of three representative devices. The quantum dots are defined by Schottky barriers with NiSi leads. Both a backgate and a side gate allow control of the number of charges down to a single hole in the dot. We observe the Zeeman energy of the first two holes at magnetic fields ranging from 0 to 9 T, from which we deduce a  $g$ -factor close to the Si bulk value. Magnetospectroscopy of the first four holes allows determination of the successive spins that are added to an empty dot and reveals a spin filling with alternating spin-down and spin-up holes. The isolation and identification of a single spin in silicon demonstrated here constitutes an important step towards the realization of spin qubits in a material with a long spin coherence time.

Single-crystal  $p$ -type Si nanowires are prepared by a gold nanocluster mediated vapor-liquid-solid process [23], using silane and diborane as precursor gases [45]. The typical diameter is 7-12 nm, comprising a Si core of 3-8 nm and a native oxide of  $\sim 2$  nm. After growth we deposit the nanowires on a highly doped silicon substrate capped with a dry thermal oxide. Predeposited markers allow locating individual nanowires with an SEM and defining contacts by means of electron-beam lithography. The samples are treated with buffered hydrofluoric acid for 5 s prior to metal deposition to etch off the native SiO<sub>2</sub>. We then evaporate 60-100 nm thick Ni contacts, leaving a Si channel of typically 300 nm uncovered.

After metal lift-off the samples are annealed in sequential steps of 20-30 seconds at 380°C and 410°C, to induce radial and longitudinal diffusion of Ni into the Si nanowire. From both Ni contacts a NiSi segment is formed in the nanowires with lengths of 100-150 nm, depending on amongst others diameter, temperature and time. In Figure 5.1A a schematic of a resulting NiSi–Si–NiSi nanowire is shown. The remaining Si section is connected to the lithographically defined Ni contacts by two NiSi leads. Scanning electron micrographs reveal silicide segments as bright regions which sandwich a darker section of Si, see e.g. Figure 5.1B or [75, 76]. These devices have room-temperature resistances varying from 100 k $\Omega$  to 5 M $\Omega$ . They are cooled down to cryogenic temperatures with a pumped  $^4\text{He}$ -cryostat or a dilution refrigerator. All data in this chapter have been taken at base temperature of 20 mK. Some nanowires are fully transformed into NiSi having room temperature resistances of 1-5 k $\Omega$ , corresponding to  $\rho \sim 10 \mu\Omega\text{cm}$ , consistent with values found in NiSi nanowires [67] and large single crystals [68].

## 5.2 Small silicon quantum dots

The relatively high electron and hole effective mass in silicon, about 5-10 times higher than in InAs or GaAs, brings along a relatively small energy level spacing. As a consequence, the observation of quantum states in silicon nanowires requires short channel lengths. Electron-beam lithography can be used to define Schottky tunnel contacts with separations down to 30-50 nm. However, the minimum width of the source and drain contacts is at least ten times the nanowire diameter. In this geometry the distance to the backgate is greater than the dot length, and thus the electric field lines coming from the backgate are severely screened by the metallic leads. In a NiSi–Si–NiSi nanowire the leads and quantum dot have comparable diameters, which strongly reduces screening of the backgate compared to lithographically defined leads [75, 76]. Thus the backgate has a stronger capacitive coupling. An extra advantage is that this technique allows the formation of dots shorter than 30 nm.

Electrical characterization is carried out by measuring the current from drain to ground while sweeping the bias voltage,  $V_{SD}$ , at the source and stepping the backgate voltage,  $V_{BG}$ . The resulting differential conductance,  $dI/dV_{SD}$ , versus  $V_{SD}$  and  $V_{BG}$  shows a set of diamond-shaped regions, in which the current is zero due to Coulomb blockade [21]. A typical measurement is presented in Figure 5.1C. Inside a Coulomb diamond the number of charges,  $N$ , on the dot is fixed. The diamond edges mark the onset of a finite current when the ground state of the  $N^{\text{th}}$  hole,  $\text{GS}(N)$ , becomes available for transport and the number of holes

starts to alternate between  $N$  and  $N - 1$ . Outside the diamonds many lines run parallel to the edges, indicating a change in conductance which is caused by the availability of extra channels for transport. Note that lines ending on the  $N^{\text{th}}$  diamond are attributed to the excited states of the  $N^{\text{th}}$  hole,  $\text{ES}(N)$  [69]. The fact that excited states are visible is a direct consequence of the small size of the quantum dots and therefore large level spacing. This demonstrates that we have access to individual quantum states.

We have measured 30 Si nanowire single quantum dots on substrates with  $\text{SiO}_2$  thicknesses of 50 and 285 nm. The backgate-to-dot capacitance,  $C_{BG}$ , is derived as  $C_{BG}=e/\Delta V_{BG}$ , where  $\Delta V_{BG}$  is the voltage needed to add a single charge, see Figure 5.1C. A cylinder-on-plate model can be used to connect  $C_{BG}$  to the Si dot length,  $L$ , see e.g. [70]. However, this model does not take into account screening of the electric fields. To get around this we have applied the Poisson equation to the geometry of Figure 5.1A to compute  $C_{BG}(L)$ , yielding e.g.  $L = 28$  nm for the device in Figure 5.1B. When the channel length measured in SEM images is compared to the length determined from the model we obtain an accuracy within 30% in different devices. We conclude that the model gives a good estimate of the dot length and that the screening from contacts at NiSi–Si junctions is very small.

So far our results do not differ qualitatively from quantum dots in other systems. However, Figure 5.1D shows ten Coulomb diamonds of the device shown in Figure 5.1B, which are almost kite-shaped: the slopes of two adjacent diamonds are not parallel, in contrast to the conventional parallelograms of Figure 5.1C. This can be explained by looking at the schematic picture of the stability diagram in Figure 5.1E (slopes copied from the data in 5.1D): The electrochemical potential denotes the difference between the dot ground-state energy with  $M$  holes and  $M - 1$  holes,  $\mu(M) = U(M) - U(M - 1)$ . In other words, it corresponds to the transition between  $\text{GS}(M)$  and  $\text{GS}(M - 1)$ . The  $M$ -hole diamond edges are set by  $\mu(M)$  (green lines) and  $\mu(M + 1)$  (blue lines) and have slopes of  $-C_{BG}/C_S$  and  $C_{BG}/(C-C_S)$ , see ref [69]. Here  $C=C_S+C_D+C_{BG}$  is the sum of all capacitances to the dot and  $C_S$  ( $C_D$ ) is the capacitance between dot and source (drain). We assume that no other gates have a significant capacitive coupling to the dot. Within this model a difference in slopes for two successive transitions is the result of different capacitances to the consecutive orbitals. The slopes we observe for excited states are consistent with this picture: the dotted blue line is the electrochemical potential of the transition from  $\text{ES}(M)$  to  $\text{GS}(M + 1)$ , where the additional transport channel is formed by a higher orbital. Since the same orbital is used for transport at the next ground state transition it has the same capacitive coupling to source, drain and gate. In the stability diagram of figure

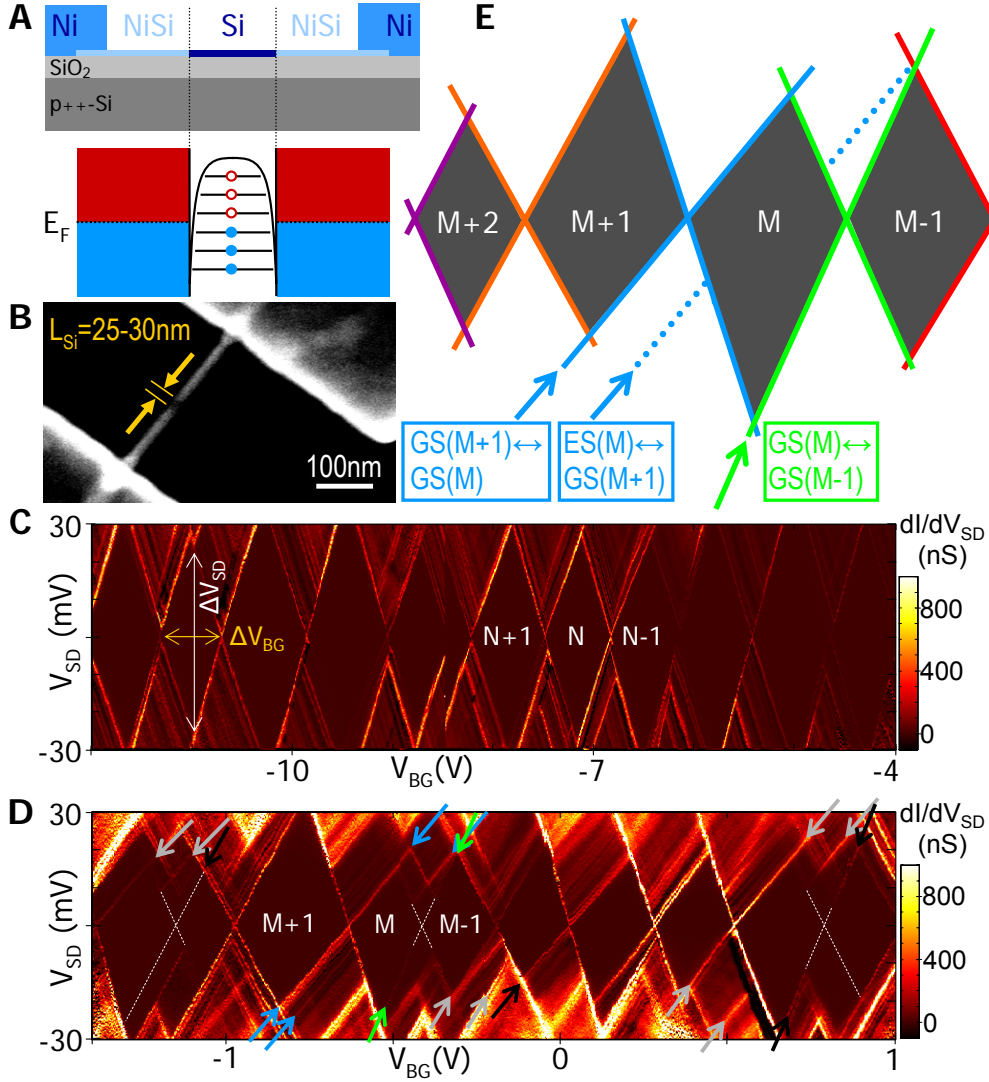


**Figure 5.1: Small silicon quantum dots.** (A) Schematic of a Si nanowire quantum dot with NiSi leads on an oxidized Si substrate. Lower panel shows a diagram of the corresponding Schottky tunnel barriers that define the quantum dot. Occupied (empty) hole states are indicated in red (blue). (B) SEM of an actual device, where the NiSi is much brighter than the Si. (C) Typical stability diagram, showing  $dI/dV_{SD}$  in color scale versus  $V_{SD}$  and  $V_{BG}$ , revealing eleven Coulomb diamonds and a charge switch at  $V_{BG} = -8.5\text{ V}$ . (D) Stability diagram of the device in (B) with kite-shaped diamonds. White dotted lines are guides to the eye to indicate the diamond edge (see additional material). Grey and blue arrows indicate six pairs of excited-state lines parallel to the ground state line of the next hole, with a slope different from the adjacent hole ground state line (black and green arrows). (E) Schematic of four diamonds from (D). The  $GS(M) \leftrightarrow GS(M-1)$  transition (green line) is not parallel to the  $GS(M+1) \leftrightarrow GS(M)$  transition and the  $ES(M) \leftrightarrow GS(M+1)$  transition (blue lines).

5.1D we can find six pairs of excited-state lines parallel to the ground state line of the next hole (grey arrows), with a slope different from the adjacent hole ground state line (black arrows). We note that close inspection of the  $(N + 3)$ -diamond in Figure 5.1C reveals that it is also kite-shaped. In short, the kites observed in Figure 5.1D can be explained by different capacitances to different orbitals in the quantum dot.

Now we discuss the physical origin of the kites. As stated before, the variation in diamond slopes implies that at least one capacitance changes for different orbital occupation. Combining the above equations with the measured slopes gives source and drain capacitances between 1.7 and 2.2 aF for Figure 5.1C. In Figure 5.1D the spread is much wider and values vary from 2 to 9 aF. In a quantum dot the specific shape of the orbital wave function determines its capacitive coupling to a metallic gate. We expect  $C_{BG}$  to be roughly the same for different orbitals, because the backgate is relatively far away. On the other hand, since the source and drain are extremely close to the quantum dot and the shape of the wave function changes with each orbital,  $C_S$  and  $C_D$  can vary strongly. We remark that the kites cannot be explained by multiple-dot behavior [77] since all diamonds neatly close (clearly visible on a logarithmic scale, see additional material).

As far as we know kites have not been reported in any other material system. Based on that we suggest that the origin may lie in the degeneracy of the top of the valence band of Si, absent in e.g. GaAs 2DEGs and InAs nanowires. If a quantum dot is alternately filled by heavy and light holes which have different types of orbitals, the coupling of the wave functions to the leads can differ for consecutive hole numbers. This can induce strong variations in capacitive coupling of successive orbitals and thus kites as we have observed. However, it does not identify *what* determines whether a stability diagram will consist of mainly parallelograms or kites, as in Figures 5.1C and 5.1D.

In these small diameter nanowires the degeneracy of the heavy hole and light hole subbands can be lifted by confinement, see e.g. calculations based on density functional theory [78, 79] and tight-binding models [40, 41]. If so, an empty Si nanowire quantum dot will start to fill with holes of the highest subband, resulting in a regular diamond pattern as in Figure 5.1C. At higher charge numbers holes of the second subband, with a different effective hole mass, can also enter the dot and cause different slopes of adjacent diamond edges as in Figure 5.1D. The latter device contains about 23–32 holes, whereas the first has about 3–13 holes, see additional material. The higher hole number can thus cause the kites. Another explanation is the absence of subband splitting due to weaker confinement in the nanowire of Figure 5.1D, e.g. in the case of a bigger diameter.

The results in Figure 5.1 show that we can reproducibly fabricate Si nanowire quantum dots with sizes of 3 to 100 nm and a tuneable hole number over a large range. The observed asymmetry in Coulomb diamonds is a strong indication of the degeneracy of heavy and light hole bands in silicon.

### 5.3 Observation of the last hole

We have also fabricated devices with an additional side gate (see the inset of Figure 5.2A). The side gate allows for more tunability – it is about 40 nm away from the nanowire and the distance between the lithographically defined Ni contacts is 250 nm. Based on the backgate capacitance at high hole numbers we estimate the Si dot length to be about 12 nm, becoming even smaller as holes leave the dot. The nanowire broke after the measurements.

In the main panel of Figure 5.2A we plot the current versus  $V_{BG}$  and side gate voltage,  $V_{SG}$ , at a bias of 2 mV. Each time a hole is added to the quantum dot, a current peak appears as a diagonal line, a typical signature of a single quantum dot [80]. The slopes give roughly  $C_{SG}=1.3C_{BG}$ , with  $C_{BG} \sim 0.07aF$ , based on diamond 10 in Figure 5.2B. The peak of the last hole is about 5 pA high and as a result barely visible in this color scale.

The shape of the confinement potential is modified differently by  $V_{BG}$  and  $V_{SG}$  because of their global (backgate) and more local electric field (side gate). As a result the potential well is not a perfect parabola as sketched in Figure 5.1A, but its width at a fixed height can vary in gate space. Therefore the diagonal Coulomb peak lines are slightly curved instead of perfectly parallel. The bending of two adjacent peaks towards or away from each other means that the addition energy changes. This is also reflected in the stability diagrams of Figure 5.2B, taken versus  $V_{BG}$  (upper panel) and  $V_{SG}$  (lower panel), where diamonds of the same hole number have different sizes. Some peaks become switchy over a certain gate range, e.g. the bistable behavior for values of  $V_{BG}$  between -18 and -10 V in Figure 5.2A.

In Figure 5.2C we see many similarities in the stability diagrams versus side gate (left panel) and backgate voltage (right panel): The addition energy of in the  $N = 1$  diamond is 114 meV, the first excited state lies about 80 meV above the ground state and is more pronounced at positive than at negative  $V_{SD}$ . This is a result of asymmetric tunnel barriers and will be explained later. The excited state line of the second hole (the singlet-triplet splitting) is about 10 meV above the ground state line and it does not run parallel to  $\mu(1)$  but to  $\mu(2)$ . This confirms our previous observation in Figure 5.1D and E and underlines the

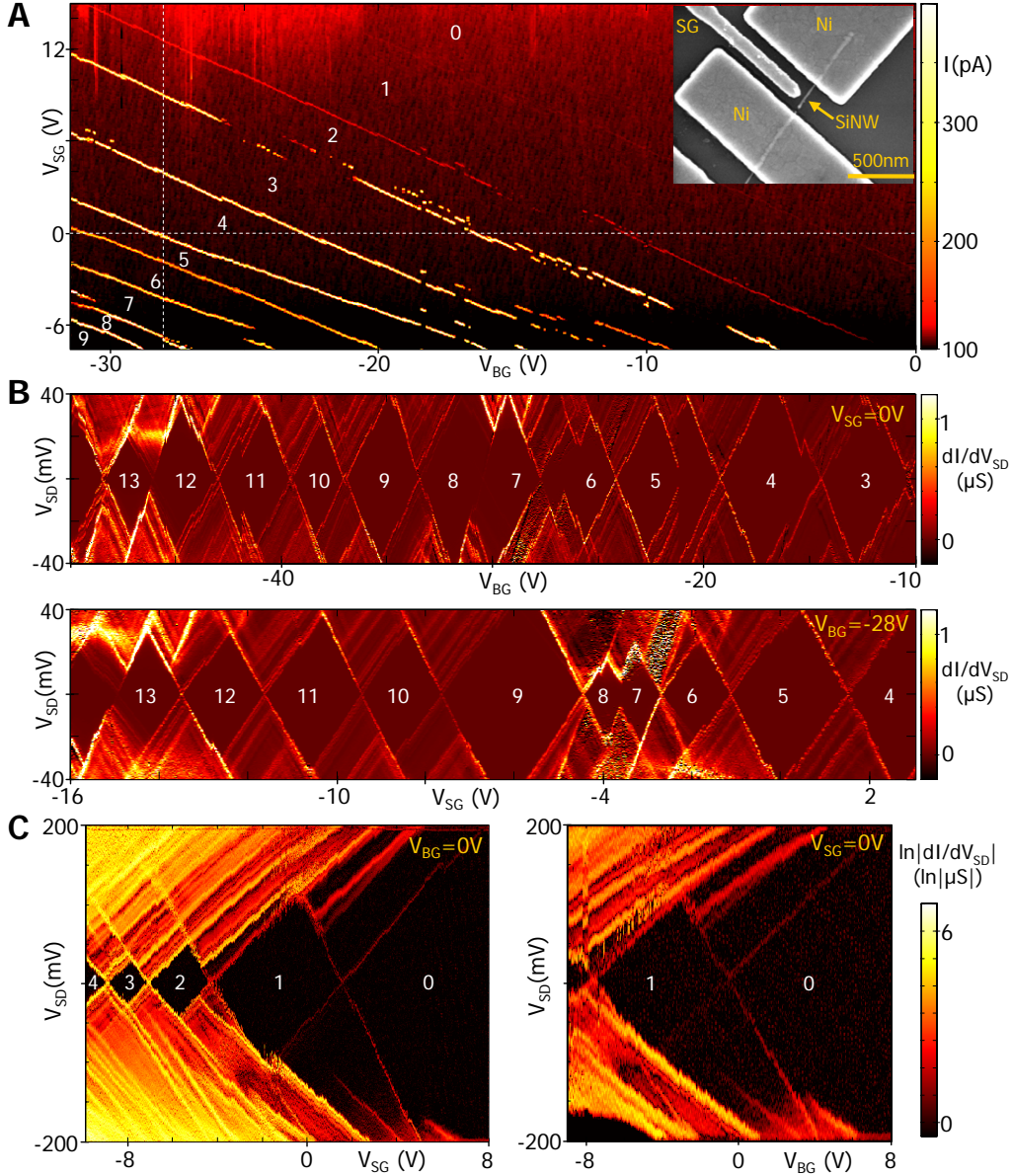


**Figure 5.2: Observation of the last hole.** (A) Current in color scale versus side gate voltage  $V_{SG}$  and  $V_{BG}$  at a bias of 2 mV. Diagonal lines correspond to transitions from  $N$  to  $N + 1$  holes, indicated in white digits. White dashed lines refer to the diagrams in (B). Inset: SEM of the device with two Ni contacts and a SiO<sub>2</sub>/Cr/Au side gate. (B) Stability diagrams of the same device with the backgate (upper panel,  $V_{SG}=0$  V) and the side gate (lower panel,  $V_{BG}=-28$  V). Diamonds of the same hole number have different addition energies for side gate and backgate sweeps, consistent with the bending Coulomb peak lines in (A). (C) Either gate can be used to control the number of holes down to zero. In both cases the last diamond opens completely, a strong indication that we have pushed out the last hole.

impact of different capacitive couplings of consecutive orbitals to the leads. The voltage on the source deforms the confinement potential as well as the Schottky barriers, which leads to bending of the ground and excited state lines outside the diamonds. This may account for the unexpected feature right of the last diamond at negative bias. The last diamond opens completely up to  $\pm 200$  mV bias. We have measured no current up to  $V_{BG}=50$  V, which means that the last diamond does not close and we have indeed observed the last hole. In Figure 5.3 we will provide extra proof. The results in Figure 5.2 demonstrate a high degree of tunability, allowing for control of the number of holes on this quantum dot down to the last one with both the side gate and the backgate.

## 5.4 Zeeman energy of the first four holes

Now we zoom in on the  $N = 0 \leftrightarrow 1$  and the  $N = 1 \leftrightarrow 2$  transition at  $B = 0, 1, 2, 4$  and  $8$  T (Figure 5.3A) applied perpendicular to the substrate. Both transitions exhibit a set of excited states parallel to the GS(1) and GS(2) lines. They cannot be attributed to electronic states, since those are both higher in energy than  $10$  meV, see 5.2C. The origin of the additional lines is not yet fully understood, but we have indications that they correspond to phonon-assisted tunneling, see next chapter. In this work we focus on the Zeeman splitting  $E_Z = |g|\mu_B B$ , where  $\mu_B = 58 \mu\text{eV/T}$  is the Bohr magneton. A finite magnetic field lifts the ground-state spin degeneracy, and splits it in a spin-up and spin-down line separated by  $E_Z$ .

In our measurements the Zeeman-split spin state (indicated by blue arrows) can be distinguished from the other excited states because (i) it has a higher differential conductance and (ii) it moves away from the ground state when the magnetic field is increased. In Figure 5.3B we show the Zeeman splitting extracted from measurements as in Figure 5.3A at magnetic fields up to  $9$  T. Linear fits yield measured g-factors of  $|g| = 2.27 \pm 0.18$  for  $N = 0 \leftrightarrow N = 1$  and  $|g| = 2.26 \pm 0.23$  for  $N = 1 \leftrightarrow N = 2$ .

At the  $N = 0 \leftrightarrow 1$  transition the Zeeman-split spin-up state,  $|\uparrow\rangle$ , appears only at positive  $V_{SD}$  as a result of asymmetric source and drain tunnel barriers: when the electrochemical potential for the  $N = 0$  to  $|\downarrow\rangle$  transition,  $\mu_{0\leftrightarrow\downarrow}$ , becomes available for transport, only a spin-down hole can tunnel through the dot. Upon increasing the bias window the  $N = 0$  to  $|\uparrow\rangle$  transition,  $\mu_{0\leftrightarrow\uparrow}$ , enters the bias window as well and raises the tunnel rate onto the dot from  $\Gamma_{\downarrow}^{\text{in}}$  to  $\Gamma_{\uparrow}^{\text{in}} + \Gamma_{\downarrow}^{\text{in}}$  because a hole with either spin-up or spin-down can enter. This is shown schematically in the energy level diagrams of the dot in the upper left panel of Figure 5.3C. The tunnel rate to leave the dot  $\Gamma^{\text{out}}$  does not change since only one hole can tunnel

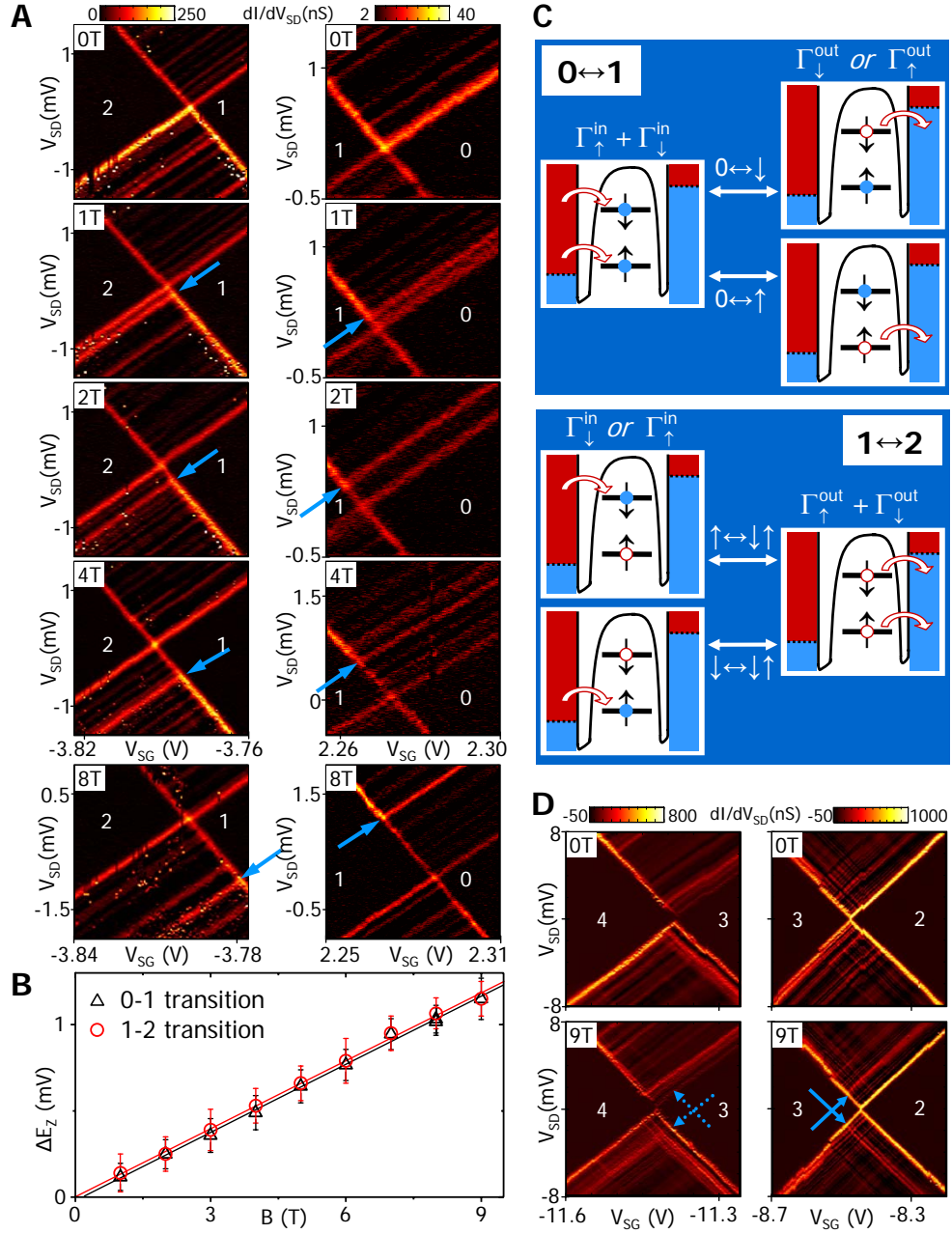


**Figure 5.3: Zeeman energy of the first four holes.** (A) Zoom on the  $0 \leftrightarrow 1$  and the  $1 \leftrightarrow 2$  transition at  $B = 0, 1, 2, 4$  and  $8$  T. At the  $0 \leftrightarrow 1$  ( $1 \leftrightarrow 2$ ) transition the Zeeman line appears at positive (negative) bias and moves away from the ground state line with  $|g|\mu_B B$  (blue arrows). (B) Zeeman energy versus magnetic field for both transitions. Red and black lines are linear fits. (C) Energy level diagrams explaining the influence of asymmetric barriers when the Zeeman split state is added to the bias window. At the  $0 \leftrightarrow 1$  ( $1 \leftrightarrow 2$ ) transition there is only an observable increase in conductance if the holes tunnel in (out) through the barrier with the lowest tunnel rate. (D) Zooms on the  $2 \leftrightarrow 3$  and the  $3 \leftrightarrow 4$  transitions at  $0$  and  $9$  T.

off (upper right panel):  $\Gamma^{\text{out}} = \Gamma_{\uparrow}^{\text{out}}$  or  $\Gamma_{\downarrow}^{\text{out}}$ , depending on which spin entered the dot previously (assuming no spin relaxation). This means that the addition of an extra level in the bias window only increases the conductance noticeably if the holes tunnel into the dot via the barrier with the lowest tunnel rate, see Figure 5.3C. In our Si dot the source barrier has the lowest tunnel rate. Therefore in the  $0 \leftrightarrow 1$  transition the Zeeman splitting only becomes visible at positive bias [81].

The situation is reversed at the  $N = 1 \leftrightarrow 2$  transition, where the ( $N = 2$ )-diamond edge splits at negative bias. In contrast to the edges of the ( $N = 0$ ) and ( $N = 2$ )-diamonds, the ( $N = 1$ )-diamond edges do not show Zeeman splitting. This means that in the 2-hole ground-state both holes are in the lowest orbital with opposite spins [82, 83]. Assuming the g-factor is positive as in bulk Si the first hole ground-state is spin-down,  $|\downarrow\rangle$ . When the second hole is added to the lowest orbital it is spin-up,  $|\uparrow\rangle$ . In the transport cycle of this transition  $\Gamma^{\text{in}}$  does not change when an additional level enters the bias window, since only one spin species can enter the dot (lower left panel of Figure 5.3C). After this event the dot state can change to either  $|\downarrow\rangle$  or  $|\uparrow\rangle$  when respectively a spin-up hole or a spin-down hole leaves the dot. Since both spin species can tunnel off  $\Gamma_{\text{out}}$  increases to  $\Gamma_{\uparrow}^{\text{out}} + \Gamma_{\downarrow}^{\text{out}}$  when the second level becomes available for transport. This is reflected by the Zeeman split line at negative bias, where holes tunnel off via the barrier with the lowest tunnel rate, the source.

At the  $N = 2 \leftrightarrow 3$  and the  $N = 3 \leftrightarrow 4$  transitions the tunnel barriers become less opaque and more symmetric. This makes it harder to distinguish the Zeeman spin states from the other excited states. The zooms in Figure 5.3D at 0 and 9 T, give a strong indication of Zeeman splitting of the ( $N = 2$ )- and ( $N = 4$ )-diamond edges, corresponding to  $|g| = 2.3 \pm 0.7$  in both cases. From the splitting of even- $N$  diamond edges we deduce that the third and fourth hole are respectively spin-down and spin-up.

The results in Figure 5.3 show excited-state spectroscopy of the Zeeman energy of hole 1 to 4, from which we deduce a g-factor of  $\sim 2.3$  and spin filling with alternating spin-down and spin-up. This is the first experimental observation of Zeeman splitting in a few-hole Si quantum dot. The clarity of our data allow for a complete understanding of the spin states of the first four holes.

## 5.5 Magnetospectroscopy of the first four holes

We have also performed magnetospectroscopy on the first four holes to deduce the spin filling of the quantum dot. Figure 5.4A shows the current versus side gate voltage, where the number of holes goes from four to zero. The  $0 \leftrightarrow 1$

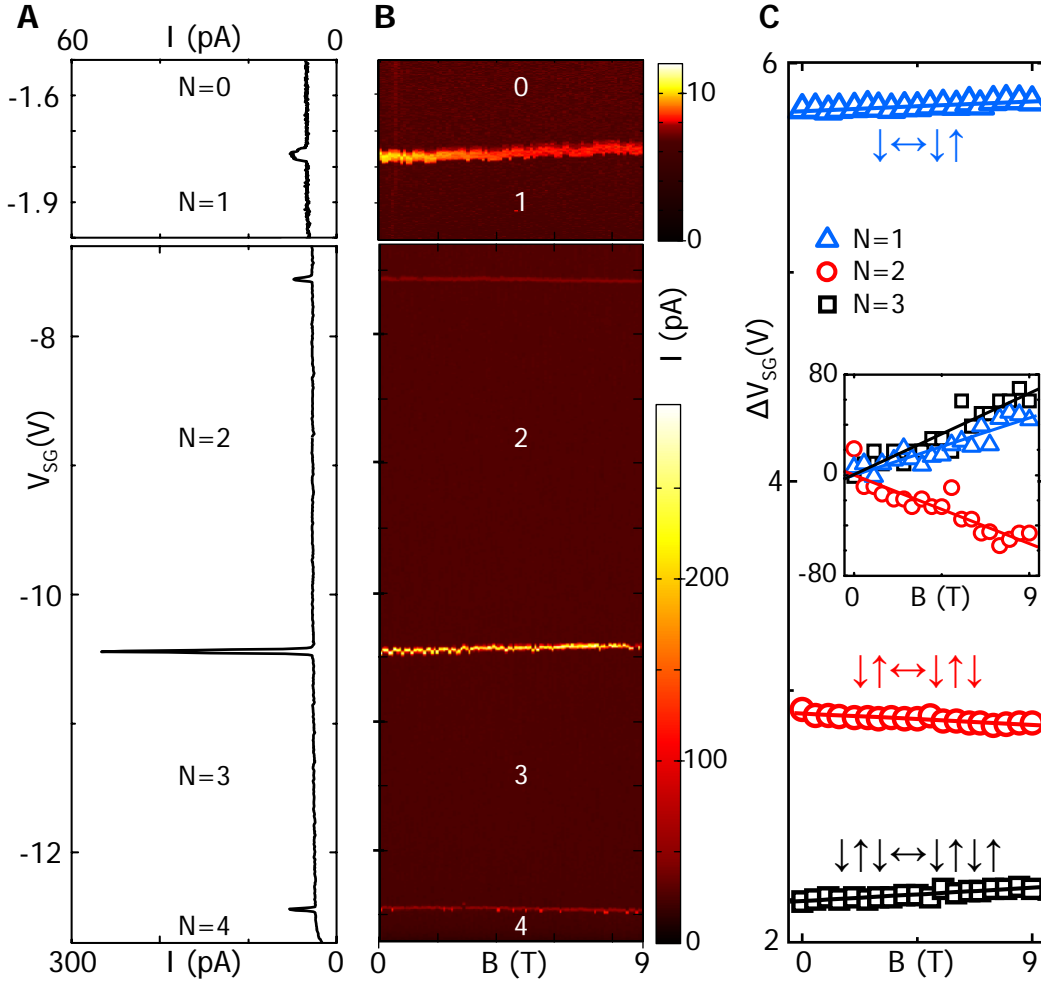


**Figure 5.4: Magnetospectroscopy of the first four holes.** (A) Coulomb peaks corresponding to the addition of hole 1 (upper panel,  $V_{SD}=0.8$  mV) and hole 2, 3 and 4 (lower panel,  $V_{SD}=0.6$  mV). (B) Evolution of the Coulomb peaks with magnetic field. The direction alternates due to even-odd spin filling. (C) The peak-to-peak distance  $\Delta V_{SG}$  versus magnetic field and linear fits for 1, 2 and 3 holes. In the inset the offset has been subtracted. Conversion of the fitted slope values to the Zeeman energy via the gate coupling factor,  $\alpha$ , gives corresponding g-factors of  $1.72 \pm 0.29$ ,  $1.77 \pm 0.43$  and  $2.02 \pm 0.58$ .

peak (upper panel) is about 2 pA at a bias of  $V_{SD}=0.8$  mV, whereas the peaks in the lower panel are taken at  $V_{SD}=0.6$  mV. Stepping the magnetic field from 0 to 9 T while sweeping the side gate voltage gives the evolution of the peak positions in Figure 5.4B. The current peaks move towards or away from each other, depending on the spin direction of the additional hole. The change in side gate voltage is small compared to the total peak-to-peak distance, but it is nevertheless observable.

This is made clear in Figure 5.4C, where we plot the distance  $\Delta V_{SG}$  between consecutive peaks for 1, 2 and 3 holes. In the inset  $\Delta V_{SG}$  is plotted without the offset. Linear fits through the data points have slopes of  $5.05 \pm 0.56$  mV/T for  $N = 1$ ,  $-6.05 \pm 0.74$  mV/T for  $N = 2$  and  $7.17 \pm 0.69$  mV/T for  $N = 3$ . The gate coupling factor  $\alpha$  converts the change in gate voltage to the Zeeman energy as  $|g|\mu_B B = \alpha \Delta V_{SG}$ . Analysis of Figure 5.2C gives  $\alpha$ -factors of  $0.020 \pm 0.001$ ,  $0.017 \pm 0.002$  and  $0.016 \pm 0.003$  for respectively  $N = 1$ ,  $N = 2$  and  $N = 3$ . Combining these values with the fitted slopes yields  $g$ -factors of  $1.72 \pm 0.29$ ,  $1.77 \pm 0.43$  and  $2.02 \pm 0.58$ . The deviation from the numbers found in Figure 5.3 is caused by the uncommon diamond shapes. They are not parallelograms just as in Figure 5.1D, which makes conversion to energy with the strict definition of  $\alpha$  as  $\Delta V_{SD}/2\Delta V_{BG}$  deviate as well. The alternating direction of the Coulomb peak evolution indicates that spin-up and spin-down holes alternately enter the dot. We have observed the same even-odd spin filling for hole numbers up to  $N = 14$  (not shown here), as has been reported previously [45].

In conclusion, we report on a consistent set of data on many small quantum dots in silicon nanowires. We argue that the asymmetry in Coulomb diamonds is caused by the degeneracy of heavy and light hole bands. A detailed investigation of a few-hole quantum dot reveals the first observation of the Zeeman energy of a single spin in silicon. The magnetic field dependence of the Zeeman energy for the  $0 \leftrightarrow 1$  and  $1 \leftrightarrow 2$  hole transition yields a  $g$ -factor close to the Si bulk value. We have observed spin transitions corresponding to even-odd filling through both excited-state spectroscopy and magnetospectroscopy. The isolation and identification of a single spin in silicon is an important step on the route towards the realization of solid state spin qubits in silicon. In order to perform quantum operations, a double quantum dot scheme with tuneable tunnel barriers is required, e.g. by means of local gates. Such gates demand a resolution in lithographic techniques of  $\sim 10$  nm, due to short channel length of these Si quantum dots (10-30 nm). If that requirement is met, the coherent manipulation of single spins in Si nanowire quantum dots should be well within reach.

We thank T. Balder, R. Hanson, A. A. van Loon, K. C. Nowack, R. N. Schouten, G.A. Steele and I. T. Vink for help and discussions.

## 5.6 Additional material

### Differences between devices

The three most obvious differences between these two devices in Figures 5.1C and 5.1D are hole number, dot length and tunnel coupling:

(i) The exact hole number in both devices is unknown because the diamonds no longer close before reaching the last hole. This is likely due to roughness in the bottom of the confining potential, which can split the single dot into a double dot. Therefore we estimate the number of charges by counting up holes from zero, starting at the backgate voltage at which the dot is emptied at a high bias (100 mV). We combine this so-called pinch-off voltage of  $V_{BG}=-1.3$  V with  $C_{BG}=0.2$  aF to estimate the number of charges in Figure 5.1C to change from 3 to 13. Analogously,  $C_{BG}=0.7$  aF and high-bias pinch-off at  $V_{BG}=9$  V indicate that the hole number in 5.1D runs from about 23 to 32.

(ii) The estimates for the dot lengths are 23 nm for Figure 5.1C and 28 nm for Figure 5.1D. Note that  $C_{BG}$  is about 0.2 aF in 5.1C and 0.7 aF in 5.1D, a consequence of backgate distances of respectively 285 nm and 50 nm.

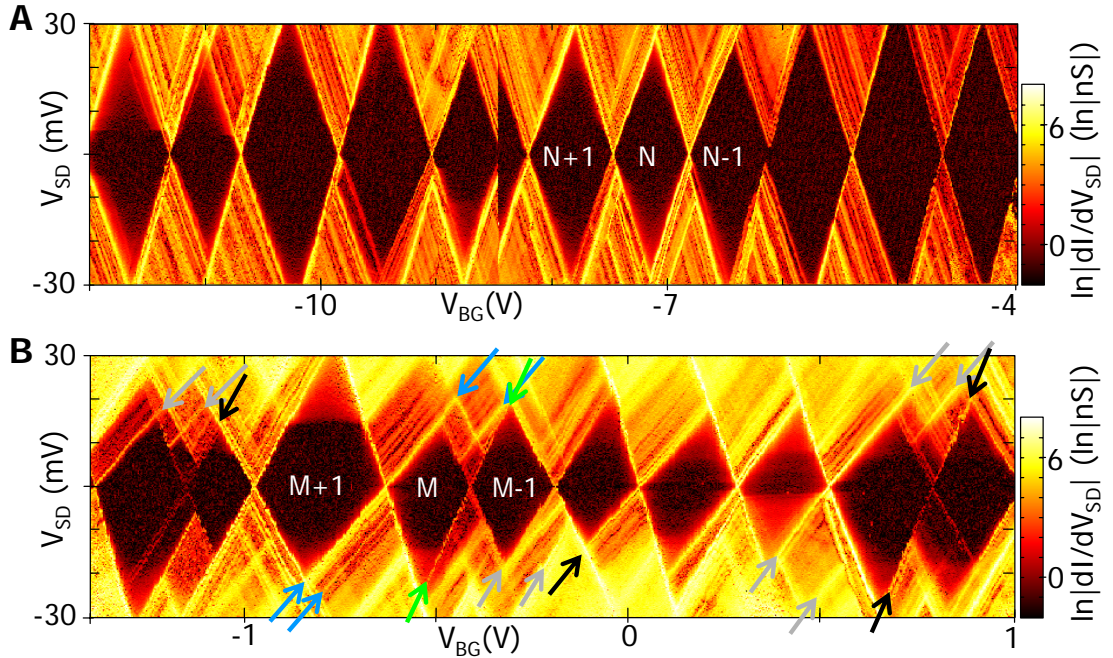


**Figure 5.5: Logarithmic plots.** (A) and (B) show the data of Figure 5.1C and 5.1D on a logarithmic scale. Cotunneling processes appear in red, e.g. in the two leftmost diamonds in (A), and in almost all diamonds in (B). Also, these plots make clear that all diamonds close, as a result of single-dot behavior.

(iii) The conductance outside the diamonds is higher in 5.1D than in 5.1C, as a result of stronger tunnel coupling. This is confirmed by the onset of cotunneling inside most kites in 5.1D, see Figure 5.5, and its absence in most diamonds in 5.1C. The larger tunnel coupling is likely due to thinner Schottky barriers at higher holer numbers. A stronger overlap of the wave function with the leads naturally corresponds to a larger capacitance to source and drain.

### Zeeman energy in a few-hole Si nanowire quantum dot

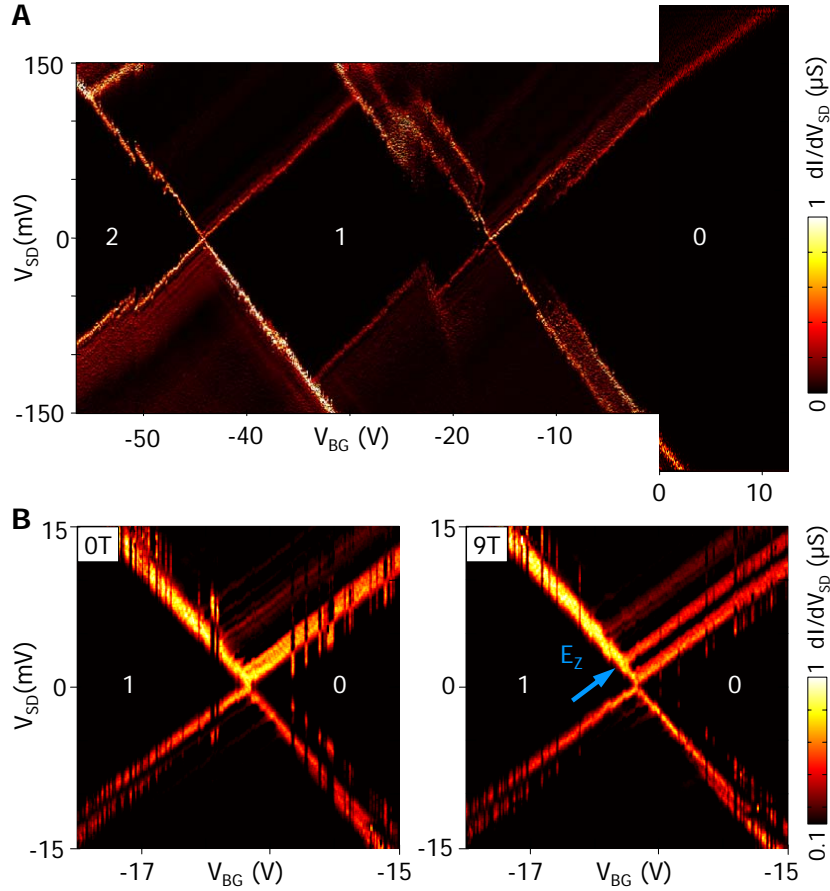


**Figure 5.6: Zeeman energy in a few-hole Si nanowire quantum dot.** (a) Stability diagram of a single-hole silicon nanowire quantum dot in another device. Here we need 30 V on the backgate to go from one to two holes as a result of a very small capacitance to the dot. The excited state of the second hole is about 120 meV. The small capacitive coupling and the large level splitting indicate a very small quantum dot ( $< 10$  nm). This device exhibits switching behavior at the  $0 \leftrightarrow 1$  transition, probably due to bistable potential fluctuations caused by a charge in the environment of the dot. (b) Zoom of the  $0 \leftrightarrow 1$  transition at 0 and 9 T, revealing the Zeeman splitting at positive bias, cf. Figure 5.3a.



# Chapter 6

## Quantized energy emission in a few-hole Si nanowire quantum dot

Many electronic transport measurements on few-electron quantum dots show transitions corresponding to additional energy levels below the  $N = 0$  ground-state energy. No one has been able to give a satisfying explanation so far. Our data on a single-hole silicon nanowire quantum dot show many discrete energy levels at different magnetic fields, allowing for a detailed analysis. The levels are quantized in multiples of 100-180  $\mu\text{eV}$  and independent of magnetic field. They can neither correspond to electronic or Zeeman states of the quantum dot itself, nor to density of states modulations in the leads. Instead, we explain the discrete energy spectrum as inelastic tunneling processes, where the excess energy is emitted to quantized states in the environment of the quantum dot. We discuss different explanations for the excitations, in particular phonon emission, photon emission and a resonances in the electric circuit. The existence of additional energy levels below the  $N = 0$  ground-state energy in various material systems with different geometries underlines the universality of the phenomenon.

---

The results in this chapter will be submitted for publication.

## 6.1 Introduction

The proposal to use single spins in quantum dots as quantum bits [10] exploits an optimal combination of the spin and charge degree of freedom [69]. The potential of this spin qubit is underlined by the recent demonstration of coherent control of one [13] and two [12] spin states in quantum dots in GaAs/AlGaAs heterostructures. Most experiments have focused on quantum dots formed in III-V semiconductors; however, electron spin coherence in those materials is limited by hyperfine interactions with nuclear spins and spin-orbit coupling. Group IV materials are believed to have long spin lifetimes because of weak spin-orbit interactions and the predominance of spin-zero nuclei. This prospect has stimulated significant experimental effort to realize single-charge quantum dots in carbon nanotubes [72, 73], Si/SiGe heterostructures [65] and Si nanowires [45].

We have demonstrated the realization of a single-hole silicon nanowire quantum dot in chapter 5. An unusual feature in these measurements are transitions corresponding to additional energy levels below the  $N = 0$  ground-state energy of the dot, which cannot correspond to electronic or Zeeman states. In this paper we investigate the nature of these discrete energy levels, specifically their magnitude, spacing and magnetic field dependence. It turns out that the levels are quantized in multiples of 100-180  $\mu\text{eV}$  and independent of magnetic field. We explain the discrete energy spectrum via inelastic tunneling processes, where the excess energy is emitted to quantized states in the environment of the quantum dot. We discuss different explanations for the excitations, in particular phonon emission, photon emission and a resonant  $LC$ -line.

The additional energy levels below the  $N = 0$  ground-state energy appear in virtually all electronic transport measurements on one-electron quantum dots, see e.g. the energy level spectra of single charges in vertical InGaAs quantum dots [84, 85], lateral GaAs quantum dots [86], carbon nanotube quantum dots [72], InAs nanowire quantum dots [87, 88], and also silicon nanowire quantum dots. The existence in various material systems with different geometries underlines the universality of the phenomenon. The detailed analysis of our data on a single-hole silicon nanowire quantum dot paves the way to a better understanding of the additional discrete energy levels.

## 6.2 Discrete energy spectrum due to environment

We prepare NiSi-Si-NiSi nanowire devices with a diameter of 7-12 nm as described in Chapter 5, resulting in a Si quantum dot with metallic NiSi leads. The measurements presented in this work are performed on the device shown in

the right panel of Figure 6.1A, which has a dot length of about 12 nm and NiSi leads of  $\sim 120$  nm. The side gate is about 40 nm away from the nanowire and

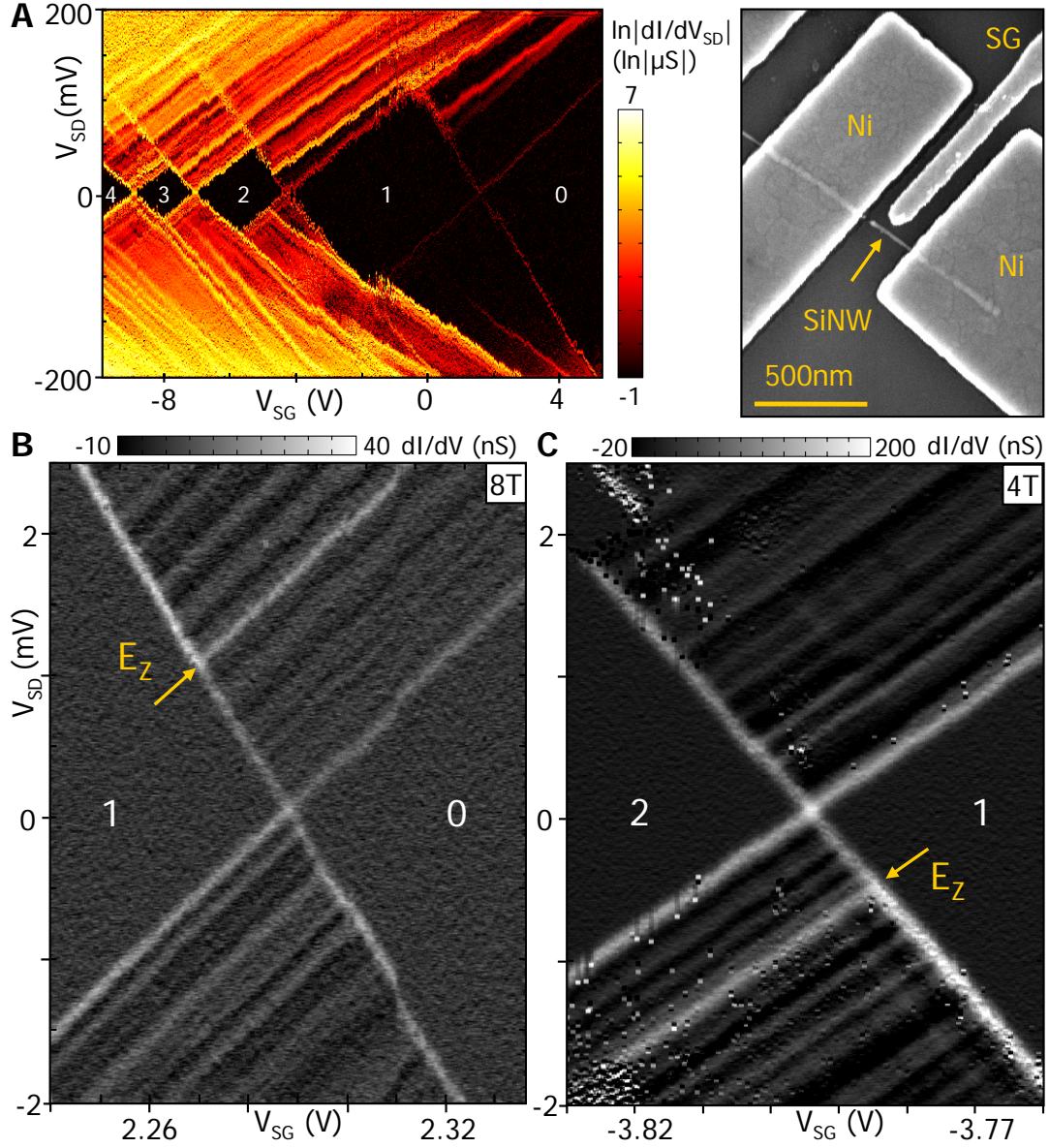


**Figure 6.1: Discrete energy spectrum due to environment.** (A) Left panel: Stability diagram of the last four holes, showing  $\ln|dI/dV_{SD}|$  in color scale versus  $V_{SD}$  and  $V_{SG}$ . The excited states in the first two diamonds are more than 10 meV above the ground state energy. Right panel: SEM of the device with two Ni contacts and a side gate. (B) Zoom on the  $0 \leftrightarrow 1$  transition at  $B = 8$  T, showing many lines of increased conductance at discrete energies ending on both the  $N = 0$  and  $N = 1$  region. The brightest of these lines can be attributed to the Zeeman energy. (C) Zoom on the  $1 \leftrightarrow 2$  transition at  $B = 4$  T, showing the same features as (B).

the distance between the lithographically defined Ni contacts is 250 nm. The left panel of Figure 6.1A shows the differential conductance,  $dI/dV_{SD}$ , versus the source-drain voltage,  $V_{SD}$ , and the side gate voltage,  $V_{SG}$ , measured at zero magnetic field. Inside the diamond-shaped regions, the current is zero due to Coulomb blockade [21] and the number of holes on the dot is fixed. We can control of the number of charges down to a single hole in the dot, as explained in Chapter 5. The line of increased conductance ending on the  $N = 1$  diamond edge is attributed to the excited orbital state of the first hole, which is about 80 meV above the ground state. Analogously we observe that the excited state of the second hole is about 10 meV above the ground state energy. Measurements on other devices show a comparable discrete energy level spectrum.

In Figure 6.1B we zoom in on the transition from 0 to 1 holes at a magnetic field of 8 T applied perpendicular to the substrate. The diamond edges mark the onset of a finite current when the electrochemical potential of the transition between GS(0) and GS(1) enters the bias window. Many lines of increased conductance end on both the  $N = 1$  and  $N = 0$  diamond edge. The brightest line is 1.02 meV above the ground state line, which corresponds to the Zeeman energy at 8 T. We followed this line versus magnetic field, see Chapter 5. At negative bias voltages the Zeeman-split excited state is not visible because it does not give a significant contribution to the current due to asymmetric tunnel barriers, see Chapter 5. The other lines of increased conductance cannot be attributed to the level spacing or the Zeeman splitting of the Si quantum dot. Firstly because the energies of the corresponding transitions are very small, spaced by roughly 100-150  $\mu\text{eV}$ . More important, the lines ending on the  $N = 0$  diamond edge would involve transitions using states below the  $N = 0$  ground state. Such a transition can only be an electronic state of quantum dot if it is an excited state of the first electron, which is 1.17 eV in energy away from the zero hole ground state. From this we conclude that the additional lines do *not* originate from an intrinsic property of the Si quantum dot itself, but are necessarily due to interactions with the (local) environment. The zoom of the transition from 1 to 2 holes at 4 T in Figure 6.1C clearly shows the same features as the 0 to 1 transition. The only (qualitative) difference is the presence of the Zeeman energy at negative instead of positive bias voltages, as we have already explained in Chapter 5.

The results in Figure 6.1 demonstrate that the measured lines of increased conductance cannot be attributed to hole transport via higher orbital states or Zeeman-split states. Instead, the origin lies in something in the environment of the quantum dot that results in lines of increased conductance above and under the ground state transition. We first investigate the properties of these lines before we try to identify the nature of the environment that causes them.

## 6.3 Quantized energy spectrum for different bias directions

We start out by verifying whether the magnitude and spacing of the lines depend on the bias direction. We measure the current versus  $V_{SD}$  and  $V_{SG}$  at the  $N = 1 \leftrightarrow 2$  transition at 0 T (Figure 6.2A). The corresponding differential conductance in Figure 6.2B displays a similar line pattern as we have seen at the  $N = 0 \leftrightarrow 1$  transition. Figure 6.2C shows two IV-characteristics taken from Figure 6.2A in which the current makes a step of about 10-20 pA when the ground-state enters the bias window. After that, current peaks of 1-5 pA appear which look equally spaced in energy. The lower increase in current of the latter is a direct result of lower tunnel coupling.

Now we look in more detail at the energies,  $E_n$ , of the lines, to which we have assigned a number  $n$  as shown in Figure 6.2A. Since the lines are roughly equidistant, we have leave out  $n = 2$  and  $n = 6$  at negative bias, and  $n = 8$  at positive bias. The difference in energy between the  $n^{\text{th}}$  line and the ground state transport line,  $E_n - E_0$ , is plotted as a function of  $n$  in Figure 6.2C (For  $E_n$  we take the center of each line). The linear fits through the data points have slopes of  $126.0 \pm 2.0 \mu\text{eV}$  and  $-126.1 \pm 3.7 \mu\text{eV}$  for respectively positive and negative bias voltages. Both the fact that all points fit a straight line with little error and the symmetry in bias strongly suggests that the energies involved in these transitions are equidistant. This indicates something in the environment that is either determined by a harmonic oscillator potential or has a bosonic nature. The unobservable lines are probably washed out by modulations of the ground-state resonant tunnel rate due to modification of the barrier while  $V_{SD}$  is increased. For example, the big dip in (negative) current at  $V_{SD} = -0.7$  mV in the green trace of Figure 6.2B masks the  $n=2$  line.

The quantitative analysis in Figure 6.2 demonstrates that the discrete energy levels are equidistant and symmetric in voltage bias. The energy spectrum is quantized in multiples of  $\Delta E = 126 \mu\text{eV}$ , even up to nine energy quanta.

## 6.4 Quantization independent of magnetic field

The second property we investigate is the evolution of the discrete energy levels with magnetic field. The Zeeman energy adds an electrochemical potential level to the quantum dot, see e.g. the bright line at positive bias in Figure 6.1B. For simplicity we look at the discrete energy level spectrum which is not parallel to the Zeeman-split excited state, so we have only one level in the dot that contributes

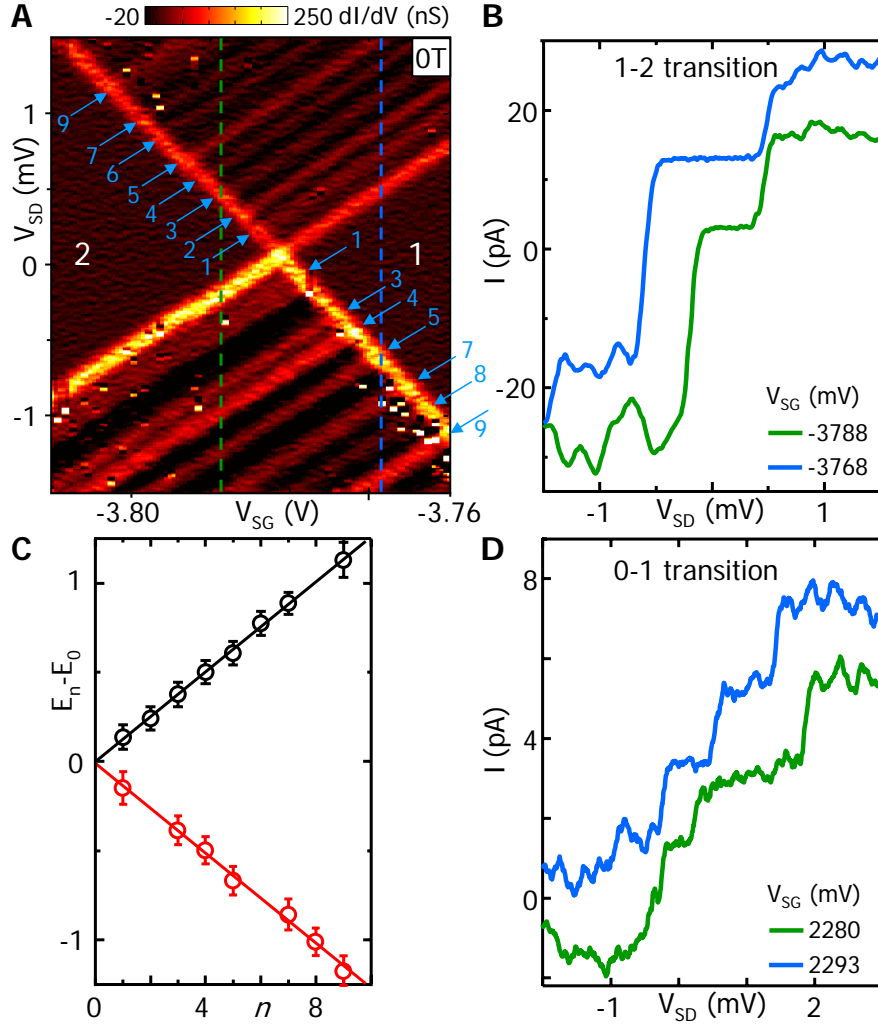


**Figure 6.2: Quantized energy spectrum for different bias directions.** (A) Differential conductance in color scale versus  $V_{SD}$  and  $V_{SG}$  at the  $N = 1 \leftrightarrow 2$  transition at 0 T displaying the same line pattern as Figure 6.1B. Blue arrows and numbers point to lines of increased conductance above the ground state transport level. (B) Current-voltage characteristics taken as line cuts from (A) at  $V_{SG} = -3788$  mV (green trace) and  $-3768$  mV (blue trace, offset by 10 pA). (C) Energy difference between the  $n^{\text{th}}$  line and the ground state energy versus  $n$  for positive bias (black circles) and negative bias (red circles). The linear fits through the data points have slopes of  $126 \mu\text{eV}$  (black trace) and  $-126 \mu\text{eV}$  (red trace). (D) Current-voltage characteristics of the  $N = 0 \leftrightarrow 1$  transition taken as line cuts from 6.1B at  $V_{SG} = 2280$  mV (green trace, offset by 2 pA) and  $2293$  mV (blue trace).

to the current. Since only the edges of even- $N$  diamonds are Zeeman-split, we look at negative (positive) bias of the  $N = 0 \leftrightarrow 1$  ( $N = 1 \leftrightarrow 2$  transition). The spectrum of both transitions has been analyzed as in Figure 6.2 at magnetic fields

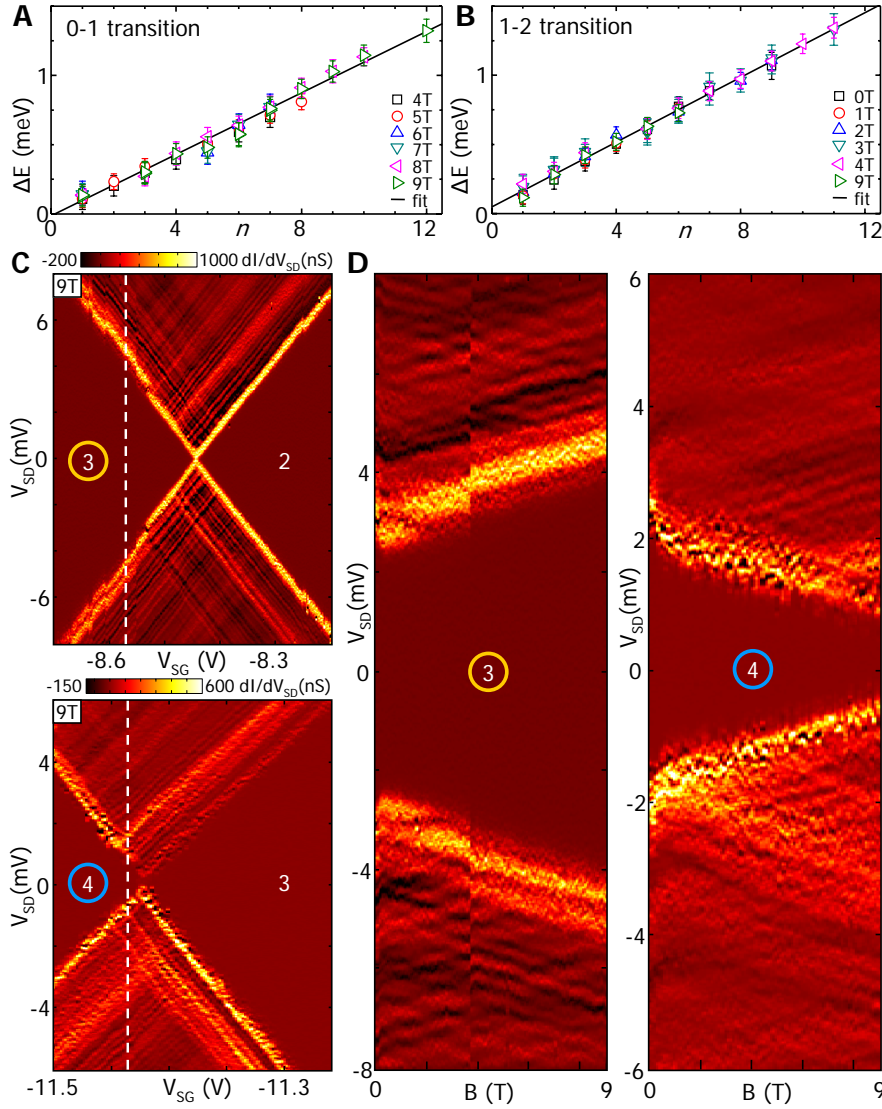


**Figure 6.3: Quantization independent of magnetic field.** (A) Energy level spectrum of the  $0 \leftrightarrow 1$  transition at  $B = 4$  to 9 T. Black trace is a linear fit with a slope of  $111 \mu\text{eV}$ . (B) Energy level spectrum of the  $1 \leftrightarrow 2$  transition at  $B = 0$  to 9 T. Black trace is a linear fit with a slope of  $117 \mu\text{eV}$ . (C) Zoom of the discrete energy level spectrum at 9 T at the  $2 \leftrightarrow 3$  (upper panel) and the  $3 \leftrightarrow 4$  transition (lower panel). (D) Magnetospectroscopy of the discrete energy levels of the  $N = 2 \leftrightarrow 3$  (left panel) and the  $N = 3 \leftrightarrow 4$  transition (right panel), taken at the line cuts indicated by white dashed lines in (C). A charge switch is visible in the left panel at  $B = 3.7$  T. The color scales of (C) are used.

ranging from 0 to 9 T and is plotted in Figure 6.3A and B. The level energies do not change with magnetic field and linear fits have slopes of  $117.0 \pm 3.4 \mu\text{eV}$  and  $110.9 \pm 4.0 \mu\text{eV}$  for respectively the  $N = 1 \leftrightarrow 2$  and the  $N = 0 \leftrightarrow 1$  transition.

We have combined energy spectroscopy with magnetospectroscopy to study the magnetic field evolution of the discrete spectrum at the  $N = 2 \leftrightarrow 3$  and the  $N = 3 \leftrightarrow 4$  transition. The upper panel of Figure 6.3C reveals a grid of lines in the zoom of the  $N = 2 \leftrightarrow 3$  transition, whereas only lines in one direction are visible at the  $N = 0 \leftrightarrow 1$  and the  $N = 1 \leftrightarrow 2$  transition in Figure 6.1. Here the lines from top left to bottom right are suppressed due to a strong asymmetry in the tunnel barriers. The  $N = 2 \leftrightarrow 3$  transition is at a side gate voltage where the barriers are more symmetric, and lines appear parallel to both diamond edges. One of the tunnel barriers becomes slightly more opaque at the gate voltage of the  $N = 3 \leftrightarrow 4$  transition, resulting in a lower differential conductance and less pronounced inelastic transport lines, see lower panel in Figure 6.3C.

Magnetospectroscopy of the energy levels is performed at side gate voltages close to both transitions, indicated by white dashed lines in Figure 6.3C. The first thing we notice is that, with increasing magnetic field, the Coulomb blocked region increases at the  $N = 2 \leftrightarrow 3$  transition (Figure 6.3D, left panel) and decreases at the  $N = 3 \leftrightarrow 4$  transition (Figure 6.3D, right panel). This is directly connected to the observed Coulomb peak evolution in Figure 5.4: the peak at the  $N = 2 \leftrightarrow 3$  transition moves away from the gate voltage at which the magnetospectroscopy is performed, whereas the peak at the  $N = 3 \leftrightarrow 4$  transition moves *towards* it. The lines above the ground state transport remain equidistant and again form a grid (red in the color scale). They neatly follow the ground state transport line at a constant distance throughout the magnetic field sweep. The energy difference between the discrete levels is about 160–188  $\mu\text{eV}$  at the  $N = 2 \leftrightarrow 3$  transition and 103–114  $\mu\text{eV}$  at the  $N = 3 \leftrightarrow 4$  transition. We note that the Zeeman splitting of the  $N = 4$  diamond is faintly visible at the  $N = 3 \leftrightarrow 4$  transition.

The evolution of the energy level spectrum with magnetic field in Figure 6.3 demonstrates that the line spacing is independent of magnetic field at the first four hole transitions.

## 6.5 Quantized energy emission to the environment

Now we will discuss the possible explanations for the quantized energy spectrum, starting by summarizing the most important properties. (i) The levels are quantized in multiples between 100 and 180  $\mu\text{eV}$ . (ii) They exist above and below the ground-state transport levels, including below the  $N = 0$  ground state. (iii) The levels are independent of magnetic field. As mentioned before, electronic states of the Si quantum dot and the Zeeman energy can be ruled out because neither

matches any of the three observed properties. To our knowledge this leaves two possible explanations, which we will address below: 1. Density of states modulations in the leads, e.g. quantized states. 2. Quantized energy emission, e.g. to a phonon cavity.

It has been suggested that density of states modulations in the leads can cause extra resonances [86, 89]. In those experiments the electron reservoirs were semiconductors, whereas here they are metallic. The NiSi leads would have to form an island in series with the Si dot, that only allows states at discrete energies. However, this interpretation can be ruled out by the following arguments. First and most important, the lines are parallel to the diamond edges and their slopes are determined by the capacitive coupling to source, drain and gate [69]. In order to explain our data, the alleged NiSi islands must have the same capacitances as the Si quantum dot, which is highly unlikely due to their different sizes and locations. In the hypothetical case of equal capacitances, the electrochemical potentials of the NiSi islands move up and down by the same amount as the levels in the Si quantum dot. The lines ending on the  $N = 0$  region correspond to the situation where the  $N = 0$  ground-state energy is in the bias window, exactly  $\Delta E$  above the drain (source) at positive (negative) bias voltage, comparable to the situation in the right two panels of Figure 6.4. The NiSi islands can have available states below the  $N = 0$  ground-state energy of the Si dot, but higher-order tunneling processes would be required to explain transport from those NiSi states up to the lowest electrochemical potential level of the Si dot. Furthermore, based on  $\sim 120$  nm long NiSi cylinders with a diameter of  $\sim 10$  nm and a Fermi energy of 14 eV [90], we can expect a mean level spacing of  $\sim 8$   $\mu\text{eV}$  [91], which is more than an order of magnitude smaller than measured. Besides that, its resistance would have to be larger than the resistance quantum  $h/e^2$  in order to see single hole charging effects [92]. Based on a resistivity of 10  $\mu\Omega\text{cm}$  [67] the NiSi cylinder will have a resistance of about 150  $\Omega$ , two orders of magnitude smaller than required. Last, since NiSi is a non-magnetic material it should show Zeeman splitting, in contrast to the results in Figure 6.3.

A more likely origin of the energy spectrum are inelastic tunneling processes via discrete energy levels above and under the ground-state transition. The excess energy is absorbed to the environment of the quantum dot in quanta. In this scenario, additional tunneling processes exist where packets of energy,  $\Delta E$ , are emitted to the environment of the dot as illustrated in the diagrams in Figure 6.4. The middle panel sketches the measured non-zero differential conductance of Figure 6.1B. The adjacent electrochemical potential diagrams show the possible tunnel processes when the level of the GS(0) to GS(1) transition is in the bias window. Black arrows correspond to ground-state transport via elastic tunneling.

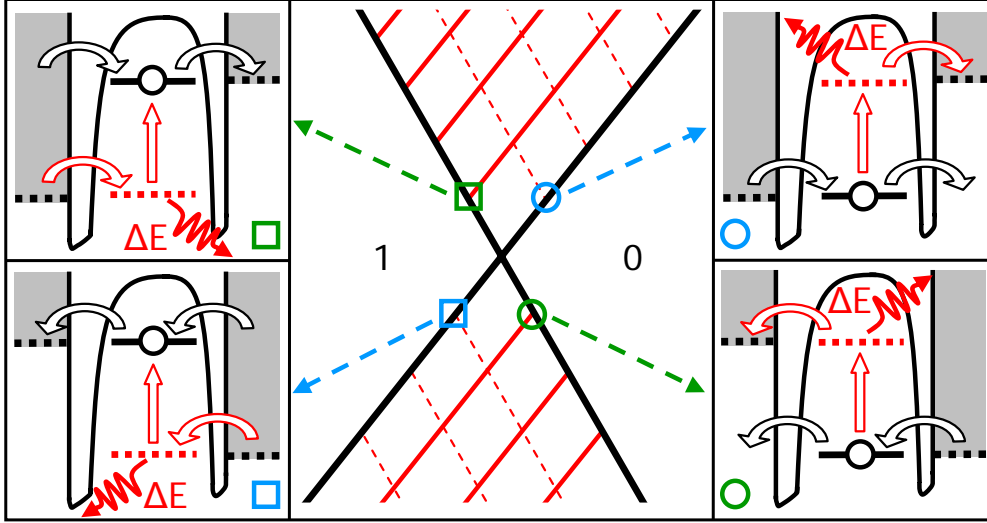


**Figure 6.4: Quantized energy emission to the environment.** The middle panel sketches the measured non-zero differential conductance of Figure 6.1B in straight lines; dashed lines are present but do not contribute significantly to the current. The adjacent diagrams show the possible tunnel processes when the ground-state transport level is aligned to source (blue symbols) or drain (green symbols). Black (red) arrows correspond to tunneling processes without (with) energy emission  $\Delta E$ . The tunnel rate into (out of) the dot increases for lines ending on the  $N = 1$  ( $N = 0$ ) region. Due to an asymmetry in tunnel barriers the inelastic tunnel processes only enhance the conductance if the holes tunnel inelastically in (out) through the barrier with the lowest tunnel rate.

In the leftmost panels red arrows indicate additional inelastic tunnel processes, where holes can tunnel into the quantum dot while emitting an energy  $\Delta E$ . For both bias directions the tunnel rate into the dot increases, but it can only be observed in the measured current, if it concerns the barrier with the lowest tunnel rate, i.e. the source (upper left panel). Therefore the lines ending on the  $N = 1$  diamond are only visible at positive bias voltages in Figure 6.1B.

The situation is reversed in the rightmost panels, where holes can tunnel inelastically out of the dot (red arrows). Here the increase in outgoing tunnel rate only leads to an observable change in conductance at a negative bias (lower right panel), hence the lines ending on the  $N = 0$  diamond. Analogously, at higher bias voltages the  $n^{\text{th}}$  line corresponds to inelastic transport with a total energy emission of  $n\Delta E$ . Our measurements give values for  $\Delta E$  of 111,  $122 \pm 5$ ,  $180 \pm 10$  and  $106 \pm 5 \mu\text{eV}$  for respectively the  $0 \leftrightarrow 1$ , the  $1 \leftrightarrow 2$ , the  $2 \leftrightarrow 3$  and the  $3 \leftrightarrow 4$  transition. We stress that the lines *must* be directly connected to ground-state transport since the slopes of the lines are parallel to the ground state transport lines.

In Figure 6.2C the current-voltage characteristic shows a peak at each discrete energy level instead of a step as one might expect for an excited state. A tunnel event *with* energy emission does not have a higher rate than a tunnel event *without* energy emission, since additionally there has to be a process of energy absorption. The lower coupling of the inelastic tunnel events can also make their tunnel rate more sensitive for changes in  $V_{SD}$ , because the Schottky barrier is modified as the bias voltage increases, hence the peaks instead of steps.

In short, holes can tunnel inelastically into or out of the dot via discrete energy levels above or under the one-hole ground state level. We stress that these electrochemical potential levels, indicated by red dashed lines, are *not* available states for holes residing on the dot: only the ground state can be occupied (black straight line).

## 6.6 Discussion

The logical next question addresses the precise nature of the environment that absorbs the energy. We see three options: phonons, photons and resonances in the electric circuit. Energy emission via these mechanisms can explain the existence of energy levels below the  $N = 0$  ground state (Figure 6.1) and the insensitivity for changes in magnetic field (Figure 6.3).

In case of resonances in the electric circuit a standing electromagnetic wave would have to be confined to an open or closed cavity that is strongly coupled to the quantum dot. This can only take place in a homogeneous waveguide that has a large enough impedance mismatch with its direct electrical environment to reflect incoming electromagnetic waves. If such a cavity would exist on-chip, we can get an order of magnitude estimate for its size. The wave length corresponds to  $\lambda = hc/\Delta E$ , where  $c = c_0/\sqrt{\epsilon_r}$ , i.e. the speed of light in vacuum corrected by the dielectric constant of the medium under consideration. The measured energy steps of  $\Delta E = 100\mu\text{eV}$  or 24 GHz would then yield a wavelength of  $\sim 6$  mm. An open (closed) cavity would have a size of  $\lambda/4 \sim 1.5$  mm ( $\lambda/2 \sim 3$  mm). The thin films on chip leading from the Al bond wires to the device are constituted of six metallic segments of varying widths, thicknesses and materials (AuPd/Ni/NiSi), making it virtually impossible to create a high-Q cavity. Possibly the Al bonding wires that connect the chip to the wiring of the chip carrier could form a cavity. However, the nanostructures on-chip effectively operate as a low-pass filter, with a damping greater than 80% for frequencies above 100 MHz. Since the observed energies emission correspond to 24 GHz and the damping of a high-quality resonator must be less than 1%, we find this explanation unlikely.

If the energy is emitted to phonons or photons, there must be discrete empty states for the quantized emission. The energy quantum is then determined by the phonon or photon speed,  $v$ , and the length of the cavity,  $L$ , according to  $\Delta E = hv/2L$ . This allows us to estimate the order of magnitude of the cavity size required for an emission of  $\Delta E \sim 100\mu\text{eV}$ . Based on a speed of sound (light) of  $\sim 5000\text{ ms}^{-1}$  ( $3 \cdot 10^8\text{ ms}^{-1}$ ), the phonon (photon) cavity must be  $\sim 104\text{ nm}$  ( $\sim 6\text{ mm}$ ) long. If the energy is emitted to free photons the cavity could be the chip carrier in which we have glued the substrate with the quantum dot. However, since the chip carrier is not sealed off as a designed microwave cavity and the density of states of free photons is very small at energies of  $100\ \mu\text{eV}$ , emission of photons highly unlikely in this situation.

The third option of acoustic phonons is the most likely explanation. In case of a phonon wavelength,  $\lambda$ , of  $\sim 208\text{ nm}$ , the Si quantum dot of  $12\text{ nm}$  length is smaller than  $0.1\lambda$  and will hardly perturb the phonon. The cavity edges are situated at the transition from the amorphous Ni contacts to the crystalline NiSi, where the cross-sectional area drops stepwise by more than three orders of magnitude. The required cavity length of  $104\text{ nm}$  corresponds well to the total length of NiSi–Si–NiSi nanowire of  $250\text{ nm}$ .

An energy emission of  $n\Delta E$  can be interpreted by two possible scenarios: (i) one phonon with energy  $n\Delta E$  is sent out. Each line corresponds to one phonon mode of energy  $n\Delta E$ , hence the modes are equidistant in energy as in a harmonic oscillator potential. (ii)  $n$  phonons with energy  $\Delta E$  are emitted. Here only one phonon mode is used, so we have no knowledge of the phonon spectrum. Since we observe emission even up to  $13\Delta E$  (see Figure 6.3A), the electron-phonon coupling must be very strong in the latter scenario [93].

In conclusion, we have shown evidence for discrete energy levels that assist transport through a Si nanowire quantum dot. The additional transitions correspond to energy levels below the  $N = 0$  ground-state energy of the dot, which cannot correspond to electronic states of the quantum dot itself or to Zeeman states. The energy levels are quantized in multiples of  $100\text{-}180\ \mu\text{eV}$  and do not change with magnetic field. The magnitude of the quantization as well as the independence of magnetic field, and the presence of energy levels below the  $N = 0$  ground state level rule out the possibility of quantized states in the leads. Instead we attribute them to the emission of quantized energies during inelastic transport. The most likely explanation for the excitations is acoustic phonon emission to a cavity between two Ni contacts. The detailed analysis of our data on a single-hole silicon quantum dot marks a significant step to a better understanding of a phenomenon that is observed in single-charge quantum dots in nearly all material systems. Nevertheless it still requires a detailed theoretical explanation.

# Chapter 7

## Scanned probe imaging of quantum dots inside InAs nanowires

A. C. Bleszynski, F. A. Zwanenburg, R. M. Westervelt,  
A. L. Roest, E. P. A. M. Bakkers, & L. P. Kouwenhoven

We show how a scanning probe microscope (SPM) can be used to image electron flow through InAs nanowires, elucidating the physics of nanowire devices on a local scale. A charged SPM tip is used as a movable gate. Images of nanowire conductance versus tip position spatially map the conductance of InAs nanowires at liquid-He temperatures. Plots of conductance versus backgate voltage without the tip present show complex patterns of Coulomb-blockade peaks. Images of nanowire conductance identify their source as multiple quantum dots formed by disorder along the nanowire—each dot is surrounded by a series of concentric rings corresponding to Coulomb blockade peaks. An SPM image locates the dots and provides information about their size. In this way, SPM images can be used to understand the features that control transport through nanowires. The nanowires were grown from metal catalyst particles and have diameters  $\sim 80$  nm and lengths 2-3  $\mu\text{m}$ .

---

This chapter has been published in Nano Letters Vol. 7, No. 9, p. 2559-2562 (2007).

## 7.1 Introduction

An explosion in research activity on semiconducting nanowires has occurred in the past decade [94, 17, 18]. The ability to control the dimensions and composition of nanowire devices shows great promise for nanoelectronics, nanophotonics, and quantum information processing. Quantum effects are naturally important due to their small size, opening new possibilities for quantum devices.

InAs nanowires are a particularly attractive system for several reasons. InAs has a large  $g$ -factor, making it useful for spintronics and quantum information processing. Its large bulk exciton Bohr radius  $a_B = 34$  nm is comparable to the radius of nanowires studied in this paper, producing quantum confinement. While some semiconductors are known to have a surface depletion layer, the surface of InAs is known to have a charge accumulation layer. As a result, very small radius nanowires are not depleted of electrons, and one can make Schottky-barrier-free contacts to metallic leads.

Recent achievements in the field of semiconducting nanowires including single-electron control [45, 95, 96], high-performance field-effect transistors [97], and proximity-induced superconductivity [98, 99]. Progress requires an understanding of where the electrons are along the nanowire and how they flow through it. Standard transport measurements provide information about the conductance of the whole length of the nanowire [45, 95, 96] but do not provide detailed spatial information.

## 7.2 Scanned probe microscopy of InAs nanowires

Scanning probe microscope (SPM) imaging allows one to probe the motion of electrons along the nanowire locally, with high spatial resolution, and to modify the potential profile to allow or block electron transport. Cooled scanned probe microscopes have proven to be powerful tools for imaging and controlling electron flow in nanoscale systems including carbon nanotubes, a two-dimensional electron gas, and GaAs quantum dots [100, 101, 102, 103, 104, 105, 106]. Imaging techniques for nanowires are just being developed [107, 108].

In this Letter we present conductance images of InAs nanowires obtained with a liquid-He-cooled SPM. Plots of nanowire conductance  $G$  versus backgate voltage  $V_{BG}$  without the tip present show complex patterns of Coulomb blockade peaks with uneven spacings and heights. SPM images of nanowire conductance, using the tip as a movable gate, show the pattern of peaks is produced by multiple quantum dots located along the InAs nanowire, accidentally produced by disorder. Each dot is surrounded by a set of concentric rings of high conductance

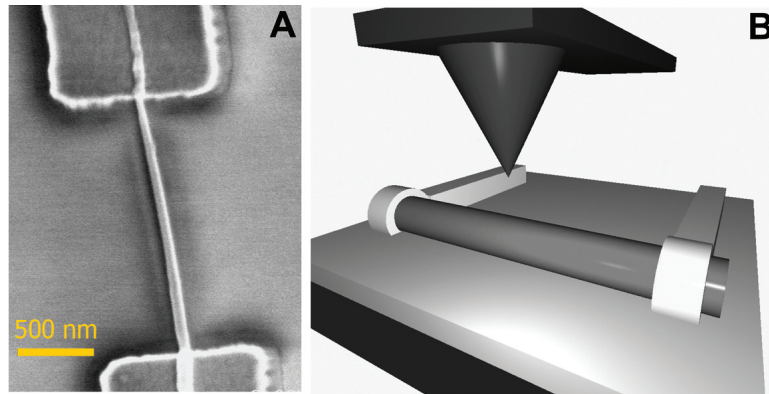


**Figure 7.1:** (A) SEM photo of an InAs nanowire (device D1) contacted with Ti/Al electrodes. (The slight kink in the wire at the top contact, due to an atomic force microscope (AFM) tip crash, occurred after the data presented in this paper was obtained.) The scale bar is 500 nm long. (B) Imaging schematic. A charged AFM tip is scanned  $\sim 100$  nm above the contacted InAs nanowire. Nanowire conductance as a function of lateral tip position is recorded to form an image. The wire lies atop a conducting Si substrate with a 250 nm thick  $\text{SiO}_2$  capping layer.

corresponding to Coulomb blockade conductance peaks [102]. The spacing and intensity of the rings about a dot provide information about the dot size and tunneling rate. The rings from nearby dots overlap. By using the tip as a movable gate, we can tune the charge state of each dot individually. These results show how a cooled SPM can be a powerful diagnostic tool for the development of nanowire devices.

The InAs nanowires were grown in a catalytic process from small gold seed particles using metal-organic vapor-phase epitaxy [109]. The nanowires have diameters  $\sim 80$  nm and lengths  $\sim 2\text{-}3$   $\mu\text{m}$ . After growth, the InAs nanowires are transferred onto a conducting p+ silicon substrate capped with a 250 nm thick  $\text{SiO}_2$  insulating layer. The silicon substrate acts as a backgate that can tune the number of charge carriers in the wire through an applied backgate voltage  $V_{BG}$ . Electron beam lithography is used to define electrodes  $\sim 2\text{-}3$   $\mu\text{m}$  apart, and 110 nm of Ti/Al is subsequently deposited to form the contacts. Figure 1A shows a scanning electron microscopy (SEM) picture of a contacted InAs wire. A home-built liquid-He-cooled SPM is used to image electrical conduction through the nanowires. As schematically shown in Figure 1B, an image is obtained by scanning a conducting SPM tip across a plane above the nanowire and recording the nanowire conductance  $G$  versus tip position with fixed  $V_{tip}$  and  $V_{BG}$  [102]. The conducting tip gates the nanowire locally, whereas the backgate gates the nanowire globally. The tip voltage  $V_{tip}$  creates a dip or peak in the electron density below. For an open nanowire, one can image electron flow by using the

tip to scatter electrons, thereby changing  $G$ . However, for a quantum dot in the Coulomb blockade regime, a different pattern is observed. An image of a dot shows a series of concentric rings corresponding to Coulomb blockade conductance peaks that occur as electrons are added to the dot. This Coulomb blockade imaging technique has been used to image multielectron quantum dots formed in carbon nanotubes [101] and a one-electron GaAs quantum dot [102].

### 7.3 Spatially mapping quantum dots

Parts A and B of Figure 2 show plots of nanowire conductance  $G$  versus backgate voltage  $V_{BG}$  for two InAs nanowire devices, D1 and D2; the nanowires are near pinchoff with  $G \ll e^2/h$ . Each plot shows an irregular series of peaks with variable spacing and amplitude similar to Coulomb blockade oscillations for multiple quantum dots in series [110, 21, 111]. The low conductance and the existence of complex patterns of peaks show the InAs nanowires are not spatially uniform. Without additional information, it is difficult to identify the source of these irregular oscillations.

The SPM conductance images in parts C and D of Figure 2 show the presence of multiple quantum dots located along each nanowire. Nested conductance rings occur about three positions along nanowire D1 in Figure 2C and about two positions along nanowire D2 in Figure 2D. Each ring corresponds to a Coulomb conductance peak of the quantum dot at the ring's center as electrons are added or removed by the SPM tip [101, 102]. The charge induced by the tip on a single dot is

$$q_{\text{ind}}(r_{t-d}, V_{t-d}) = C_{t-d}(r_{t-d}) \cdot V_{t-d}, \quad (7.1)$$

where  $r_{t-d}$  is the distance between the tip and the dot,  $C_{t-d}$  is the capacitance between the tip and the dot (assuming a conducting dot with a fixed geometry), and  $V_{t-d}$  is the voltage difference between tip and dot, including effects of the contact potential and the dot's capacitance to ground. Because  $C_{t-d}$  changes with tip position, the induced charge  $q_{\text{ind}}$  can be controlled either by the tip voltage  $V_{\text{tip}}$  or by the tip position  $r_{t-d}$ . If one were to plot  $G$  versus  $r_{t-d}$ , a conductance peak would occur every time the charge in the dot changes by one electron. In images, the conductance peaks take the form of closed rings centered on the dot that are contours of constant tip-to-dot capacitive coupling  $C_{t-d}$ . When the tip is between two rings, the dot charge remains constant at an integer multiple of the electron charge  $e$ .

The images in parts C and D of Figure 2 show that the complex conductance plots in parts A and B of Figure 2 were caused by multiple quantum dots in

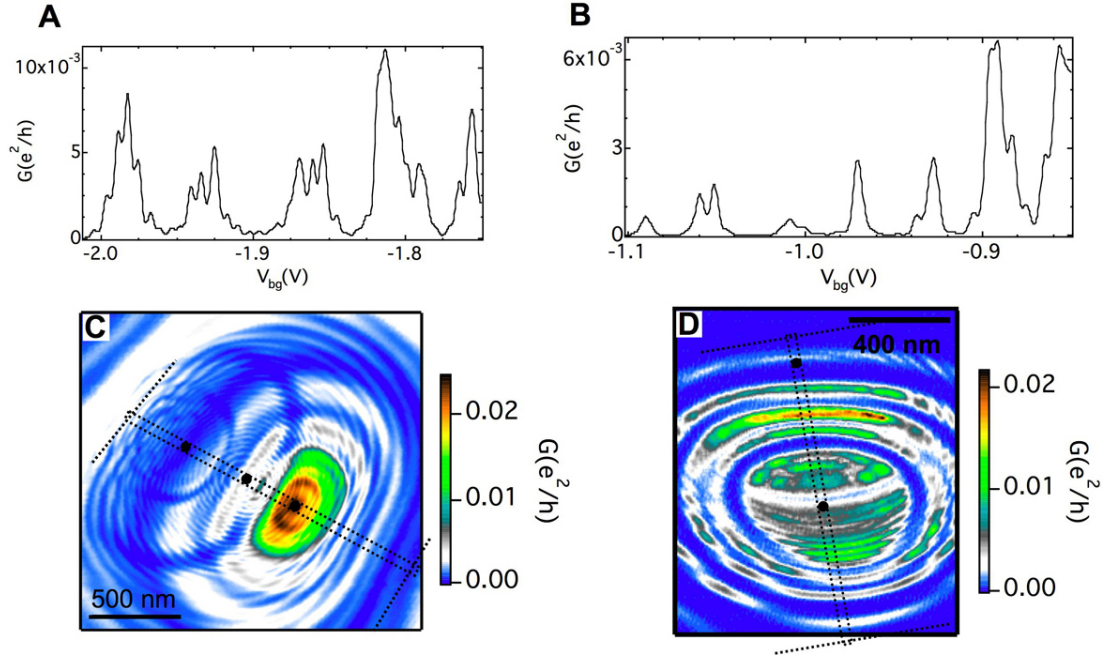


**Figure 7.2:** InAs nanowire transport measurements and corresponding images that spatially illuminate the behavior. **(A, B)** Nanowire conductance  $G$  vs backgate voltage  $V_{BG}$  for devices D1 and D2, respectively. The plots show a complex pattern of Coulomb blockade conductance peaks characteristic of multiple quantum dots in series. From these plots, it is difficult to determine the number and locations of the dots in each wire. **(C, D)** SPM images of devices D1 and D2, respectively, that display  $G$  vs position of a charged SPM tip scanned along a plane 100 nm above the nanowire. Concentric rings of high conductance, corresponding to Coulomb blockade peaks, are centered on quantum dots in the nanowire. **(C)** shows three sets of concentric rings identify three quantum dots whose positions are marked by black dots. **(D)** reveals rings surrounding two quantum dots in the nanowire. Dotted lines denote the outline of the wire and the electrical contacts.

series. In Figure 2C, three sets of concentric rings indicate the presence of three quantum dots at locations indicated by the black dots superimposed on the image. The rings surrounding the middle dot in D1 are more closely spaced than those surrounding the other two dots, indicating that the center dot is larger. In Figure 2D, two sets of concentric rings indicate the presence of two quantum dots, whose locations are again marked by black dots. In both parts C and D of Figure 2, the rings are elongated along an axis perpendicular to the wire due to a slight screening of the tip by the metal contacts. Formation of the quantum dots is accidental, presumably due to local potential fluctuations or defects in the nanowires.

## 7.4 Quantum dot size

The SPM images together with plots of  $G$  versus  $V_{BG}$  allow us to estimate the sizes of the quantum dots located along the nanowire. We use a simple model in which the capacitance  $C_{BG}$  between the dot and the backgate is given by the capacitance of a cylindrical nanowire segment [112] of radius  $r = 40$  nm and length  $L$  located at a height  $z$  above the backgate  $C_{BG} = 2\epsilon_r\epsilon_0L/\ln(2z/r)$ ; here  $\epsilon_0$  is the permittivity of a vacuum,  $z = 250$  nm is the thickness of the insulating SiO<sub>2</sub> layer, and  $\epsilon_r = 2.0$  is the average dielectric constant including both the SiO<sub>2</sub> layer and the gap between the nanowire and SiO<sub>2</sub> layer away from the line where they touch. The length  $L$  of a given dot can be estimated from the period of its Coulomb blockade conductance oscillation versus  $V_{BG}$ . For Figure 2A this is possible for the rapid oscillation. This rapid oscillation corresponds to the closely spaced rings about the middle dot in the image Figure 2C; the ring spacing for the other dots is larger. Comparing the backgate voltage period with the ring spacing for a given dot calibrates the image for all of the dots shown, so that the ring spacing for another dot can be used to estimate its length  $L$ , even if its conductance oscillation cannot be picked out of the  $G$  versus  $V_{BG}$  conductance plot. Using this procedure, we found the lengths of the three dots from left to right in Figure 2C for sample D1 to be  $L = 63, 520$  and  $140$  nm, and the lengths of the two dots from top to bottom in Figure 2D for sample D2 to be  $L = 400$  and  $122$  nm. The dot lengths vary, and some dots are longer than their diameter, as one might expect for accidental dots.

Using the SPM tip as a movable gate allows us to control the charge on one dot in a nanowire that contains many dots, like the devices shown here. The movable gate technique has a great advantage over static gating techniques for the manipulation of quantum dots in nanowires: The movable gate allows one to image and locate the position of one or more quantum dots along a nanowire. In addition, the SPM tip can be used to address an individual dot in a nanowire that contains multiple dots. Doing this can be difficult using lithographically defined gates if the dot locations are unknown or if the spacing between two dots is smaller than the lithographic resolution. The images in Figure 3 show how the nanowire conductance is pinched off by a negative backgate voltage to produce Coulomb conductance peak patterns characteristic of quantum dots in series [110]. The electron density is reduced everywhere in the nanowire, producing effectively higher barriers. A series of SPM images of device D1 are shown in parts A-C of Figure 3 for  $V_{BG} = -1.94, -2.05,$  and  $-2.12$  V, respectively. The small pink dots in Figure 3 show quantum dot locations, and the dashed ellipses in panels B and C of Figure 3 show the location of the rings for the two outer dots from Figure 3A.

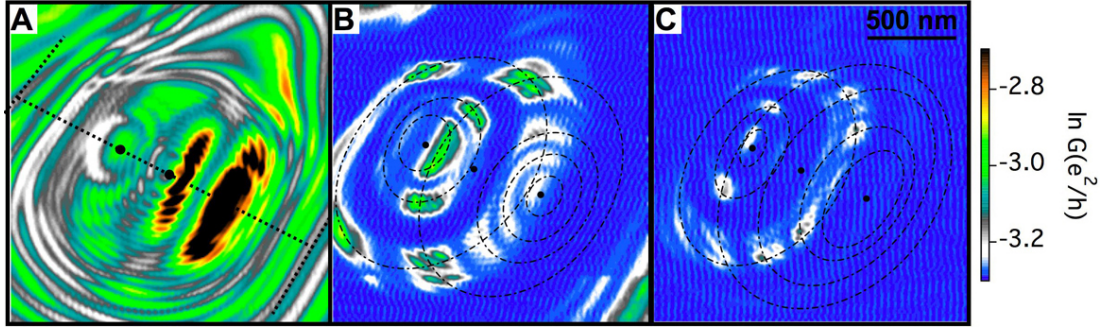


**Figure 7.3:** SPM images of conductance  $G$  for device D1 showing the interaction of Coulomb blockade rings from the three quantum dots in the nanowire. Pink dots mark the dot locations, and dashed lines show outlines of the nanowire and contacts in (A). The images were recorded with  $V_{tip} = 0$  V and backgate voltages (A)  $V_{BG} = -1.94$  V, (B)  $-2.05$  V, and (C)  $-2.12$  V. As  $V_{BG}$  is made more negative, conductance occurs only near the intersection of rings from different dots, where each dot is on a Coulomb blockade conductance peak. Elliptical dash-dotted rings in (B) and (C) show the location of rings in (A) from the two outermost dots. The expected rings for the middle dot have not been shown, because they are so closely spaced that their inclusion would clutter the image.

As the nanowire is depleted, conductance only occurs when all three dots are on a Coulomb blockade peak; this occurs at the intersections of conductance rings from different dots. Clearly seen in Figure 3C, this peaks at the intersection of conductance rings from different dots is the expected pattern for multiple quantum dots in series with negligible coupling between them [110].

## 7.5 Evolution of SPM images with tip voltage

The SPM images of device D2 in Figure 4 show how the Coulomb blockade rings from a given dot evolve as the tip voltage is increased from  $V_{tip} = 0.48$  to  $1.44$  V while keeping  $V_{BG}$  constant: the rings move radially outward, and their spacing decreases. In these images, a dominant set of rings is centered on the quantum dot in the upper half of the image. We can track the motion of an individual ring by taking a series of images with small increments in  $V_{tip}$  (see Supporting Information). A subset of these images is shown in Figure 4, where a superimposed black triangle is used to indicate the location of a particular ring. The radius grows as  $V_{tip}$  is increased, because the positive tip pulls more electrons onto the dot. It is difficult to estimate the absolute number of electrons, because the dot contains many electrons and we cannot deplete the number to zero. In

addition, the rings become more closely spaced as  $V_{tip}$  is increased, because the induced charge on the dot increases, in proportion to  $V_{tip}$ . So a smaller change in tip position and tip-to-dot capacitance  $C_{t-d}$  is needed to add or remove one electron.

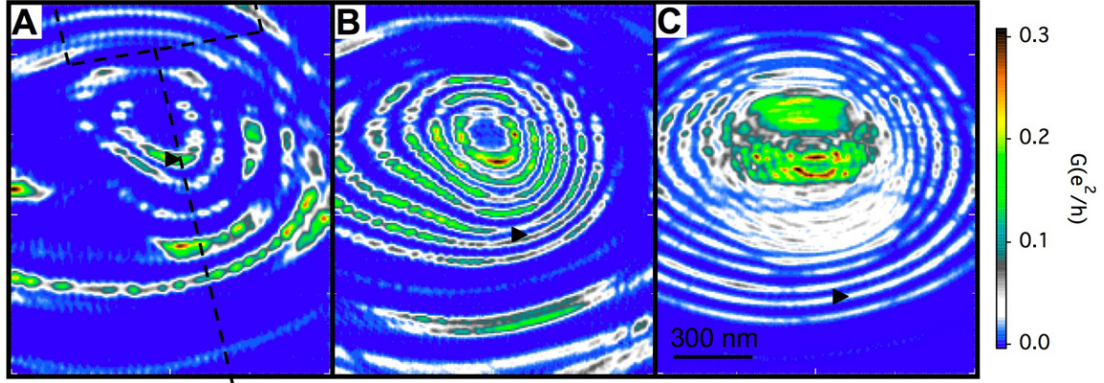


**Figure 7.4:** Evolution of SPM images of device D2 with tip voltages: (A)  $V_{tip} = 0.48$  V, (B) 0.90 V, and (C) 1.44 V. The wire and top contact are denoted with dashed lines in (A). Coulomb blockade rings surround a quantum dot in the upper half of the image. As  $V_{tip}$  increases, the rings expand outward in size and become more closely spaced. The black triangle tracks one Coulomb peak, demonstrating how the size of the rings grows with tip voltage.

We acknowledge useful discussions with Jorden van Dam, Silvano De Franceschi, Markus Brink, and Gary Steele. This work was supported at Harvard and at Delft by the Nanoscale Science and Engineering Center (NSEC), Grant NSF PHY-01-17795, and at Delft by funding from the Netherlands Organization for Scientific Research (NWO).

## 7.6 Additional material

The scanning probe microscope images of nanowire device D2 in Figure 7.4 are three images of a larger series. The full evolution of Coulomb rings moving outward is shown in Figure 7.5.

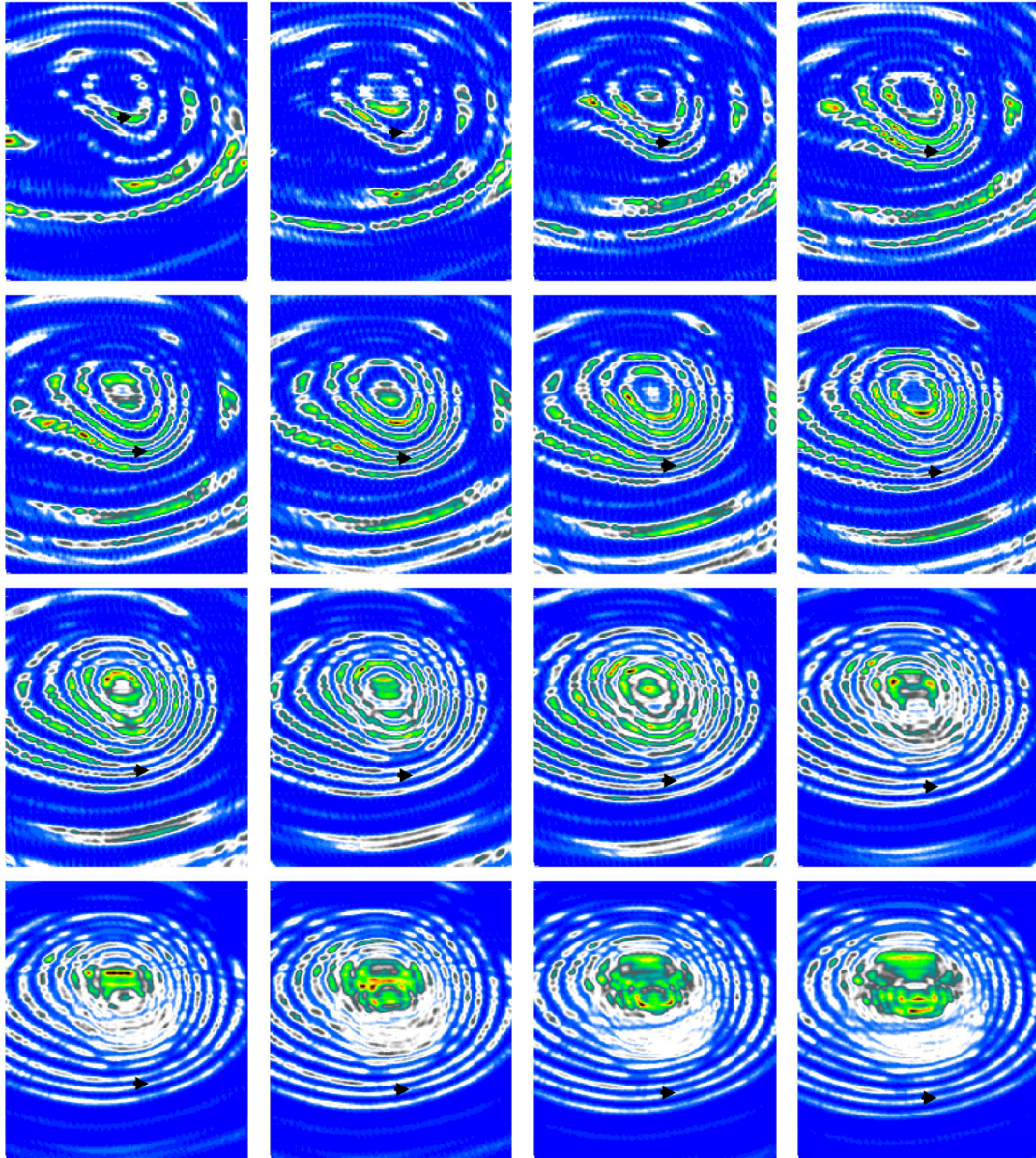


**Figure 7.5:** Series of cooled scanning probe microscope images of nanowire device D2 taken as the tip voltage varied from 0.48V to 1.40V, from top left to bottom right. The black arrow on each frame tracks the Coulomb ring corresponding to the addition of the  $n^{\text{th}}$  electron, where  $n$  has the same value in each image.



# Chapter 8

## Electric field control of magnetoresistance in InP nanowires

F. A. Zwanenburg, D. W. van der Mast, H. B. Heersche,  
E. P. A. M. Bakkers & L. P. Kouwenhoven

We demonstrate electric field control of sign and magnitude of the magnetoresistance in InP nanowires with ferromagnetic contacts. The sign change in the magnetoresistance is directly correlated with a sign change in the transconductance. Additionally, the magnetoresistance is shown to persist at such a high bias that any possible form of Coulomb blockade has been lifted. We also observe the magnetoresistance when one of the ferromagnets is replaced by a non-magnetic metal. We conclude that it must be induced by a single ferromagnetic contact, and that spin transport can be ruled out as the origin. Our results emphasize the importance of a systematic investigation in order to discriminate between ambiguous interpretations.

---

The results in this chapter will be submitted for publication.

## 8.1 Introduction

The realization of the field effect transistor in 1947 may be the greatest invention of the 20th century, allowing the development of modern-day electronics. The discovery of the giant magnetoresistance in multi-layers of magnetic and nonmagnetic metals [113, 114] has had an enormous impact on the data storage industry. It opened the field of spintronics which wants to exploit both the spin and charge degree of freedom of electrons for useful devices [3, 4, 5]. The proposal of Datta and Das, that combines the functionalities of semiconductors and magnetic materials into a spin transistor [115], has triggered many research groups to pursue its experimental realization.

The typical signature of giant magnetoresistance, or spin valve effect, is the onset of a low and high resistance state for parallel (P) and anti-parallel (AP) orientations of the magnetizations of two ferromagnets. These different magnetization directions result in different densities of states for spin-up and spin-down electrons at the Fermi energy. In metallic systems this is a well-understood phenomenon, but it took almost a decade until the first demonstration was claimed on carbon nanotubes with ferromagnetic contacts [116], after which many followed [117, 118, 119, 120, 121, 122].

However, the Magneto-Coulomb effect can have the exact same signature, resulting in ambiguous interpretations of spin transport experiments [123]. Magneto-Coulomb oscillations were first observed in ferromagnetic single electron transistors in 1997 [124, 125]. These experiments showed how amagnetic field can induce single electron charging effects: a change in magnetic field  $B$  shifts the densities of states for spin-up and spin-down electrons in a ferromagnet by the Zeeman energy  $\Delta E_Z = \pm g\mu_B B/2$ . Here  $g$  is the gyromagnetic ratio,  $\mu_B$  the Bohr magneton and the sign is negative (positive) for spin-up (spin-down). The total number of electrons stays constant, and as a consequence the chemical potential has to change by  $P\Delta E_Z$ , with  $P$  the spin polarization at the Fermi energy. If the ferromagnet is capacitively coupled to the metallic island of a single electron transistor, the resulting modification in work function acts as a voltage on a gate. Via this mechanism a magnetic field can give rise to single electron charging effects. Along these lines the Magneto-Coulomb effect should also be observable in semiconductors contacted by ferromagnets.

If one wants to inject and detect spins electrically, the non-local measurement of a spin imbalance [126, 127] is generally regarded as the best configuration to exclude misleading effects that leave the same signature. Only recently three non-local experiments have been reported in non-metallic systems, namely carbon nanotubes [128], GaAs [129] and graphene [130]. The results on carbon nanotubes

with ferromagnetic contacts [117, 118, 119, 120, 121, 122] were all carried out in a 2-point (or ‘local’) geometry. They observed the typical spin valve-like signal of a low- and high resistance state for parallel (P) and anti-parallel (AP) orientations of the magnetizations of the ferromagnetic electrodes.

Here we present the first experiments on semiconductor nanowires with ferromagnetic contacts. We use InP nanowires that are contacted with both ferromagnetic and non-magnetic metals, allowing for discrimination of spin transport effects and the Magneto-Coulomb effect, thus avoiding ambiguous interpretations of the experiments. We demonstrate electric field control of the sign and magnitude of the magnetoresistance in these devices. Additionally, the magnetoresistance is shown to persist at such a high bias that any possible form of Coulomb blockade has been lifted.

Crystalline InP nanowires are grown from gold catalyst particles via a vapor-liquid-solid process [23, 109, 131]. During growth Se is incorporated as dopant atom (100 ppm Se) aiming at  $10^{18}$  electrons/cm<sup>3</sup>. The effective doping level is higher due to extra impurity incorporation, resulting in an electron density of  $\sim 10^{19}$  cm<sup>-3</sup>. The typical diameter is 50 nm and lengths vary from 5 to 20 micron. After growth we deposit the nanowires on a thermally oxidized silicon wafer with 250nm SiO<sub>2</sub>. The silicon is highly doped, enabling use of it as a backgate to induce an electric field in the nanowires. Predeposited markers allow locating individual nanowires and definition of electrodes by means of electron-beam lithography. Before metal deposition, the samples are treated with buffered hydrofluoric acid for 5s in order to etch off the native oxide layer around the nanowires. We then evaporate 100nm of the alloy Co<sub>80</sub>Fe<sub>20</sub> for ferromagnetic contacts. After a second lithography step and etch treatment, 110nm Ti/Pt is deposited for non-magnetic contacts. In the experiments shown here the distance between the contacts is varied from 200 to 460nm. The resulting two-point resistances are typically 20-80 k $\Omega$ , but can be as low as 5 k $\Omega$ . For both CoFe-InP and Ti/Pt-InP the contact resistance is estimated between 1 and 10k $\Omega$ . The high carrier concentration results in a very thin Schottky barrier. At low temperature we see an increase in differential resistance around zero bias, but no sign of Coulomb blockade. Measurements of the conductance versus source-drain and backgate voltage show an interference pattern which most likely originates from universal conductance fluctuations or Fabry-Pérot-like interference between source and drain contacts. The presented data in this paper are taken at 1.6-1.8 K in a pumped <sup>4</sup>He-cryostat. We only show 2-terminal measurements, where we bias a DC current from source to drain and measure the source-drain voltage.

## 8.2 Electric field control of magnetoresistance

Figure 8.1A shows a scanning electron micrograph of device A, an InP nanowire with four CoFe (F) contacts. Two contacts have a width of 100 nm and the other two 300 nm, resulting in different coercive fields: when the magnetic field is swept parallel to the easy axis of the contacts, the magnetizations of the wider (300 nm) electrodes will switch before the two 100 nm electrodes. This allows us to measure the device resistance both with parallel (P) and anti-parallel (AP) magnetizations of the involved electrodes. The distance between the contacts is about 200nm, and the device has a resistance of 10 k $\Omega$  at zero gate voltage. The devices B and C (later in this paper) have almost identical designs and differential resistances of 15-20 k $\Omega$  and 140-260 k $\Omega$  respectively.

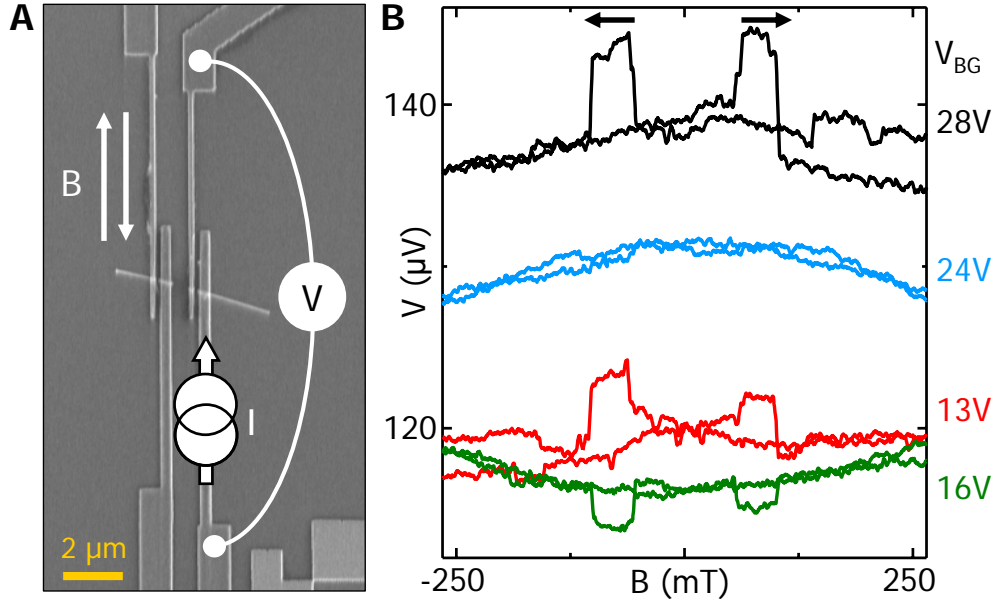


**Figure 8.1: Electric field control of magnetoresistance.** (A) SEM of device A, an InP nanowire with four CoFe contacts. The electrodes have different widths (100 nm and 300 nm) in order to realize different coercive fields. We perform 2-terminal measurements on the two rightmost contacts, which are separated by 220 nm. The wire part between the middle contacts has broken off after metal lift-off and is not used for measurements. We bias a DC current  $I$  from source to drain and measure the source-drain voltage  $V$ . The other contacts are floating. (B) Magnetic field sweeps at 2K of the voltage at a current bias of 10 nA for different values of the backgate voltage. The magnetic field is swept up and down parallel to the easy axis of the electrodes; arrows indicate the sweep direction. At 3 of the 4 backgate voltages the magnetization switches at  $\pm 55$  and  $\pm 100$  mT result in jumps in the measured voltage varying from -1.4% to +2.3%.

The magnetization switches are clearly visible in the measured voltage at a constant current bias of 10nA, see Figure 8.1B. When the magnetic field is swept in the positive direction, jumps in the voltage appear at 55 and 100 mT. Going to negative fields two jumps are seen symmetrically in B-field. Between  $\pm 55$  mT and  $\pm 100$ mT the two ferromagnets have anti-parallel magnetizations. Outside these regions they are aligned parallel, either in the positive or negative B-field direction. Four sets of traces are shown at backgate voltages of 13V, 16V, 24V and 28V. When we define the magnetoresistance as  $(R_{AP} - R_P)/(R_{AP} + R_P)$  we find respective values of 1.4%, -1.0%, 0% and 2.3% for these gate voltages. Besides observing the 2-terminal magnetoresistance in more than twenty different F-InP-F devices, we have also measured the magnetoresistance of a nanowire in a 4-point geometry: we measured the voltage between the inner two contacts of a nanowire, with a constant bias current through the outer two electrodes (all ferromagnetic). This resulted in the same magnetoresistance as in a 2-point measurement on the inner two contacts, both qualitatively and quantitatively. The results in Figure 8.1 demonstrate that we can control and even turn off the magnetoresistance by means of an electric field.

### 8.3 Relation between transconductance and magnetoresistance

Now we look in more detail at the relation between the sign of the magnetoresistance and the transconductance. We perform the same magnetic field sweeps on device B. With no gate voltage applied this device has a differential resistance of 18k $\Omega$  at zero bias and 15k $\Omega$  at a bias of 100nA. When we take magnetic field sweeps while stepping the different gate voltage from 17 V to 26.5 V, it turns out that the change in resistance with electric field ( $\sim 20\%$ ) is much bigger than the sudden change due to the switches ( $\sim 0.5-1\%$  in this device). Plotting the numerical derivative  $dV/dB$ , which is proportional to the magnetoresistance, allows us to discern the magnetization switches.

Figure 8.2A shows a grayscale plot of  $dV/dB$  versus backgate voltage and magnetic field. The switches appear as horizontal alternating black and white lines at  $\pm 80$ ,  $+150$  and  $\pm 190$  mT. In the measurement set-up the magnetic field was not aligned with the easy axis but under a non-zero angle with the electrodes. This results in higher switching fields for both CoFe contacts, and one of the electrodes switches in two parts (at 150 and 190mT). The switching lines change from black to white or vice versa a couple of times, corresponding to a sign change in magnetoresistance. The middle panel shows several minima and maxima in the

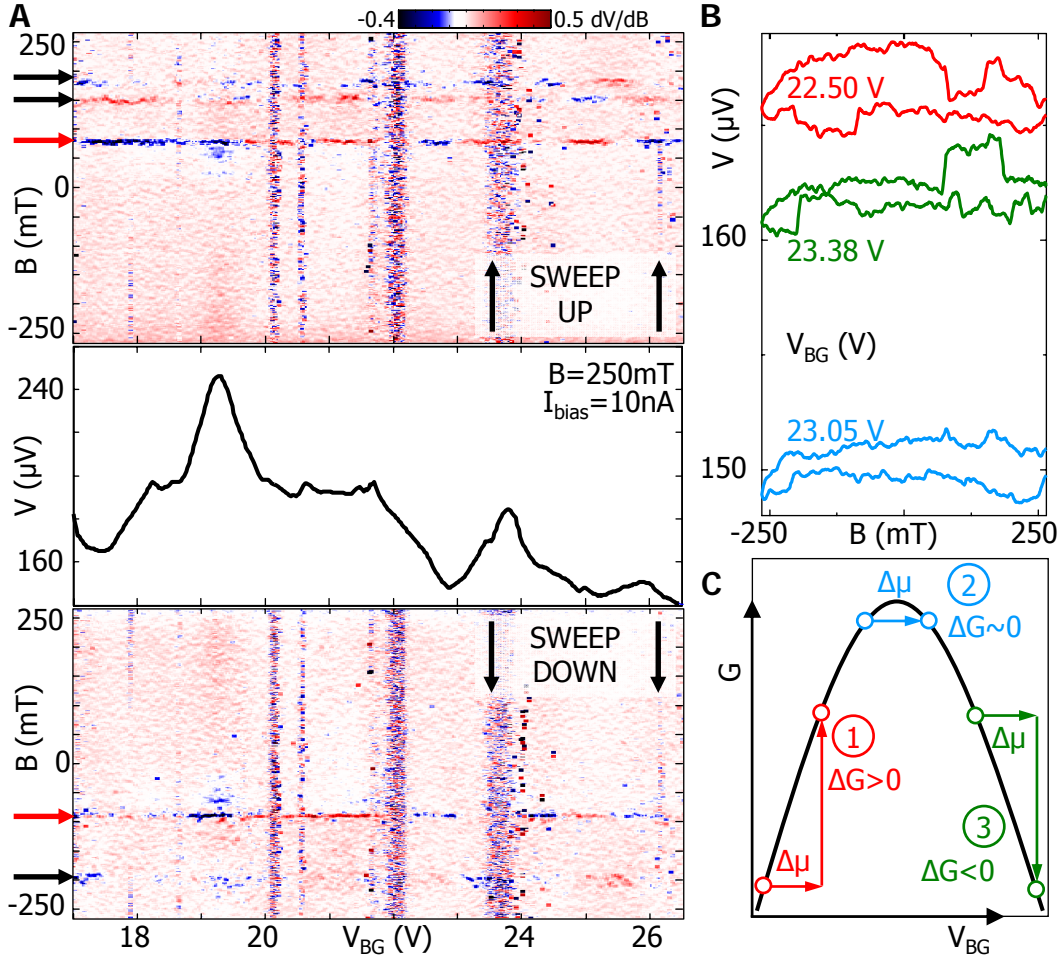


**Figure 8.2: Relation between transconductance and magnetoresistance.** (A) For device B the voltage is measured at a current bias of 10 nA. The grayscale plots show the numerical derivative  $dV/dB$  versus magnetic field and gate voltage. The upper (lower) panel depicts the magnetoresistance while sweeping the magnetic field up (down). White (black) represents a positive (negative) magnetoresistance. Three switches are visible at  $\pm 80$ ,  $+150$  and  $\pm 190$  mT. The first can be attributed to the 300 nm wide CoFe electrode, and the latter two to the 100 nm contact (its magnetization switches in two steps). The middle panel shows a line cut of the measured voltage versus gate voltage at  $B=250$  mT, taken from the upper panel. (B) Line cuts of (A) at three different gate voltages. The magnetoresistance changes sign while the normal resistance goes through a minimum at  $V_{BG}=22.9$  V. (C) Schematic explaining sign change of the conductance in case of the Magneto-Coulomb effect. If the chemical potential  $\mu$  of one of the ferromagnetic contacts changes by an amount  $\Delta\mu$ , it results in an effective  $\Delta V_{BG}$  on the device. The change in conductance  $G$  depends on the position in gate space. When the conductance goes through a maximum it can change from  $\Delta G > 0$  (before the maximum, situation 1) to  $\Delta G = 0$  (situation 2) to  $\Delta G < 0$  (situation 3).

normal resistance versus backgate voltage. The three line cuts in Figure 8.2B are taken around the minimum at  $V_{BG}=22.9\text{V}$ . The sign of the magnetoresistance changes from negative at  $V_{BG}=22.5\text{V}$  to zero (at  $V_{BG}=23.05\text{V}$ ) to positive (at  $V_{BG}=23.38\text{V}$ ). We have observed this in devices A and C as well. These results show that a sign change in the transconductance,  $dG/dV_{BG}$ , goes together with a sign change in the magnetoresistance.

## 8.4 Magneto-Coulomb effect and spin transport

The origin of this relation can be understood by both the Magneto-Coulomb effect and spin transport. We will explain both, starting with the latter.

The experiments on carbon nanotubes with ferromagnetic contacts are in the coulomb blockade regime, and the presented magnetic field sweeps display the spin-valve signature. Different mechanisms are suggested to explain the data, namely spin injection, spin-dependent quantum interference and spin-dependent coupling between quantum dot and lead. The latter two [121, 122] reported the correlation of sign changes of their magnetoconductance with resonances in the normal conductance, just like in Figure 8.2A and B. Man et al. add the disappearance of the effect on increasing the voltage bias of the device[122].

The Magneto-Coulomb effect has been demonstrated and carefully explained for the first time in metallic devices by Ono et al. [125]. In this case, a change in magnetic field shifts the densities of states for spin-up and spin-down electrons in a ferromagnet by the Zeeman energy  $\Delta E_Z = \pm g\mu_B B/2$ . Since the spin-up and spin-down densities of states differ and the total number of electrons stays constant, the chemical potential has to change by

$$\Delta\mu = Pg\mu_B B/2. \quad (8.1)$$

Here  $P$  is the spin polarization of the electron density of states at the Fermi energy of the ferromagnet. The work function of the ferromagnet changes by the same amount as  $\mu$ . When the ferromagnet is capacitively coupled to an island via a capacitance  $C$ , the charge on the island changes by  $\Delta q = C\Delta\mu/e$  [123]. Adding up all contributions leads to the total accumulated charge

$$\Delta q = C_S\Delta V_S + C_D\Delta V_D + C_{BG}\Delta V_{BG}, \quad (8.2)$$

where the subscripts  $S$ ,  $D$  and  $G$  refer to source, drain and gate. Equations (8.1) and (8.2) demonstrate how an applied magnetic field can change the electric field experienced by the device (Figure 8.2C). The corresponding change in the conductance depends on the position in gate space. When the conductance goes

over a peak it can change from  $\Delta G > 0$  (before the peak, situation 1) to  $\Delta G = 0$  (situation 2) to  $\Delta G < 0$  (situation 3). This is an adequate explanation for the magnetoresistance at different gate voltages as shown in Figure 8.1CB.

We stress that in order for the latter effect to be observed *only one* ferromagnetic contact is sufficient. In contrast, electrical detection of spin transport requires spin coherence from one ferromagnet to another, and therefore *at least two* ferromagnets are necessary for that experiment. Using only one ferromagnetic contact results in two possible scenarios: (i) The signal is absent, indicating spin transport as the origin. (ii) The signal of one magnetization switch is present, proving that the Magneto-Coulomb effect causes the magnetoresistance.

## 8.5 Magnetoresistance with one ferromagnet

To find out which effect comes into play in our experiment we have fabricated devices with *both* ferromagnetic *and* normal contacts to InP nanowires. We have performed magnetic field and electric field sweeps on device C, which has three working CoFe contacts and one working Ti/Pt contact, see Figure 8.3A. The differential resistance of both combinations CoFe-InP-CoFe (F-InP-F) and CoFe-InP-Ti/Pt (F-InP-N) is  $\sim 230$  k $\Omega$  at zero bias and  $\sim 150$  k $\Omega$  at a bias of 100 nA. Figure 8.3B shows the magnetoresistance in grayscale versus gate voltage for the F-InP-F configuration.

Just like in Figure 8.2 three distinct resistance jumps show up at  $\pm 60$ ,  $\pm 110$  and  $+170/-200$  mT, which we can relate to the coercive fields of F1 ( $\pm 110$  mT and  $+170$  mT/ $-200$ ) and F2 ( $\pm 60$  mT). Contrary to the measurements of Figures 8.1 and 8.2 the magnetoresistance barely changes with respect to gate voltage. The reason is that the gate dependence of the conductance has no minima or maxima: at this current bias the conductance only goes up with increasing gate voltage, see middle panel of 8.3B. When we carry out the same measurement in the F-InP-N configuration, we still see the two jumps that correspond to the magnetization switching of F1 (Figure 8.3C), but the coercive field of F2 at  $\pm 60$  mT is no longer visible. We observe the same signature at a current bias of 3 nA. Apparently we do not need two ferromagnetic electrodes to observe a resistance jump caused by a magnetization switch. We conclude from Figure 8.3 that the magnetoresistance is induced by a single ferromagnetic contact.

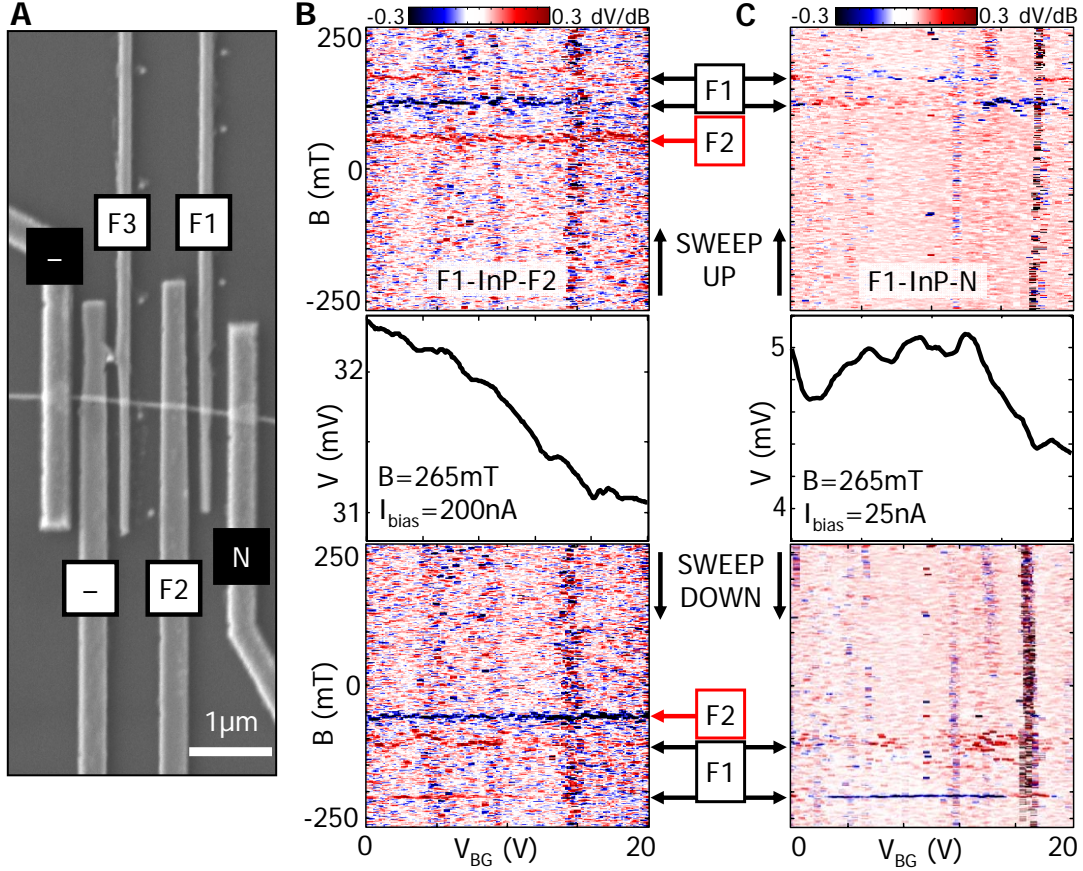


**Figure 8.3: Magnetic field sweeps on device C: an InP wire with four ferromagnetic and two normal contacts.** (A) SEM of the device. The two leftmost electrodes are not connected. (B) F1-InP-F2: we measure  $V$  from F1 to F2 in the range  $V_{BG}=[0,20V]$  at a current bias of 200 nA while sweeping the magnetic field up (top panel) and down (bottom panel). By plotting  $dV/dB$  in grayscale the jumps caused by the magnetization switches are highlighted. In both sweep directions *three* magnetization switches are visible at  $\pm 60$ ,  $\pm 110$  and  $\pm 170/-200$  mT. The first switch can be attributed to F2, and latter two to F1. (C) F1-InP-N: we measure  $V$  from F1 to N at a current bias of 25 nA. The switch of F2 at  $\pm 60$  mT has disappeared. However, the *two* switches at  $\pm 110$  and  $\pm 170/-200$  mT are still visible. Both are caused by the magnetization switching of F1, which means that the observed magnetoresistance is induced by *one* ferromagnetic contact alone.

## 8.6 Magnetoresistance at high bias

We have also investigated whether the magnetoresistance remains at high current bias. Figure 8.4A shows the magnetic field sweeps on device C while the current bias is swept from 10 to 400nA. Here we use F2 and the third ferromagnetic contact F3, with an InP channel length of 460nm. Throughout the entire bias

range jumps appear at  $\pm 60$  and  $\pm 170$  mT, caused by the magnetization switches of respectively F2 and F3. Above 250 nA the jumps are more difficult to resolve due to instability of the device, but they are present nevertheless. The sign and relative magnitude of the magnetoresistance do not change when the bias current is increased up to 400 nA.

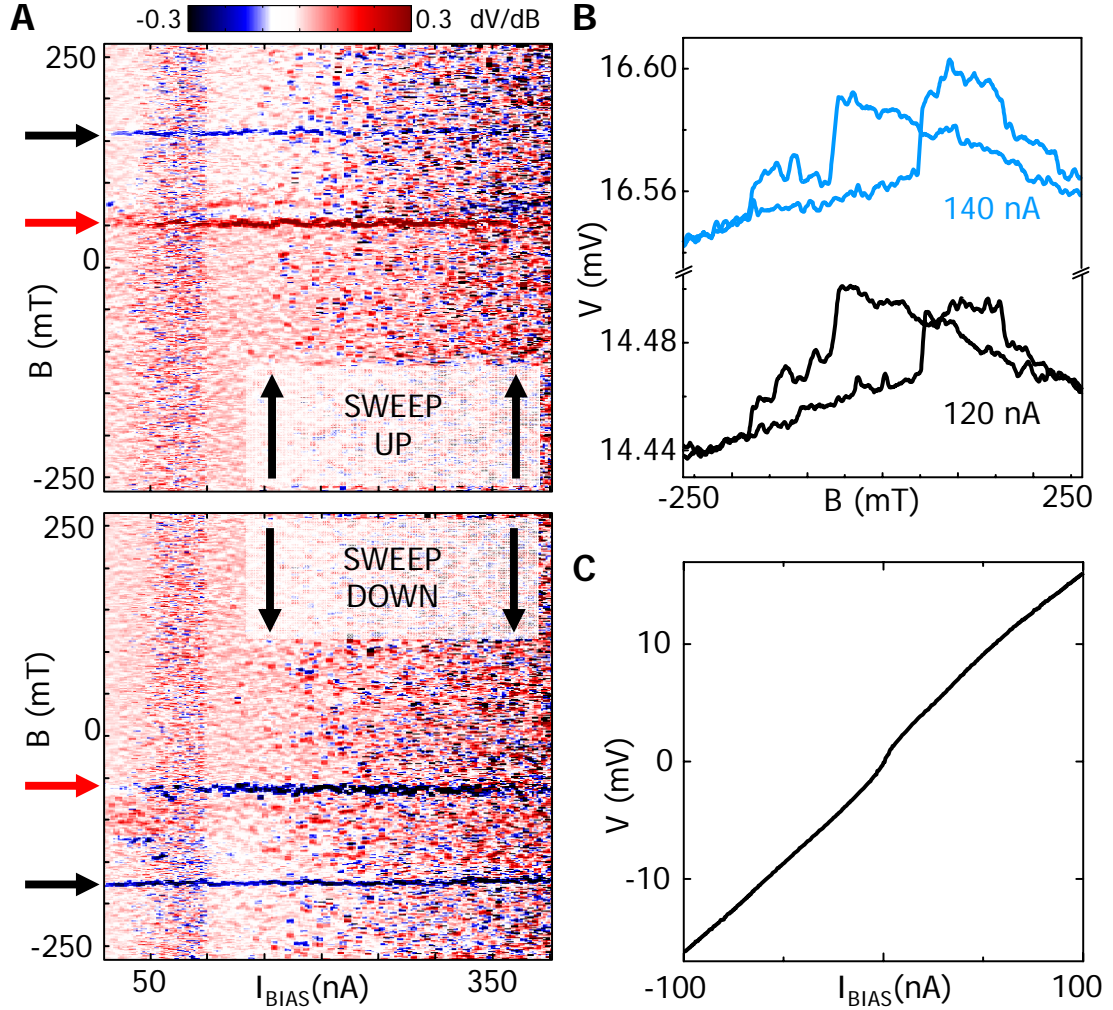


**Figure 8.4: Bias dependence of the magnetoresistance of device C.** (A) The upper (lower) panel shows  $dV/dB$  in grayscale versus current bias while the magnetic field is swept up (down). This is the same device as in Figure 8.3, but here we use F2 and F3. The gate voltage is kept at  $V_{BG}=0$  V. The sign and magnitude of the magnetoresistance do not change with increasing bias current. (B) Line cuts of (A) at current biases of 120 nA and 140 nA. The two voltage jumps in the negative sweep direction have the same sign. (C)  $V$  vs  $I$  at zero B-field and zero gate voltage.  $dV/dI$  varies from 130 k $\Omega$  at 100 nA to 260 k $\Omega$  at zero bias.

In the negative sweep direction of both traces two jumps in voltage of about -20 and -10  $\mu\text{V}$  are visible at -60 and -170mT, corresponding to a conductance change of 0.1 and 0.05%. In Figure 8.4C we plot the IV of F2-InP-F3. The presence of the switches at high bias indicates that single electron charging is not necessary to observe the coercive fields of the ferromagnets. This is confirmed by Figure 8.3B where the switches appear at a high bias of 200 nA. In order to be complete we have measured the bias dependence of device B as well, and saw no change in the magnetoresistance when the bias was varied from 1 nA to 225 nA (not shown here). The results in Figure 8.4 demonstrate that the magnetoresistance persists at such a high bias that any possible form of Coulomb blockade has been lifted.

The data in Figures 8.3 and 8.4 demonstrate that we are dealing with a ferromagnetic contact-induced effect, visible without the necessity of Coulomb blockade. Figure 8.3 demonstrates that the observed magnetoresistance is not related to coherent spin transport from one ferromagnet to another. Also, the fact that both voltage jumps in the negative sweep direction can go down (e.g. fig. 8.4B, down-sweep) means there are more than two resistance levels in a magnetic field sweep. That makes it impossible to refer to low- and high-resistance states of the device as the direct result of P and AP configurations of the ferromagnets.

## 8.7 Discussion

Next we will discuss four possible interpretations of our measurements: spin transport in InP nanowires, a *direct* measurement of the work function, the Magneto-Coulomb effect (an *indirect* measurement of the work function) and magnetic field dependent contact resistances.

### 1. Spin transport in InP nanowires

Spin transport can suffice to explain the results in Figures 8.1 and 8.2, along the same lines as the mechanisms in refs [121] and [122]. However, it is ruled out by four observations: (i) The presence of the signal with only one ferromagnetic contact (Figure 8.3), since spin transport requires coherent spin transport between two ferromagnets. (ii) The presence of more than two magnetoresistance levels in some devices (e.g. Figure 8.4), instead of only high-resistance (AP) and low-resistance (P) states. (iii) Its presence in the absence of single electron charging, whereas other reports only see the magnetoresistance at low bias [121, 122]. (iv) The absence of a spin-valve like signal in the non-local experiment: in that geometry we measure a magnetic hysteresis with only *one* visible switch (not shown

here). We have measured the non-local voltage in more than 20 different samples at different current biases and gate voltages, but we never observe a spin-valve like signal.

2. *Direct measurement of the work function*

One could argue that the magnetically induced change in ferromagnetic work function is added *directly* to the measured voltage instead of *indirectly* via a capacitive coupling, appearing as voltage jumps at the magnetization switches. Two arguments contradict this interpretation: (i) If the change in work function were to result in a permanent voltage drop in the electronic circuit, then it would be able to generate a current *without* an externally applied voltage bias. The sudden change in work function is comparable to the formation of a Schottky barrier: it results in a very brief charge rearrangement between metal and semiconductor, but it cannot induce a constant current flow for reasons of energy conservation. (ii) Since a ferromagnet is not affected by electric fields, the magnetoresistance should be the same for all gate voltages. The gate dependence of the magnetoresistance in Figures 8.1 and 8.2, however, shows a clear gate dependence.

3. *Magneto-Coulomb effect*

Unlike spin transport the Magneto-Coulomb effect can be responsible for all our observations, because we have to do with an *electrostatic* effect accompanied by the individual *magnetization* switches of the ferromagnets. As long as the non-magnetic material has an electric field dependent conductance and a strong enough capacitive coupling to the ferromagnet, the change in chemical potential will be observable. Since it is an electrostatic effect, the sign and magnitude of all individual jumps depend on the transconductance  $dG/dV_{BG}$  in that specific situation just before the magnetization switch. After each switching event the position in gate space of the semiconductor has changed, and this determines the effect of the next switch. We cannot pinpoint the origin of the sign of all switches in our data, but the Magneto-Coulomb effect allows the signs of two consecutive switching events to be the same, like in Figure 8.4B.

4. *Magnetic field dependent contact resistances*

A two-point measurement (e.g. F-InP-F) incorporates the sum of the InP nanowire resistance,  $R_W$ , and two F-InP contact resistances,  $R_C$ . A change in work function as in equation (8.1) raises the CoFe-InP Schottky barrier by the same amount, implying a higher  $R_C$ , so we can readily expect jumps as in Figures 8.1-8.4. Since the Schottky barrier (and hence also  $R_C$ ) de-

depends on the electric-field dependent carrier density in InP [28], changes with respect to gate voltage as observed in Figures 8.1 and 8.2 cannot be excluded. This interpretation is challenged by the persistence of the magnetoresistance in four-terminal measurements. In that geometry the current runs underneath the contacts if  $R_C \gg R_W$ , and the outcome gives  $R_W$ . However, if  $R_C \sim R_W$ , the current will cross the Schottky barrier and the magnetic field dependent contact resistance can emerge.

The first two interpretations can be eliminated as plausible explanations of the magnetoresistance, leaving a further investigation of the latter two. The mechanism of magnetic field dependent contact resistances is in fact a Magneto-Coulomb effect. Due to the low contact resistances we cannot discriminate between the two, so we can reduce the discussion to an investigation of the Magneto-Coulomb effect.

The experimental value of the chemical potential change can be derived from a comparison of the magnitudes of the backgate effect and the magnetoresistance in one and the same device. The voltage jumps of device C in Figure 8.3B are typically  $30 \pm 10 \mu\text{V}$  at all gate voltages. At this current bias the measured voltage decreases with increasing gate voltage by roughly  $60 \mu\text{V}/\text{V}$ , see middle panel of Figure 8.4B. In other words, a change in backgate voltage  $\Delta V_{BG}$  of  $500 \pm 167 \text{ mV}$  induces a change of  $30 \mu\text{V}$ , i.e. equal to the effect of one magnetization switch. When the two effects are equally strong we can write

$$C_S \Delta\mu/e = C_{BG} \Delta V_{BG}. \quad (8.3)$$

A realistic value for the ratio of the capacitances  $C_{BG}/C_S$  is 0.33, based on a 50 nm diameter wire and a 200 nm contact distance<sup>1</sup>. By combining  $C_{BG}/C_S = 0.33$  with equation (8.3) we find an experimental change in chemical potential  $\Delta\mu$  of  $165 \pm 55 \text{ meV}$ . We get comparable numbers for devices A and B. Equation (8.1) yields a theoretical value for  $\Delta\mu$  of  $5 \mu\text{eV}$ , if we use  $P=0.4$ ,  $B=0.2 \text{ T}$ ,  $g=2$  and  $\mu_B = 9.7 \cdot 10^{-24} \text{ J/T}$ . The theoretical prediction is four orders of magnitude smaller than the empirical value.

At first sight, the enormous discrepancy throws strong doubts on the Magneto-Coulomb effect as the origin of the observed magnetoresistance, and asks for an evaluation of theory and experiment. The theoretical number of  $5 \mu\text{eV}$  seems extremely small when compared to the work function of CoFe of about 5 eV. Intuitively one expects a negligible effect on transport, especially in case of the highly doped InP. On the other hand, the experimental number of 165 meV is in itself not an oddly huge number when compared to the work function of CoFe

<sup>1</sup>Numerical simulations based on the Poisson equation yield  $C_{BG}=4.3 \text{ aF}$  and  $C_S=13 \text{ aF}$ .

of about 5 eV. One explanation could be that the effective magnetic field in equation (8.1) is higher due to shape anisotropy of the ferromagnetic contacts at the F-InP interface. The surface charges of the CoFe contacts add a component to the external magnetic field. This demagnetizing field will not be larger than 1 T, which can contribute up to 50  $\mu\text{eV}$  to theoretically expected change in work function. Moreover, a recent report has investigated the magnetoresistance of single metallic nanoparticles contacted with Co [132]. They can faithfully reproduce their data with Monte Carlo simulations, resulting in fitting parameters for the total capacitance  $C_T = 4.6$  aF and induced charge of  $\Delta Q_0 = 0.03e$  [133]. If we convert this to a change in work function, we obtain  $\Delta\mu = 1.0$  meV. Clearly, the Magneto-Coulomb effect as described by equation (8.1) does not apply to these two experiments. The quantitative difference between experiment and theory suggests a stronger change in work function than theory predicts, which may be caused by anisotropic density of states in the ferromagnet.

Recently there have been reports of spin-orbit induced tunneling anisotropic magnetoresistance caused by a single Fe [134] and a single Co [135] contact. Anisotropic magnetoresistance in ferromagnetic metals stems from spin-orbit interaction, which mixes the conductive s-bands with the exchange-split d-bands. Free particle-like s-states determine the transport properties of a metal. The density of states of the d-bands depends on the direction of the magnetization. Therefore spin-orbit induced scattering of electrons from conductive s-states into localized d-states increases the resistivity of the metal. A magnetization switch can thus affect the conductivity by changing the density of states of the d-bands. Analogously, in tunnel devices with a ferromagnetic contact the density of states can be anisotropic and depend on the direction of the magnetization. The anisotropy can be sensed by electrons tunneling into or from the ferromagnet. It is also present in our F-InP junctions, where the deposited CoFe electrodes are wrapped around the InP nanowire, resulting in a locally very strong shape anisotropy. Since each contact is different on a microscopic scale, there will be a wide variety in anisotropy of all electrode shapes. Unfortunately, at the moment of writing we can no longer carry out measurements at other magnetic field orientations to check the anisotropy. The anisotropic density of states can play a significant role in our devices. It may for example add a significant contribution to the change in work function, and thus confirm the values we found. A calculation of this contribution is not feasible since the evaporated CoFe is polycrystalline: the dependence of density of states on the magnetization direction is not as straightforward as e.g. for single crystals [136].

In conclusion, we have reported the first observation of magnetoresistance in InP nanowires with CoFe and Ti/Pt contacts. The electric field control of sign

and magnitude of the magnetoresistance demonstrates a direct correlation with the transconductance. Also, the methods we use allow discrimination between effects induced by the contacts and spin transport phenomena. We observe the magnetoresistance when one of the ferromagnets is replaced by a non-magnetic metal, ruling out spin transport and proving that it is caused by a single ferromagnetic contact. We attribute the magnetoresistance to the Magneto-Coulomb effect, where a magnetically induced change in its work function alters the electric field experienced by the InP nanowire and hence the total device resistance. Our results emphasize the importance of making the distinction between different effects with the exact same signature to avoid ambiguous interpretations of magnetoresistance measurements.

We thank G. E. W. Bauer, A. J. S. Bernand-Mantel, J. A. van Dam, D. Loss, G. A. Steele and B. J. van Wees for discussions.



# Bibliography

- [1] A. Einstein, “Über einen die Erzeugung und Verwandlung des Lichtes betreffenden heuristischen Gesichtspunkt,” *Annalen der Physik*, vol. 17, pp. 132–148, 1905.
- [2] For more information, see the International Technology Roadmap for Semiconductors at <http://public.itrs.net>.
- [3] G. A. Prinz, “Magnetoelectronics,” *Science*, vol. 282, pp. 1660–1663, 1998.
- [4] S. A. Wolf, D. D. Awschalom, R. A. Buhrman, J. M. Daughton, S. von Molnar, M. L. Roukes, A. Y. Chtchelkanova, and D. M. Treger, “Spintronics: A Spin-Based Electronics Vision for the Future,” 2001.
- [5] I. Zutic, J. Fabian, and S. D. Sarma, “Spintronics: Fundamentals and applications,” *Reviews of Modern Physics*, vol. 76, 2004.
- [6] P. W. Shor, “Algorithms for Quantum Computation: Discrete Logarithms and Factoring,” *IEEE Symposium on Foundations of Computer Science*, pp. 124–134, 1994.
- [7] G. K. Brennen, C. M. Caves, P. S. Jessen, and I. H. Deutsch, “Quantum Logic Gates in Optical Lattices,” *Physical Review Letters*, vol. 82, no. 5, pp. 1060–1063, 1999.
- [8] J. I. Cirac and P. Zoller, “Quantum Computations with Cold Trapped Ions,” *Physical Review Letters*, vol. 74, no. 20, pp. 4091–4094, 1995.
- [9] J. E. Mooij, T. P. Orlando, L. Levitov, L. Tian, C. H. van der Wal, and S. Lloyd, “Josephson Persistent-Current Qubit,” *Science*, vol. 285, 1999.
- [10] D. Loss and D. P. DiVincenzo, “Quantum computation with quantum dots,” *Physical Review A*, vol. 57, no. 1, pp. 120–126, 1998.
- [11] B. E. Kane, “A silicon-based nuclear spin quantum computer,” *Nature*, vol. 393, no. 6681, pp. 133–137, 1998.

- [12] J. R. Petta, A. C. Johnson, J. M. Taylor, E. A. Laird, A. Yacoby, M. D. Lukin, C. M. Marcus, M. P. Hanson, and A. C. Gossard, “Coherent Manipulation of Coupled Electron Spins in Semiconductor Quantum Dots,” *Science*, vol. 309, pp. 2180–2184, 2005.
- [13] F. H. L. Koppens, C. Buizert, K. J. Tielrooij, I. T. Vink, K. C. Nowack, T. A. Y. Meunier, L. P. Kouwenhoven, and L. M. K. Vandersypen, “Driven coherent oscillations of a single electron spin in a quantum dot,” *Nature*, vol. 442, pp. 766–771, 2006.
- [14] I. Appelbaum, B. Huang, and D. J. Monsma, “Electronic measurement and control of spin transport in silicon,” *Nature*, vol. 447, pp. 295–8, 2007.
- [15] B. Huang, D. J. Monsma, and I. Appelbaum, “Coherent spin transport through an entire silicon wafer,” *Arxiv preprint arXiv:0706.0866*, 2007.
- [16] C. M. Lieber and Z. L. Wang, “Functional nanowires,” *MRS Bull*, vol. 32, no. 2, pp. 99–108, 2007.
- [17] P. Yang *MRS Bull*, vol. 30, p. 85, 2005.
- [18] L. Samuelson *et al.*, “Semiconductor nanowires for 0D and 1D physics and applications,” *Physica E*, vol. 25, 2004.
- [19] L. P. Kouwenhoven, D. G. Austing, and S. Tarucha, “Few-electron quantum dots,” *Reports on Progress in Physics*, vol. 64, no. 6, pp. 701–736, 2001.
- [20] R. Hanson, *Electron spins in Semiconductor Quantum Dots*. PhD thesis, 2005.
- [21] L. P. Kouwenhoven, C. M. Marcus, P. L. McEuen, S. Tarucha, R. M. Westervelt, and N. S. Wingreen, “Mesoscopic Electron Transport,” *NATO ASI Series E: Applied Sciences*, vol. 345, 1997.
- [22] J. A. van Dam, *Quantum transport in semiconductor nanowires*. PhD thesis, 2006.
- [23] R. S. Wagner and W. C. Ellis, “Vapor-Liquid Mechanism of Single Crystal Growth,” *Applied Physics Letters*, vol. 4, pp. 89–90, 1964.
- [24] A. M. Morales and C. M. Lieber, “A Laser Ablation Method for the Synthesis of Crystalline Semiconductor Nanowires,” *Science*, vol. 279, no. 5348, p. 208, 1998.

## BIBLIOGRAPHY

---

- [25] K. Hiruma, M. Yazawa, T. Katsuyama, K. Ogawa, K. Haraguchi, M. Koguchi, and H. Kakibayashi, “Growth and optical properties of nanometer-scale GaAs and InAs whiskers,” *Journal of Applied Physics*, vol. 77, p. 447, 1995.
- [26] Y. Wu, Y. Cui, L. Huynh, C. J. Barrelet, D. C. Bell, and C. M. Lieber, “Controlled growth and structures of molecular-scale silicon nanowires,” *Nano Lett*, vol. 4, no. 3, pp. 433–436, 2004.
- [27] M. S. Gudixsen, J. Wang, and C. M. Lieber, “Synthetic control of the diameter and length of single crystal semiconductor nanowires,” *J. Phys. Chem. B*, vol. 105, no. 19, p. 4062, 2001.
- [28] S. M. Sze, *Physics of semiconductor devices*. Wiley New York, 1985.
- [29] J. H. Davies, *The Physics of Low-dimensional Semiconductors: An Introduction*. Cambridge University Press, 1998.
- [30] M. A. Green, “Intrinsic concentration, effective densities of states, and effective mass in silicon,” *Journal of Applied Physics*, vol. 67, p. 2944, 1990.
- [31] P. Lautenschlager, P. B. Allen, and M. Cardona, “Phonon-induced lifetime broadenings of electronic states and critical points in Si and Ge,” *Physical Review B*, vol. 33, no. 8, pp. 5501–5511, 1986.
- [32] G. G. Macfarlane, T. P. McLean, J. E. Quarrington, and V. Roberts, “Fine Structure in the Absorption-Edge Spectrum of Si,” *Physical Review*, vol. 111, no. 5, pp. 1245–1254, 1958.
- [33] R. Hull, *Properties of Crystalline Silicon*. INSPEC, 1999.
- [34] F. L. Madarasz, J. E. Lang, and P. M. Hemeger, “Effective masses for nonparabolic bands in p-type silicon,” *Journal of Applied Physics*, vol. 52, no. 7, pp. 4646–4648, 1981.
- [35] J. E. Lang, F. L. Madarasz, and P. M. Hemenger, “Temperature dependent density of states effective mass in nonparabolic p-type silicon,” *Journal of Applied Physics*, vol. 54, no. 6, p. 3612, 1983.
- [36] L. L. Sohn, L. P. Kouwenhoven, and G. Schön, *Mesoscopic Electron Transport*. Kluwer Academic, 1997.
- [37] C. Kittel, “Introduction to Solid State Physics,” 1996.

- [38] B. Van Zeghbroeck, “Principles of Semiconductor Devices, 2004,” *unpublished*, see <http://ece-www.colorado.edu/~bart/book>.
- [39] O. F. Sankey, R. E. Allen, S. F. Ren, and J. D. Dow, “Dangling bonds and Schottky barriers,” *Journal of Vacuum Science & Technology B: Microelectronics and Nanometer Structures*, vol. 3, no. 4, pp. 1162–1166, 1985.
- [40] Y. M. Niquet, A. Lherbier, N. H. Quang, M. V. Fernández-Serra, X. Blase, and C. Delerue, “Electronic structure of semiconductor nanowires,” *Physical Review B*, vol. 73, no. 16, 2006.
- [41] A. K. Buin, A. Verma, A. Svizhenko, and M. P. Anantram, “Significant Enhancement of Hole Mobility in [110] Silicon Nanowires Compared to Electrons and Bulk Silicon,” *Nano Lett*, vol. 8, no. 2, pp. 760–765, 2008.
- [42] K. K. Lew, L. Pan, T. E. Bogart, S. M. Dilts, E. C. Dickey, J. M. Redwing, Y. Wang, M. Cabassi, T. S. Mayer, and S. W. Novak, “Structural and electrical properties of trimethylboron-doped silicon nanowires,” *Applied Physics Letters*, vol. 85, p. 3101, 2004.
- [43] A. A. van Loon, “Creating quantum dots in silicon nanowires,” Master’s thesis, 2006.
- [44] F. V. Mikulec, M. Kuno, M. Bennati, D. A. Hall, R. G. Griffin, and M. G. Bawendi, “Organometallic synthesis and spectroscopic characterization of manganese-doped CdSe nanocrystals,” *J. Amer. Chem. Soc.*, vol. 122, no. 11, pp. 2532–2540, 2000.
- [45] Z. Zhong, Y. Fang, W. Lu, and C. M. Lieber, “Coherent Single Charge Transport in Molecular-Scale Silicon Nanowires,” *Nano Lett*, vol. 5, no. 6, pp. 1143–1146, 2005.
- [46] D. Shir, B. Z. Liu, A. M. Mohammad, K. K. Lew, and S. E. Mohny, “Oxidation of silicon nanowires,” *Journal of Vacuum Science & Technology B: Microelectronics and Nanometer Structures*, vol. 24, p. 1333, 2006.
- [47] Y. Cui and C. M. Lieber, “Functional Nanoscale Electronic Devices Assembled Using Silicon Nanowire Building Blocks,” 2001.
- [48] Y. Cui, X. Duan, J. Hu, and C. M. Lieber, “Doping and electrical transport in silicon nanowires,” *J. Phys. Chem. B*, vol. 104, pp. 5213–5216, 2000.

## BIBLIOGRAPHY

---

- [49] C. Niu, V. Sahi, J. Chen, J. W. Parce, S. Empedocles, and J. L. Goldman, “High-performance thin-film transistors using semiconductor nanowires and nanoribbons,” *Nature*, vol. 425, pp. 274–278, 2003.
- [50] S. W. Chung, J. Y. Yu, and J. R. Heath, “Silicon nanowire devices,” *Applied Physics Letters*, vol. 76, p. 2068, 2000.
- [51] Y. Cui, Z. Zhong, D. Wang, W. U. Wang, and C. M. Lieber, “High performance silicon nanowire field effect transistors,” *Nano Lett*, vol. 3, no. 2, pp. 149–152, 2003.
- [52] S. Jin, D. Whang, M. C. McAlpine, R. S. Friedman, Y. Wu, and C. M. Lieber, “Scalable Interconnection and Integration of Nanowire Devices without Registration,” *Nano Letters*, vol. 4, no. 5, pp. 915–919, 2004.
- [53] J. Goldberger, A. I. Hochbaum, R. Fan, and P. Yang, “Silicon vertically integrated nanowire field effect transistors,” *Nano Lett*, vol. 6, no. 5, 2006.
- [54] G. Zheng, W. Lu, S. Jin, and C. M. Lieber, “Synthesis and Fabrication of High-Performance n-Type Silicon Nanowire Transistors,” *Advanced Materials*, vol. 16, no. 21, pp. 1890–1893, 2004.
- [55] F. Simmel, D. Abusch-Magder, D. A. Wharam, M. A. Kastner, and J. P. Kotthaus, “Statistics of the Coulomb-blockade peak spacings of a silicon quantum dot,” *Physical Review B*, vol. 59, no. 16, pp. 10441–10444, 1999.
- [56] G. M. Jones, B. H. Hu, C. H. Yang, M. J. Yang, R. Hajdaj, and G. Heheine, “Enhancement-mode metal-oxide-semiconductor single-electron transistor on pure silicon,” *Applied Physics Letters*, vol. 89, p. 073106, 2006.
- [57] A. Fujiwara, H. Inokawa, K. Yamazaki, H. Namatsu, Y. Takahashi, N. M. Zimmerman, and S. B. Martin, “Single electron tunneling transistor with tunable barriers using silicon nanowire metal-oxide-semiconductor field-effect transistor,” *Applied Physics Letters*, vol. 88, p. 053121, 2006.
- [58] M. Hofheinz, X. Jehl, M. Sanquer, G. Molas, M. Vinet, and S. Deleonibus, “Simple and controlled single electron transistor based on doping modulation in silicon nanowires,” *Applied Physics Letters*, vol. 89, no. 14, 2006.
- [59] L. P. Rokhinson, L. J. Guo, S. Y. Chou, and D. C. Tsui, “Spin transitions in a small Si quantum dot,” *Physical Review B*, vol. 63, p. 35321, 2001.

- [60] E. G. Emiroglu, D. G. Hasko, and D. A. Williams, “Isolated double quantum dot capacitively coupled to a single quantum dot single-electron transistor in silicon,” *Applied Physics Letters*, vol. 83, p. 3942, 2003.
- [61] M. R. Sakr, H. W. Jiang, E. Yablonovitch, and E. T. Croke, “Fabrication and characterization of electrostatic Si/SiGe quantum dots with an integrated read-out channel,” *Applied Physics Letters*, vol. 87, 2005.
- [62] L. J. Klein, D. E. Savage, and M. A. Eriksson, “Coulomb blockade and Kondo effect in a few-electron silicon/silicon-germanium quantum dot,” *Applied Physics Letters*, vol. 90, p. 033103, 2007.
- [63] S. J. Angus, A. J. Ferguson, A. S. Dzurak, and R. G. Clark, “Gate-Defined Quantum Dots in Intrinsic Silicon,” *Nano Lett*, vol. 7, no. 7, p. 2051, 2007.
- [64] H. Liu, T. Fujisawa, H. Inokawa, Y. Ono, A. Fujiwara, and Y. Hirayama, “A gate-defined silicon quantum dot molecule,” *Applied Physics Letters*, vol. 92, no. 22, 2008.
- [65] N. Shaji, C. B. Simmons, M. Thalakulam, L. J. Klein, H. Qin, H. Luo, D. E. Savage, M. G. Lagally, A. J. Rimberg, R. Joynt, M. Friesen, R. H. Blick, S. N. Coppersmith, and M. A. Eriksson, “Spin blockade and lifetime-enhanced transport in a few-electron Si/SiGe double quantum dot,” *Nature Physics*, no. 4, pp. 540–544, 2008.
- [66] C. E. W. M. van Rijmenam, “Spin filling in a few-hole silicon nanowire quantum dot,” Master’s thesis, 2007.
- [67] Y. Wu, J. Xiang, C. Yang, W. Lu, and C. M. Lieber, “Single-crystal metallic nanowires and metal/semiconductor nanowire heterostructures,” *Nature*, vol. 430, no. 6995, pp. 61–65, 2004.
- [68] B. Meyer, U. Gottlieb, O. Laborde, H. Yang, J. C. Lasjaunias, A. Sulpice, and R. Madar, “Intrinsic properties of NiSi,” *Journal of alloys and compounds*, vol. 262, pp. 235–237, 1997.
- [69] R. Hanson, L. P. Kouwenhoven, J. R. Petta, S. Tarucha, and L. M. K. Vandersypen, “Spins in few-electron quantum dots,” *Reviews of Modern Physics*, vol. 79, no. 4, pp. 1217–1265, 2007.
- [70] R. Martel, T. Schmidt, H. R. Shea, T. Hertel, and P. Avouris, “Single- and multi-wall carbon nanotube field-effect transistors,” *Applied Physics Letters*, vol. 73, p. 2447, 1998.

## BIBLIOGRAPHY

---

- [71] T. Balder, “Modeling Quantum Dots in Realistic Carbon Nanotube Devices,” Master’s thesis, 2008.
- [72] P. D. Jarillo-Herrero, S. Sapmaz, C. Dekker, L. P. Kouwenhoven, and H. S. J. van der Zant, “Electron-hole symmetry in a semiconducting carbon nanotube quantum dot,” *Nature*, vol. 429, pp. 389–392, 2004.
- [73] F. Kuemmeth, S. Ilani, D. C. Ralph, and P. L. McEuen, “Coupling of Spin and Orbital Motion of Electrons in Carbon Nanotubes,” *Nature*, vol. 452, pp. 448–452, 2008.
- [74] H. Sellier, G. P. Lansbergen, J. Caro, S. Rogge, N. Collaert, I. Ferain, M. Jurczak, and S. Biesemans, “Transport Spectroscopy of a Single Dopant in a Gated Silicon Nanowire,” *Physical Review Letters*, vol. 97, no. 20, p. 206805, 2006.
- [75] Y. Hu, J. Xiang, G. Liang, H. Yan, and C. M. Lieber, “Sub-100 Nanometer Channel Length Ge/Si Nanowire Transistors with Potential for 2 THz Switching Speed,” *Nano Lett*, vol. 8, no. 3, pp. 925–930, 2008.
- [76] W. M. Weber, L. Geelhaar, A. P. Graham, E. Unger, G. S. Duesberg, M. Liebau, W. Pamler, C. Chèze, H. Riechert, P. Lugli, and F. Kreupl, “Silicon-nanowire transistors with intruded nickel-silicide contacts,” *Nano Lett*, vol. 6, no. 12, pp. 2660–2666, 2006.
- [77] A. V. Danilov, D. S. Golubev, and S. E. Kubatkin, “Tunneling through a multigrain system: Deducing sample topology from nonlinear conductance,” *Physical Review B*, vol. 65, no. 12, p. 125312, 2002.
- [78] P. W. Leu, B. Shan, and K. Cho, “Surface chemical control of the electronic structure of silicon nanowires: Density functional calculations,” *Physical Review B*, vol. 73, no. 19, p. 195320, 2006.
- [79] P. B. Sorokin, P. V. Avramov, A. G. Kvashnin, D. G. Kvashnin, S. G. Ovchinnikov, and A. S. Fedorov, “Density functional study of [110]-oriented thin silicon nanowires,” *Physical Review B*, vol. 77, p. 235417, 2008.
- [80] W. G. van der Wiel, S. De Franceschi, J. M. Elzerman, T. Fujisawa, S. Tarucha, and L. P. Kouwenhoven, “Electron transport through double quantum dots,” *Reviews of Modern Physics*, vol. 75, no. 1, pp. 1–22, 2002.
- [81] D. H. Cobden, M. Bockrath, P. L. McEuen, A. G. Rinzler, and R. E. Smalley, “Spin Splitting and Even-Odd Effects in Carbon Nanotubes,” *Physical Review Letters*, vol. 81, pp. 681–684, 1998.

- 
- [82] D. H. Cobden and J. Nygård, “Shell Filling in Closed Single-Wall Carbon Nanotube Quantum Dots,” *Physical Review Letters*, vol. 89, p. 46803, 2002.
- [83] L. H. Willems van Beveren, R. Hanson, I. T. Vink, F. H. L. Koppens, L. P. Kouwenhoven, and L. M. K. Vandersypen, “Spin filling of a quantum dot derived from excited-state spectroscopy,” *New Journal of Physics*, vol. 7, 2005.
- [84] L. P. Kouwenhoven, T. H. Oosterkamp, M. W. Danoesastro, M. Eto, D. G. Austing, T. Honda, and S. Tarucha, “Excitation Spectra of Circular, Few-Electron Quantum Dots,” *Science*, vol. 278, no. 5344, p. 1788, 1997.
- [85] T. Kita, D. Chiba, Y. Ohno, and H. Ohno, “A few-electron vertical InGaAs quantum dot with an insulating gate,” *Applied Physics Letters*, vol. 91, p. 232101, 2007.
- [86] D. M. Zumbühl, C. M. Marcus, M. P. Hanson, and A. C. Gossard, “Co-tunneling Spectroscopy in Few-Electron Quantum Dots,” *Physical Review Letters*, vol. 93, no. 25, p. 256801, 2004.
- [87] M. T. Björk, C. Thelander, A. E. Hansen, L. E. Jensen, M. W. Larsson, L. R. Wallenberg, and L. Samuelson, “Few-Electron Quantum Dots in Nanowires,” *Nano Lett*, vol. 4, pp. 1621–1625, 2004.
- [88] M. T. Björk, A. Fuhrer, A. E. Hansen, M. W. Larsson, L. E. Fröberg, and L. Samuelson, “Tunable effective g factor in InAs nanowire quantum dots,” *Physical Review B*, vol. 72, no. 20, p. 201307, 2005.
- [89] C. Fasth, A. Fuhrer, L. Samuelson, V. N. Golovach, and D. Loss, “Direct Measurement of the Spin-Orbit Interaction in a Two-Electron InAs Nanowire Quantum Dot,” *Physical Review Letters*, vol. 98, 2007.
- [90] W. R. L. Lambrecht, N. E. Christensen, and P. Blöchl, “Electronic structure and properties of NiSi<sub>2</sub> and CoSi<sub>2</sub> in the fluorite and adamantane structures,” *Physical Review B*, vol. 36, no. 5, pp. 2493–2503, 1987.
- [91] J. von Delft and D. C. Ralph, “Spectroscopy of discrete energy levels in ultrasmall metallic grains,” *Physics Reports*, vol. 345, pp. 61–173, 2001.
- [92] H. Grabert and M. H. Devoret, *Single charge tunneling*. 1992.
- [93] S. Braig and K. Flensberg, “Vibrational sidebands and dissipative tunneling in molecular transistors,” *Physical Review B*, vol. 68, p. 205324, 2003.

## BIBLIOGRAPHY

---

- [94] C. M. Lieber *MRS Bull*, vol. 28, p. 486, 2003.
- [95] S. De Franceschi, J. A. van Dam, E. P. A. M. Bakkers, L. F. Feiner, L. Gurevich, and L. P. Kouwenhoven, “Single-electron tunneling in InP nanowires,” *Applied Physics Letters*, vol. 83, no. 2, 2003.
- [96] M. T. Björk, C. Thelander, A. E. Hansen, L. E. Jensen, M. W. Larsson, L. R. Wallenberg, and L. Samuelson, “Few-Electron Quantum Dots in Nanowires,” *Nano Lett*, vol. 4, pp. 1621–1625, 2004.
- [97] J. Xiang, W. Lu, Y. Hu, Y. Wu, H. Yan, and C. M. Lieber, “Ge/Si nanowire heterostructures as high-performance field-effect transistors,” *Nature*, vol. 441, no. 7092, pp. 489–493, 2006.
- [98] Y. J. Doh, J. A. van Dam, A. L. Roest, E. P. A. M. Bakkers, L. P. Kouwenhoven, and S. De Franceschi, “Tunable Supercurrent Through Semiconductor Nanowires,” 2005.
- [99] J. Xiang, A. Vidan, M. Tinkham, R. M. Westervelt, and C. M. Lieber, “Ge/Si nanowire mesoscopic Josephson junctions,” *Nature Nanotechnology*, vol. 1, no. 3, pp. 208–213, 2006.
- [100] M. A. Topinka, R. M. Westervelt, and E. J. Heller, “Imaging Electron Flow,” *Physics Today*, vol. 56, no. 12, pp. 47–52, 2003.
- [101] M. T. Woodside and P. L. McEuen, “Scanned Probe Imaging of Single-Electron Charge States in Nanotube Quantum Dots,” 2002.
- [102] P. Fallahi, A. C. Bleszynski, R. M. Westervelt, J. Huang, J. D. Walls, E. J. Heller, M. Hanson, and A. C. Gossard, “Imaging a single-electron quantum dot,” *Nano Lett*, vol. 5, no. 2, pp. 223–6, 2005.
- [103] A. Pioda *et al.*, “Spatially Resolved Manipulation of Single Electrons in Quantum Dots Using a Scanned Probe,” *Physical Review Letters*, vol. 93, no. 21, p. 216801, 2004.
- [104] M. Bockrath, W. Liang, D. Bozovic, J. H. Hafner, C. M. Lieber, M. Tinkham, and H. Park, “Resonant Electron Scattering by Defects in Single-Walled Carbon Nanotubes,” 2001.
- [105] S. J. Tans and C. Dekker, “Molecular transistors: Potential modulations along carbon nanotubes,” *Nature*, vol. 404, no. 6780, pp. 834–835, 2000.

- [106] N. B. Zhitenev, T. Fulton, A. Yacoby, H. F. Hess, L. N. Pfeiffer, and K. W. West, “Imaging of localized electronic states in the quantum Hall regime,” *Nature*, vol. 404, no. 6777, pp. 473–476, 2000.
- [107] Y. Ahn, J. Dunning, and J. Park, “Scanning photocurrent imaging and electronic band studies in silicon nanowire field effect transistors,” *Nano Lett*, vol. 5, no. 7, pp. 1367–70, 2005.
- [108] Y. Gu, E. S. Kwak, J. L. Lensch, J. E. Allen, T. W. Odom, and L. J. Lauhon, “Near-field scanning photocurrent microscopy of a nanowire photodetector,” *Applied Physics Letters*, vol. 87, p. 043111, 2005.
- [109] E. P. A. M. Bakkers, J. A. van Dam, S. De Franceschi, L. P. Kouwenhoven, M. Kaiser, M. Verheijen, H. Wondergem, and P. van der Sluis, “Epitaxial growth of InP nanowires on germanium,” *Nature Materials*, vol. 3, 2004.
- [110] F. R. Waugh, M. J. Berry, D. J. Mar, R. M. Westervelt, K. L. Campman, and A. C. Gossard, “Single-Electron Charging in Double and Triple Quantum Dots with Tunable Coupling,” *Physical Review Letters*, vol. 75, no. 4, pp. 705–708, 1995.
- [111] I. M. Ruzin, V. Chandrasekhar, E. I. Levin, and L. I. Glazman, “Stochastic Coulomb blockade in a double-dot system,” *Physical Review B*, vol. 45, no. 23, pp. 13469–13478, 1992.
- [112] Z. Yao, C. Dekker, and P. Avouris, “Electrical Transport Through Single-Wall Carbon Nanotubes,” *Topics in Applied Physics*, vol. 80, 2001.
- [113] M. N. Baibich, J. M. Broto, A. Fert, F. N. Van Dau, F. Petroff, P. Eitenne, G. Creuzet, A. Friederich, and J. Chazelas, “Giant Magnetoresistance of (001) Fe/(001) Cr Magnetic Superlattices,” *Physical Review Letters*, vol. 61, no. 21, pp. 2472–2475, 1988.
- [114] G. Binasch, P. Grünberg, F. Saurenbach, and W. Zinn, “Enhanced magnetoresistance in layered magnetic structures with antiferromagnetic interlayer exchange,” *Physical Review B*, vol. 39, no. 7, pp. 4828–4830, 1989.
- [115] S. Datta and B. Das, “Electronic analog of the electro-optic modulator,” *Applied Physics Letters*, vol. 56, p. 665, 1990.
- [116] K. Tsukagoshi, B. W. Alphenaar, and H. Ago, “Coherent transport of electron spin in a ferromagnetically contacted carbon nanotube,” *Nature*, vol. 401, pp. 572–574, 1999.

## BIBLIOGRAPHY

---

- [117] D. Orgassa, G. J. Mankey, and H. Fujiwara, “Spin injection into carbon nanotubes and a possible application in spin-resolved scanning tunnelling microscopy,” *Nanotechnology*, vol. 12, no. 3, pp. 281–284, 2001.
- [118] B. Zhao, I. Mönch, H. Vinzelberg, T. Mühl, and C. Schneider, “Spin-coherent transport in ferromagnetically contacted carbon nanotubes,” *Applied Physics Letters*, vol. 80, p. 3144, 2002.
- [119] J. R. Kim, H. M. So, J. J. Kim, and J. Kim, “Spin-dependent transport properties in a single-walled carbon nanotube with mesoscopic Co contacts,” *Physical Review B*, vol. 66, no. 23, p. 233401, 2002.
- [120] A. Jensen, J. R. Hauptmann, J. Nygård, and P. E. Lindelof, “Magnetoresistance in ferromagnetically contacted single-wall carbon nanotubes,” *Physical Review B*, vol. 72, no. 3, p. 35419, 2005.
- [121] S. Sahoo, T. Kontos, J. Furer, C. Hoffmann, M. Gräber, A. Cottet, and C. Schönenberger, “Electric field control of spin transport,” *Nature Physics*, vol. 1, pp. 99–102, 2005.
- [122] H. T. Man, I. J. W. Wever, and A. F. Morpurgo, “Spin-dependent quantum interference in single-wall carbon nanotubes with ferromagnetic contacts,” *Physical Review B*, vol. 73, no. 24, p. 241401, 2006.
- [123] S. J. van der Molen, N. Tombros, and B. J. van Wees, “Magneto-Coulomb effect in spin-valve devices,” *Physical Review B*, vol. 73, p. 220406, 2006.
- [124] K. Ono, H. Shimada, and Y. Ootuka, “Enhanced Magnetic Valve Effect and Magneto-Coulomb Oscillations in Ferromagnetic Single Electron Transistor,” *Journal of the Physical Society of Japan*, vol. 66, p. 1261, 1997.
- [125] H. Shimada, K. Ono, and Y. Ootuka, “Magneto-Coulomb Oscillation in Ferromagnetic Single Electron Transistors,” *Journal of the Physical Society of Japan*, vol. 67, p. 1359, 1998.
- [126] M. Johnson and R. H. Silsbee, “Interfacial charge-spin coupling: Injection and detection of spin magnetization in metals,” *Physical Review Letters*, vol. 55, no. 17, pp. 1790–1793, 1985.
- [127] F. J. Jedema, H. B. Heersche, A. T. Filip, J. J. A. Baselmans, and B. J. van Wees, “Electrical detection of spin precession in a metallic mesoscopic spin valve,” *Nature*, vol. 416, pp. 713–716, 2002.

- [128] N. Tombros, S. J. van der Molen, and B. J. van Wees, “Separating spin and charge transport in single-wall carbon nanotubes,” *Physical Review B*, vol. 73, no. 23, p. 233403, 2006.
- [129] X. Lou, C. Adelman, S. A. Crooker, E. S. Garlid, J. Zhang, S. M. Reddy, S. D. Flexner, C. J. Palmstrom, and P. A. Crowell, “Electrical detection of spin transport in lateral ferromagnet–semiconductor devices,” *Nature Physics*, vol. 3, pp. 197–202, 2007.
- [130] N. Tombros, C. Jozsa, M. Popinciuc, H. T. Jonkman, and B. J. van Wees, “Electronic spin transport and spin precession in single graphene layers at room temperature,” *Nature*, vol. 448, pp. 571–574, 2007.
- [131] S. De Franceschi, J. A. van Dam, E. P. A. M. Bakkers, L. F. Feiner, L. Gurevich, and L. P. Kouwenhoven, “Single-electron tunneling in InP nanowires,” *Applied Physics Letters*, vol. 83, no. 2, 2003.
- [132] A. Bernand-Mantel, P. Seneor, N. Lidgi, M. Muñoz, V. Cros, S. Fusil, K. Bouzehouane, C. Deranlot, A. Vaures, F. Petroff, and A. Fert, “Evidence for spin injection in a single metallic nanoparticle: A step towards nanospintronics,” *Applied Physics Letters*, vol. 89, p. 062502, 2006.
- [133] A. Bernand-Mantel *Private communication*.
- [134] J. Moser, A. Matos-Abiague, D. Schuh, W. Wegscheider, J. Fabian, and D. Weiss, “Tunneling Anisotropic Magnetoresistance and Spin-Orbit Coupling in Fe/GaAs/Au Tunnel Junctions,” *Physical Review Letters*, vol. 99, no. 5, p. 56601, 2007.
- [135] R. S. Liu, L. Michalak, C. M. Canali, L. Samuelson, and H. Pettersson, “Tunneling Anisotropic Magnetoresistance in Co/AlO<sub>x</sub>/Au Tunnel Junctions,” *Nano Lett*, vol. 8, no. 3, pp. 848–852, 2008.
- [136] M. Bode, S. Heinze, A. Kubetzka, O. Pietzsch, X. Nie, G. Bihlmayer, S. Blügel, and R. Wiesendanger, “Magnetization-Direction-Dependent Local Electronic Structure Probed by Scanning Tunneling Spectroscopy,” *Physical Review Letters*, vol. 89, no. 23, p. 237205, 2002.

# Summary

## Spin and Charge in Semiconductor nanowires

The operation of computer processors and data storage devices relies on the spin and charge of a macroscopic number of electrons. Spin is a magnetic moment, that points either parallel to an applied magnetic field (spin-up) or anti-parallel to the field (spin-down). Quantum mechanics describes the spin as being in both states at the same time, a superposition of spin-up and spin-down. This quantum property of spin manifests itself when we consider a single electron, but is no longer observable when a large number of spins is involved.

The field of spintronics tries to exploit the latter to realize novel spintronic devices that exceed modern-day silicon integrated-circuit technology in terms of data processing speed, power consumption, non-volatility and integration densities. A single spin can be used as a building block of a quantum computer, where the spin-up and spin-down states form the logical 0 and 1 of the quantum bit, or qubit. A future quantum computer should be able to carry out a certain class of computations that are not possible classically. This thesis describes a series of experiments aimed at a better understanding of spin and charge effects in semiconductor nanowires, with both spintronics and quantum computation as future applications.

The research in this thesis is motivated by an interest in quantum physics and by the prospect of new applications based on the spin of electrons or holes. This work focuses on confining single spins in quantum dots, which can serve as building blocks of a future quantum computer. Long spin lifetimes are crucial to carry out quantum operations on spin qubits.

We report a number of important steps towards the creation of spin qubits in a material with an expected long spin lifetime: the demonstration of single quantum dots in silicon (Si) nanowires, the isolation of a single hole in a Si quantum dot, energy and magnetic field spectroscopy of the first four spin states, and the use of a scanning probe microscope to locate quantum dots inside indium arsenide (InAs) nanowires. Additionally we try to make novel spintronic devices

using a macroscopic number of spins, by demonstrating electric field control of the magnetoresistance in indium phosphide (InP) nanowires. This way we show the ability to combine the functionalities of semiconductors and magnetic materials.

The versatility of semiconductor nanowires in terms of chemical composition, structure, size, and morphology promises a wide range of potential applications. The high degree of freedom in nanowire synthesis additionally allows growth of heterostructures in both the radial and longitudinal direction. It is essential for this work that a nanowire provides natural confinement of electrons and holes due to its small size, making it ideal to observe quantum effects. We use Si and InAs nanowires to create small islands with a controllable number of electrons. These quantum dots can exchange electrons with reservoirs via tunnel barriers. Additionally, the capacitive coupling to a gate electrode allows the number of electrons on the dot to be varied. If the dot size is small enough (typically  $< 50$  nm) it exhibits a discrete energy spectrum which can be observed if the thermal energy is smaller than level spacing between the quantum states.

We start with the experimental realization of single quantum dots in *p*-type silicon nanowires. We observe pronounced excited states in many devices with short channel lengths. Many single dots split up in two dots upon reaching the few-hole regime. We demonstrate control of the hole number down to one in very short dots ( $< 12$  nm). Detailed measurements at perpendicular magnetic fields reveal the Zeeman splitting of a single hole in silicon. We are able to determine the ground-state spin configuration for one to four holes occupying the dot and find a spin filling with alternating spin-down and spin-up holes, which is confirmed by magnetospectroscopy up to 9 Tesla.

An unusual feature in single-hole silicon nanowire quantum dots is analyzed. We observe transitions corresponding to additional energy levels *below* the  $N = 0$  ground-state energy of the dot, which cannot correspond to electronic or Zeeman states. The levels are quantized in multiples of 100–180  $\mu\text{eV}$  and independent of magnetic field. We explain the discrete energy spectrum as inelastic tunneling processes, where the excess energy is emitted to quantized states in the environment of the quantum dot. The most likely explanation for the excitations is acoustic phonon emission to a cavity between the two contacts to the nanowire.

Additionally we show how a scanning probe microscope can be used to find individual quantum dots inside InAs nanowires. A charged tip is used as a movable gate to image electron flow through InAs nanowires. Complex patterns of concentric rings in conductance plots reveal the presence of multiple quantum dots, formed by disorder. Rings of high conductance are centered on each quantum dot, corresponding to the addition or removal of electrons by the scanning probe.

---

Finally, we present electric field control of the magnetoresistance in InP nanowires with ferromagnetic contacts. The magnetoresistance is induced by the magnetization switch of a single ferromagnetic contact and persists at high bias. Since we still observe the magnetoresistance when one of the ferromagnets is replaced by a non-magnetic metal, it must be induced by a single ferromagnetic contact. The most likely origin is a magnetically induced change in the ferromagnetic work function, which alters the electric field experienced by the InP nanowire and hence the total device resistance.

Floris Zwanenburg  
August 2008



# Samenvatting

## Spin en lading in halfgeleidende nanodraden

De werking van computerprocessoren en harde schijven is gebaseerd op de spin en lading van elektronen. Spin is een magnetisch moment dat ofwel parallel staat aan een aangebracht magnetisch veld (spin-omhoog), ofwel anti-parallel aan dat veld (spin-omlaag). Quantummechanisch beschrijven we de spin alsof die in beide toestanden tegelijkertijd is, een superpositie van spin-omhoog en spin-omlaag. De quantummechanische aard van de spin komt naar boven als we kijken naar een enkel elektron, maar speelt geen rol meer in het geval van een groot aantal spins.

Het onderzoeksveld genaamd spintronica probeert een macroscopisch aantal spins te gebruiken om nieuwe schakelingen of apparaten te realiseren, die de huidige silicium IC-technologie overtreffen op het gebied van processorsnelheid, energieverbruik, duurzaam geheugen en integratiedichtheid. Een enkele spin kan gebruikt worden als bouwsteen van een quantum computer, waarbij de spin-omhoog en spin-omlaag toestanden de logische 1 en 0 vormen van het quantum bit, of qubit. Een quantum computer zou in staat zijn een bepaald type berekeningen uit te voeren die voor een klassieke computer onmogelijk zijn. Dit proefschrift beschrijft een reeks experimenten die tot doel hebben om het gedrag van spin en lading in halfgeleidende nanodraden beter te begrijpen, met als lange termijn toepassingen spintronica en een quantum computer.

De motivatie voor het onderzoek in dit proefschrift komt voort uit interesse in quantum fysica en het vooruitzicht op nieuwe toepassingen gebaseerd op de spin van elektronen of gaten. Dit werk richt zich op het opsluiten van enkele spins in quantum dots, die kunnen dienen als bouwstenen van een toekomstige quantum computer. Een lange levensduur van de spintoestand is cruciaal om quantum operaties uit te voeren op spin qubits.

We doen verslag van een aantal belangrijke stappen in de richting van het maken van spin qubits in een materiaal, waarvan men verwacht dat de spintoestand een lange levensduur heeft: de demonstratie van enkelvoudige quantum dots in silicium (Si) nanodraden, de isolatie van een enkel gat op een Si quantum

dot, energie en magnetisch veld spectroscopie van de eerste vier spintoestanden en het gebruik van een zogenaamde scanning probe microscoop om quantum dots in indiumarsenide (InAs) nanodraden te localiseren. Bovendien proberen we nieuwe spintronische schakelingen te ontwikkelen waarbij we gebruik maken van een macroscopisch aantal spins. De demonstratie van controle over de magnetoweerstand in indiumfosfide (InP) nanodraden met behulp van een elektrisch veld laat zien dat we de functionaliteiten van halfgeleiders en magnetische materialen kunnen combineren.

De veelzijdigheid van halfgeleidende nanodraden wat betreft de scheikundige samenstelling, structuur, afmetingen en vorm beloven een breed spectrum aan mogelijke toepassingen. De grote vrijheidsgraad in de synthese van nanodraden maakt het mogelijk om heterostructuren te maken, zowel in de radiële richting als de lengterichting. Voor dit werk is het essentieel dat een nanodraad door zijn kleine afmetingen van nature zorgt voor insluiting van elektronen en gaten, ideaal voor de waarneming van quantum effecten. We gebruiken Si en InAs nanodraden om kleine eilanden te creëren met een controleerbaar aantal elektronen. Deze quantum dots kunnen via tunnelbarrières elektronen uitwisselen met reservoirs. Bovendien zorgt de capacitieve koppeling met een gate elektrode ervoor dat het aantal elektronen op de dot kan worden gevarieerd. Als de dot klein genoeg is (typisch  $< 50$  nm) vertoont hij een discreet energiespectrum dat waargenomen kan worden als de thermische energie kleiner is dan de afstand tussen de niveaus van de quantum toestanden.

We beginnen met de experimentele realisatie van enkelvoudige quantum dots in *p*-type silicium nanodraden. We nemen geprononceerde aangeslagen toestanden waar in een groot aantal quantum dots van korte lengte. De meeste dots splitsen zich in tweeën wanneer er nog maar een paar gaten op zitten. We laten zien, dat we in zeer kleine dots ( $< 12$  nm) zelfs controle hebben tot één gat op de dot. Gedetailleerde metingen bij loodrechte magneetvelden onthullen de Zeeman-splitsing van een enkel gat in silicium. We zijn in staat om de grondtoestanden te bepalen van één tot vier gaten op de dot en we ontdekken dat de dot wordt gevuld met afwisselend spin-omlaag en spin-omhoog gaten. Dat wordt vervolgens bevestigd door magnetisch veld spectroscopie tot 9 Tesla.

We analyseren een eigenaardigheid in quantum dots in Si nanodraden waar slechts één gat op zit. We nemen transitie waar die overeenkomen met energieniveaus *onder* de energie van de  $N = 0$  grondtoestand van de dot, maar die geen elektronische of Zeemantoestanden kunnen zijn. De niveaus zijn gequantiseerd in veelvoud van  $100\text{--}180$   $\mu\text{eV}$  en onafhankelijk van magnetische velden. We leggen het discrete energiespectrum uit als gevolg van inelastische tunnel processen, waarbij de overtollige energie wordt uitgezonden naar gequantiseerde toestanden

---

in de omgeving van de quantum dot. De meest waarschijnlijke verklaring voor de excitaties is emissie van akoestische fononen naar een resonantieruimte tussen de twee contacten aan de nanodraad.

Daarnaast laten we zien hoe een scanning probe microscoop gebruikt kan worden om individuele quantum dots te localiseren in InAs nanodraden. Een opgeladen tip wordt gebruikt als een verplaatsbare gate elektrode om de elektronenstroom in InAs nanodraden in beeld te krijgen. Complexe patronen van concentrische ringen in geleidingsmetingen onthullen de aanwezigheid van meerdere quantum dots, die gevormd zijn door wanorde in de draad. Ringen van hoge geleiding zijn gecentreerd om iedere quantum dot en komen overeen met de toevoeging of verwijdering van elektronen door de scanning probe.

Tenslotte presenteren we controle over de magnetoweerstand in indiumfosfide nanodraden met behulp van een elektrisch veld. De magnetoweerstand wordt veroorzaakt door het omschakelen van de magnetisatie van een enkel ferromagnetisch contact en houdt aan bij hoge stroominstellingen. De meest waarschijnlijke verklaring is een magnetisch geïnduceerde verandering in de werkfunctie van de ferromagneet. Als bijgevolg verandert het effectieve elektrische veld dat de InP nanodraad voelt en daarmee de totale weerstand.

Floris Zwanenburg  
Augustus 2008



# Curriculum Vitae

Floris Arnoud Zwanenburg

- July 3, 1976    Born in Heerde, The Netherlands.
- 1988 – 1994    Grammar school, Gymnasium Celeanum, Zwolle.
- 1994 – 1995    English Language, Culture and Society Program,  
University of East Anglia, Norwich, UK.
- 1995 – 2003    MSc Applied Physics, Delft University of Technology.  
MSc thesis supervisor: prof. dr. ir. J. E. Mooij  
Subject: Superconducting electronics with phase-biased SQUIDs
- 1997 – 1998    Board member of the student association for Applied Physics.
- 2003            Internship at Marcus Lab, Harvard University, Cambridge, USA.  
Principal investigator: prof. dr. C. M. Marcus  
Subject: All-electrical spin injection and detection in silicon.
- 2003 – 2008    PhD research, Delft University of Technology  
under supervision of prof. dr. ir. L. P. Kouwenhoven  
Subject: Spin and charge in semiconductor nanowires.



# Publications

1. *Few-hole spin states in a silicon nanowire quantum dot*  
F. A. Zwanenburg, C. E. W. M. van Rijmenam, Y. Fang, C. M. Lieber &  
L. P. Kouwenhoven  
In preparation.
2. *Quantized energy emission in a few-hole Si nanowire quantum dot*  
F. A. Zwanenburg *et al.*  
In preparation.
3. *Magneto-field effect in InP nanowires with ferromagnetic contacts*  
F. A. Zwanenburg, D. W. van der Mast, H. B. Heersche, E. P. A. M. Bakkers &  
L. P. Kouwenhoven  
In preparation.
4. *Scanned probe imaging of quantum dots inside InAs nanowires*  
A. C. Bleszynski, F. A. Zwanenburg, R. M. Westervelt, A. L. Roest,  
E. P. A. M. Bakkers, & L. P. Kouwenhoven  
Nano Letters Vol. **7**, No. 9, p. 2559-2562 (2007).



---

---

Was leuk. Bedankt allemaal hè!

Floris



the end.

